Award Number:
W81XWH-11-2-0109

TITLE: Toward Development of a Field-Deployable Imaging Device for TBI

PRINCIPAL INVESTIGATOR: Pierre D. Mourad, PhD

CONTRACTING ORGANIZATION: University of Washington
Seattle WA 98107

REPORT DATE: June 2015

TYPE OF REPORT: Final report

PREPARED FOR: U.S. Army Medical Research and Materiel Command
Fort Detrick, Maryland 21702-5012

REPORT DOCUMENTATION PAGE		*Form Approved OMB No. 0704-0188*
Public reporting burden for this collection of information is estimated to average 1 hour per response, including the time for reviewing instructions, searching existing data sources, gathering and maintaining the data needed, and completing and reviewing this collection of information. Send comments regarding this burden estimate or any other aspect of this collection of information, including suggestions for reducing this burden to Department of Defense, Washington Headquarters Services, Directorate for Information Operations and Reports (0704-0188), 1215 Jefferson Davis Highway, Suite 1204, Arlington, VA 22202-4302. Respondents should be aware that notwithstanding any other provision of law, no person shall be subject to any penalty for failing to comply with a collection of information if it does not display a currently valid OMB control number. **PLEASE DO NOT RETURN YOUR FORM TO THE ABOVE ADDRESS.**		
1. REPORT DATE June 2015	**2. REPORT TYPE** FINAL	**3. DATES COVERED** 15FEB 2011 - 14MAR2015
4. TITLE AND SUBTITLE Toward Development of a Field-Deployable Imaging Device for TBI		**5a. CONTRACT NUMBER** **5b. GRANT NUMBER** W81XWH-11-2-0109 **5c. PROGRAM ELEMENT NUMBER**
6. AUTHOR(S) Pierre D. Mourad, PhD E-Mail: pierre@apl.washington.edu		**5d. PROJECT NUMBER** **5e. TASK NUMBER** **5f. WORK UNIT NUMBER**
7. PERFORMING ORGANIZATION NAME(S) AND ADDRESS(ES) AND ADDRESS(ES) University of Washington Seattle, WA 98195-9472		**8. PERFORMING ORGANIZATION REPORT**
9. SPONSORING / MONITORING AGENCY NAME(S) AND ADDRESS(ES) U.S. Army Medical Research and Materiel Command Fort Detrick, Maryland 21702-5012		**10. SPONSOR/MONITOR'S ACRONYM(S)** **11. SPONSOR/MONITOR'S NUMBER(S)**
12. DISTRIBUTION / AVAILABILITY STATEMENT Approved for Public Release; Distribution Unlimited		
13. SUPPLEMENTARY NOTES		
14. ABSTRACT Improvised explosive devices (IEDs) produce head injuries in nearly a majority of surviving soldiers. Most brain-injured soldiers do not, however, receive the necessary, rapid brain imaging studies as would their civilian counterparts. Instead they are flown to rear-echelon medical service centers such as in Germany for those studies, as well as additional medical care. There exists, therefore, a critical need for robust brain imaging systems at and near the battlefield. This gap in patient care reduces the quality of care and potentially, therefore the quality of life of injured soldiers. This gap also defines a critical need for rugged, field deployable systems capable of imaging injured brain. For a variety of reasons it is reasonable to expect that changes in the stiffness of brain accompany TBI, and that ultrasound-based 'sonoelastic' imaging modalities responsive to some measure of stiffness might offer a useful means for imaging the changes to brain due to TBI. Use of such systems in and near the field should improve clinical outcome for patients suffering from TBI. Our long-term goal is to develop a field deployable brain imaging system, capable of transcranial application, responsive to brain stiffness.		

15. SUBJECT TERMS traumatic brain injury, ultrasound, sonoelasticity, brain imaging.					
16. SECURITY CLASSIFICATION OF:			17. LIMITATION	18. NUMBER	19a. NAME OF RESPONSIBLE PERSON USAMRMC
a. REPORT U	b. ABSTRACT U	c. THIS PAGE U	UU	76	19b. TELEPHONE NUMBER *(include area code)*

Table of Contents

Page

INTRODUCTION – subject. Improvised explosive devices (IEDs) produce head injuries in nearly a majority of surviving soldiers. Most brain-injured soldiers do not, however, receive rapid brain imaging studies as would their civilian counterparts. Instead they are flown to rear-echelon medical service centers such as in Germany for those studies, as well as additional medical care. This is because magnetic resonance imaging is unavailable in or near the theatre of war (and a bad idea for many patients because of the presence of metal fragments) and because of the lack reliably operational CT machines at medical centers in Iraq. In the mean time, due to the lack of adequate neuro-imaging, acute neurosurgical care in response to closed TBI often requires a complete hemicraniectomy (removal of one side of the patient's skull) simply to assay the extent and location of injured brain. There exists, therefore, a critical need for robust brain imaging systems at and near the battlefield. Also, more subtle brain injuries are apparent clinically but difficult to definitively diagnose, hence treat. These gaps in patient care reduce the quality of care and potentially, therefore the quality of life of injured soldiers. This gap also defines a critical need for rugged, field deployable systems capable of imaging injured brain.

INTRODUCTION - purpose. For a variety of reasons (summarized in a recent book chapter of mine – Mourad, 2013) it is reasonable to expect that changes in the stiffness of brain accompany TBI, and that ultrasound-based 'sonoelastic' imaging modalities responsive to some measure of stiffness might offer a useful means for imaging the gross and subtle changes to brain due to TBI. Use of such systems in and near the field should improve clinical outcome for patients suffering from TBI. Our long-term goal is to develop a field deployable brain imaging system responsive to brain stiffness. Our system would do so through the use of ultrasound applied transcranially.

INTRODUCTION – scope of the research. To met the goal of this proposal we sought to test the following hypothesis: Rodent brain after closed TBI (blast, controlled cortical impact (CCI); ischemic stroke) manifest spatial patterns of endogenous and exogenous tissue displacement, hence patterns of brain-tissue stiffness, sufficient to map and identify the extent of each of hemorrhage, edema, and TAI, as tested via the following iterative aims.

Specific Aim #1: Quantify via histology and MR the spatial position and extent of each of hemorrhage, edema and TAI within each of the blast and CCI models of brain injury.

Specific Aim # 2: Directly measure the intrinsic stiffness of brain tissue of different types: normal gray and white matter; hemorrhagic brain; edematous brain; traumatized axons.

Specific Aim # 3: Use displacement-based ultrasound to image intrinsic brain tissue stiffness of normal versus traumatized rodent brains and their component parts.

Specific Aim #1: Quantify via histology and MRI the spatial position and extent of each of hemorrhage, edema and diffuse axonal injury (DAI) within each of the blast and CCI models of brain injury, with comparable studies for ischemic stroke.

Task (1): Generate closed TBI (mild and moderate-to- severe) in rats using blast methodology.

1) see Figure 1.

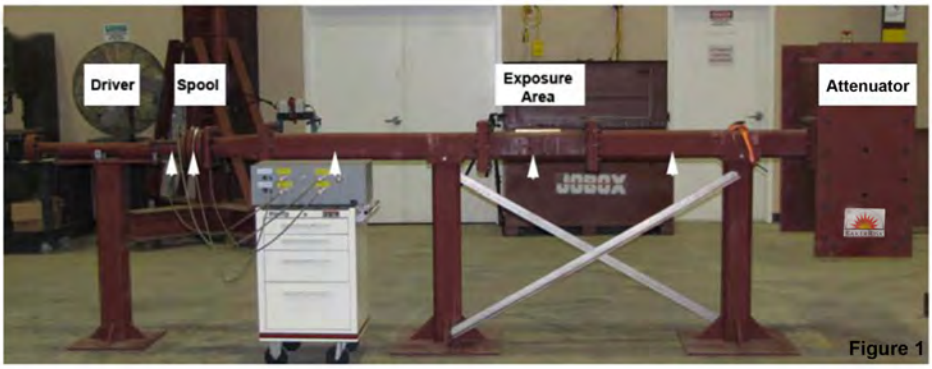

Figure 1. We used the **blast tube** shown here, deployed at the Veterans Association, to facilitate exposure of mice to blast waves. At the University of Virginia they used a comparable blast tube for their studies with rats.

Task (2): Generate closed TBI (mild, moderate-to-severe) using CCI methodology in mice, in 'mito' mice and in rats and ischemic stroke using an occlusion model in mice.

2) see Figure 2.

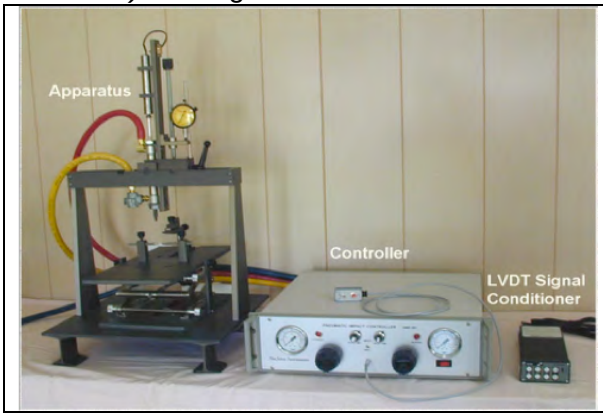

Figure 2. The device shown here creates a **controlled cortical impact (CCI)** in the cortex of mice and rats at the University of Washington. We used a comparable device at the University of Virginia for rats. The working element is the 'apparatus' where the rodents are placed in order to receive the impactor tip on their exposed brain. Red and yellow hoses facilitate movement of compressed gases that actuate the device as controlled by the ancillary devices. We induced ischemic stroke in other mice via ligation of the middle cerebral artery.

Task (3): MR image rodent brains.

3.a) UVa has performed all of its of MRI studies of CCI rats (Figure 3a,b). They have finished co-registration of those MR images with standard rat-anatomy images, in order to develop direct correlation of the brain-injury features in each imaging modality (Figure 3c). The damage corresponds with changes in histology and in ultrasound imaging or detection, discussed below.

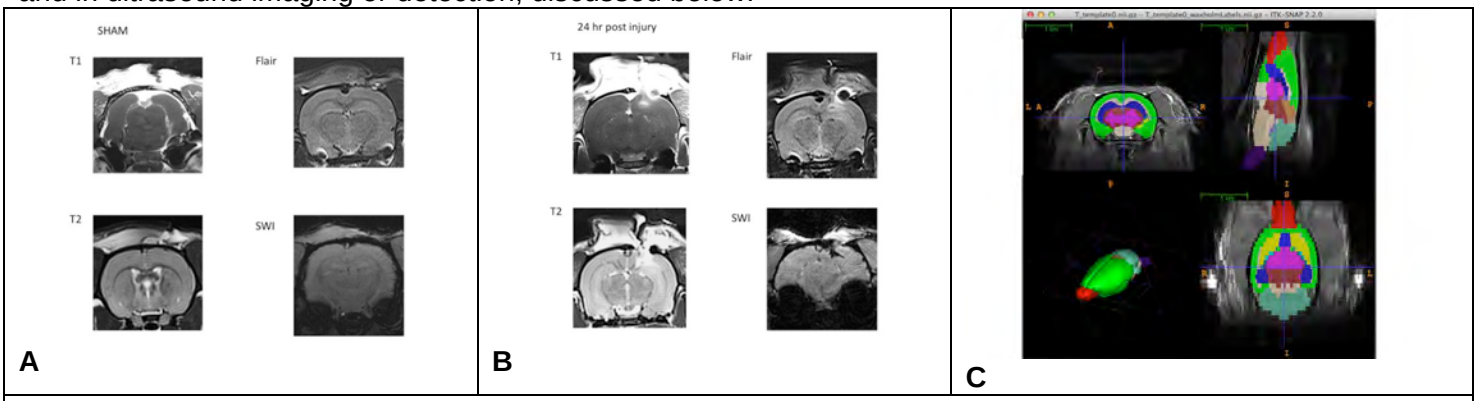

Figure 3. Images of rat brain after actual and sham controlled cortical impact (CCI) injury. (A) shows various MRI images of coronal views of sham injured rat brains. **(B)** shows various comparable MRI images of injured rat brains. The injury manifests in the upper right-hand quadrant of the brain, encompasses the cortex down to the hippocampus. 'T1' highlights the basic structural abnormality generated by the CCI, 'T2' highlights fluid buildup at the site of CCI, 'Flair' refers to fluid attenuated inversion recovery that suppresses fluid-specific signals to highlight changes in tissue structure, 'SWI' refers to susceptibility weighted imaging that is sensitive to venous blood and hemorrhage. **(C)** shows co-registration of MRI images with a rat-brain atlas, each of the major components of brain highlighted in different colors. Follow-on co-registration of the atlas with histological images will complete a useful triad of MRI/Atlas/histology, with completion of the analysis anticipated after the close of this grant.

3.b) UVa has performed all of its of MRI studies of mild and moderate/severe blast rats (Figure 4). Interestingly, they see no changes in neuroanatomy either acutely or 24 hours after blast. As discussed below, this is largely consistent with histology, consistent with brain-tissue stiffness measurements of mild blast rats that together suggest that there exist vascular changes in brain after a single mild blast but not major histopathological changes, as we discuss below.

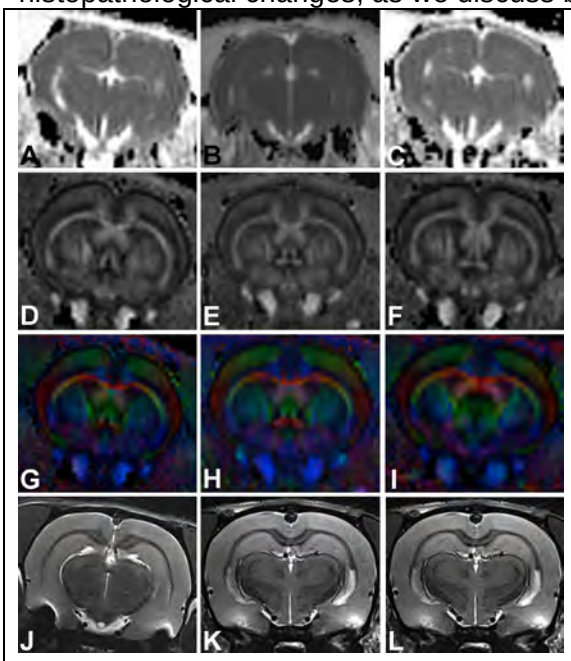

Figure 4: Coronal MRI plates acquired from rats undergoing experimental severe blast overpressure exposure at UVA. Diffusion weighted imaging (DWI) MRI are shown in plates A-C. Fractional anisotropy (FA) maps calculated from diffusion tensor imaging (DTI) are shown in plates D-F. FA DTI maps with directional color coded values are displayed in plates G-I, while fluid attenuation inversion recovery (FLAIR) images are seen in plates J-L. Plates A, D, G, and J were acquired from SHAM prepared animals. Plates B, E, H, and K were acquired from blast injured animals at 2 hours following exposure, wile plates C, F, I, and L demonstrate imaging from blast injured animals at 24 hours following exposure. No appreciable differences were seen between 2 h or 24 h post-blast animals as compared with SHAM controls across any of the studied MRI sequences, either mild or moderate/severe blast.

3.c) Colleagues at the Veterans Administration of Puget Sound (VA) have performed all of its of MRI studies of mild blast mice (Figure 5), imaged 24 hours after blast exposure. Interestingly, they see changes in the size of the cerebral ventricles, acutely, without, however, observing other structural changes. As discussed below, this and the UVa blast results are largely consistent with histology and with brain-tissue stiffness measurements of blast rats. Taken together, these data are consistent with the hypothesis that blast induces at least vascular changes in brain but not major histopathological changes, as we discuss below.

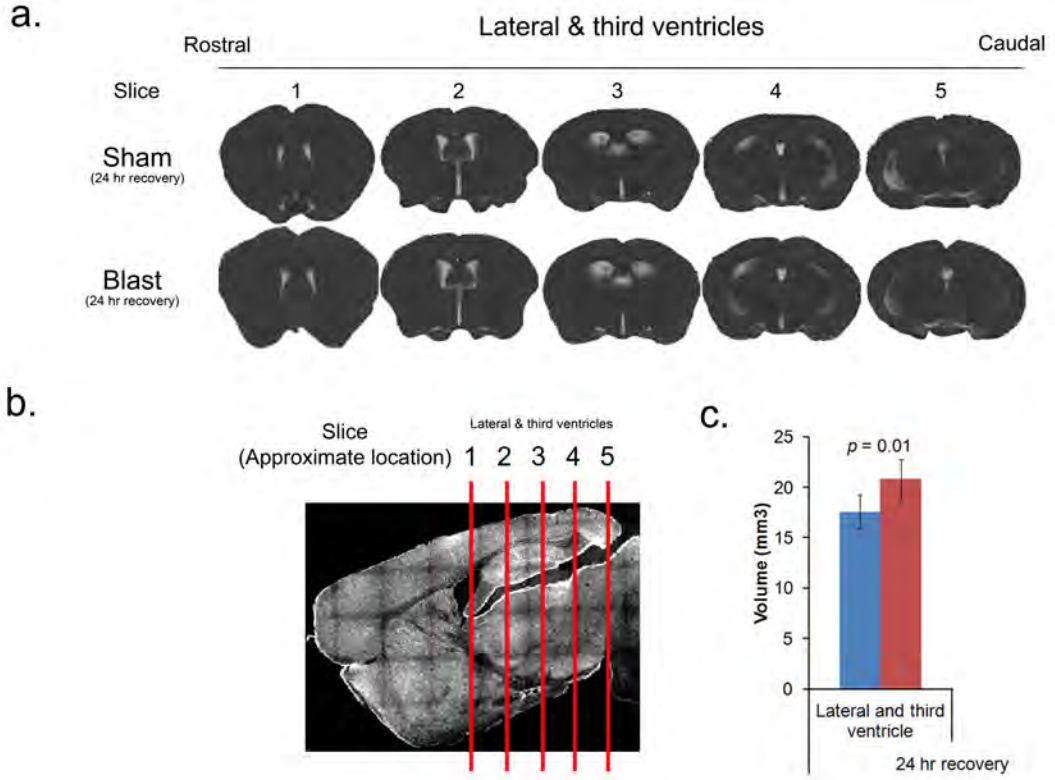

Figure 5. MRI images of mouse brain collected 24 hours after acute or sham mild blast. (A) This figure shows T2 weighted images of coronal slices of mouse brain, from rostral to caudal, after sham or actual blast exposure. **(B)** This figure shows a sagittal view of mouse brain and the position of the coronal slices from 'A'. **(C)** These results show that averaged across all slices, that the area of the lateral and third ventricles ventricles are larger 24 hours after actual (red) versus sham (blue) blast.

Task (4): Immunohistochemical assays.

4a) We at UW have collected wide field fluorescent microscopy brain-tissue images from rats (Figure 6) and mice, showing focal injury within a few millimeters of the impact site. These results are representative of the effects created through the same injury mechanism induced in mice at UW and rats at UVa.

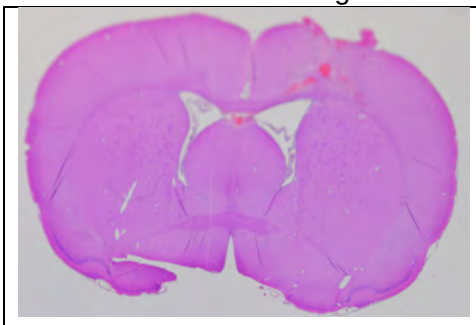

A

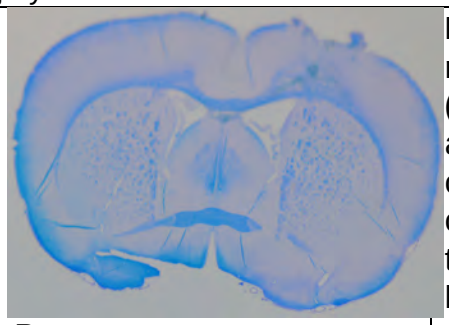

B

Figure 6. Coronal slice of mouse brain after CCI. **(A)** Hematoxylin and Eosin and **(B)** cresyl violet staining of rat brain subjected to a controlled cortical impact in the animal's right hemisphere (left from our viewpoint).

4b) We here at UW have also subjected 'mito-mice' subjected to CCI (Figure 7a,b). (These mito-mice have the unique property that the mitochondria within the neurons in their brain fluoresce when healthy.) We have identified unanticipated *increases* in fluorescence at the site of injury pointing to possible decreases in the ability of the neurons and axons to transport mitochondria, or, to changes in mitochondria morphology and function. Moreover, we observed changes in both ipsilateral as well as contralateral fluorescence due to injury, with comparable levels of fluorescence both acutely as well as 24 hours after injury (Figure 7c). Interestingly, we did not see this kind of damage for mild TBI (data not shown).

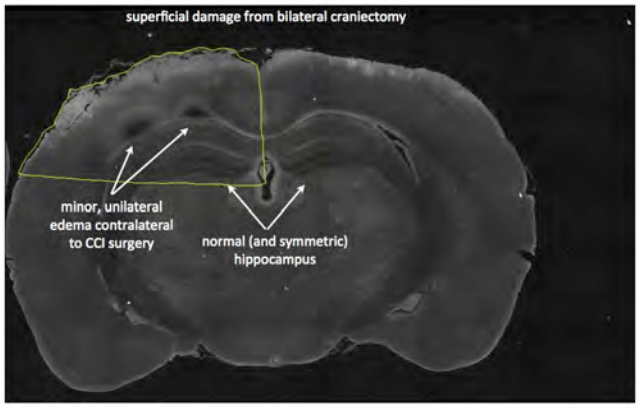

A

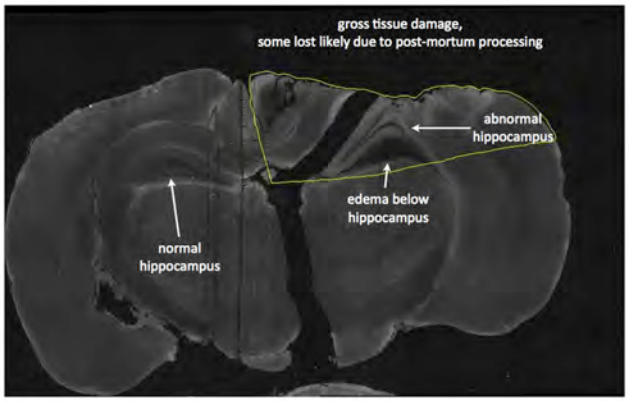

B

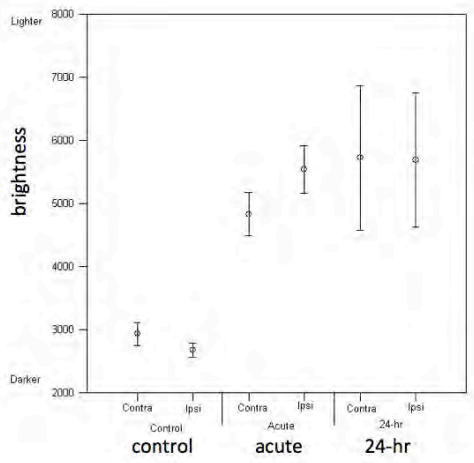

Figure 7. mitoMice brains – lighter gray has greater concentration of mitochondria than darker gray. (A) This figure shows a coronal slice of brain subjected to the initial surgery to create TBI via CCI then the subsequent surgery to widen the craniectomy ipsilateral to the sham surgery site and contralateral to the sham surgery site**. (B)** This figure shows a coronal slice of brain subjected to actual CCI. Note the enhanced fluorescence within the hippocampus (as well as edema and large-scale necrosis), suggestive of mitochondrial dysfunction and/or reduced transport. **(C)** Averaging over all data (N = 3) we observe increase in fluorescence in both hemispheres due to a single-hemisphere contusion injury that affects axonal transport in the upper quadrants of both hemispheres.

4c) With our VA colleagues we have measured subtle histological changes induced by blast TBI associated with the structure of mouse brain after blast (Figure 8; also Huber et al 2014, *J Alzheimers Disease.* 37(2):309-23. PMID:23948882).

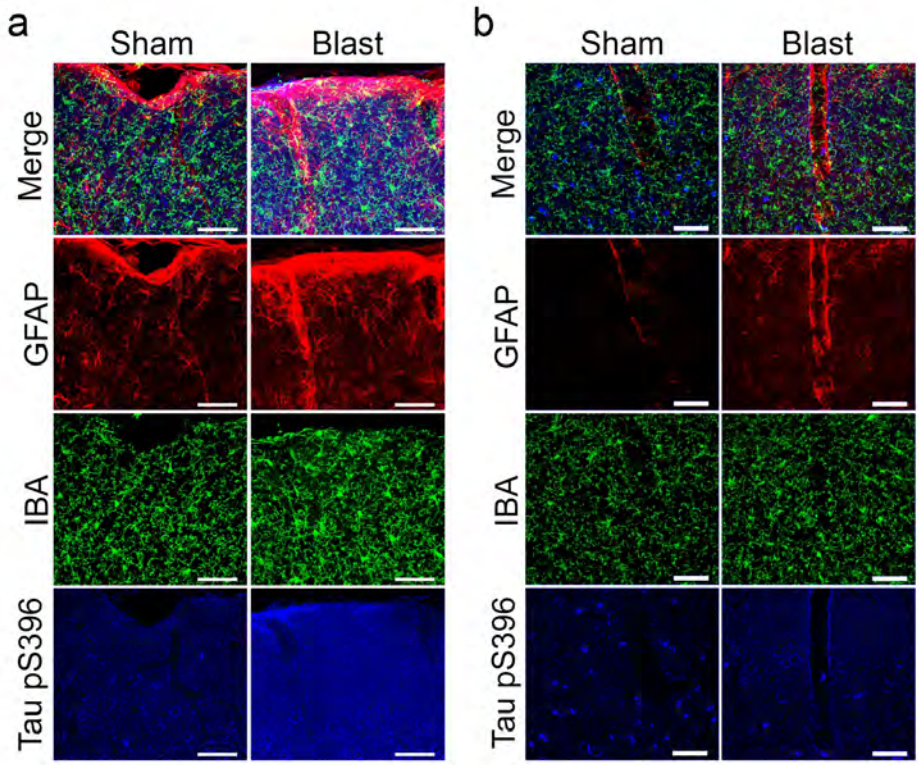

Figure 8. A single mild blast in mice at the Seattle VA causes cortical glial reactivity above the lateral ventricle within 24 hours after exposure. a) Reactive astrogliosis, marked by increased GFAP immunoreactivity (red), and microglial activation (increased Iba immunoreactivity and altered morphology; green), is seen at the cortical surface. Glial changes induced by blast are prominent in the glial limitans and along the penetrating vessels of the cortex. Tau phosphorylated at serine 396 (blue) is induced by blast mTBI as previously reported (Huber et al., 2013). b) Glial reactivity to blast exposure is also evident in deeper cortical tissue. This image is ~500 µm from the dorsal roof of the lateral ventricle.

4d) With our UVa colleagues we have measured subtle histological changes in axonal structure induced by blast TBI (Figure 9).

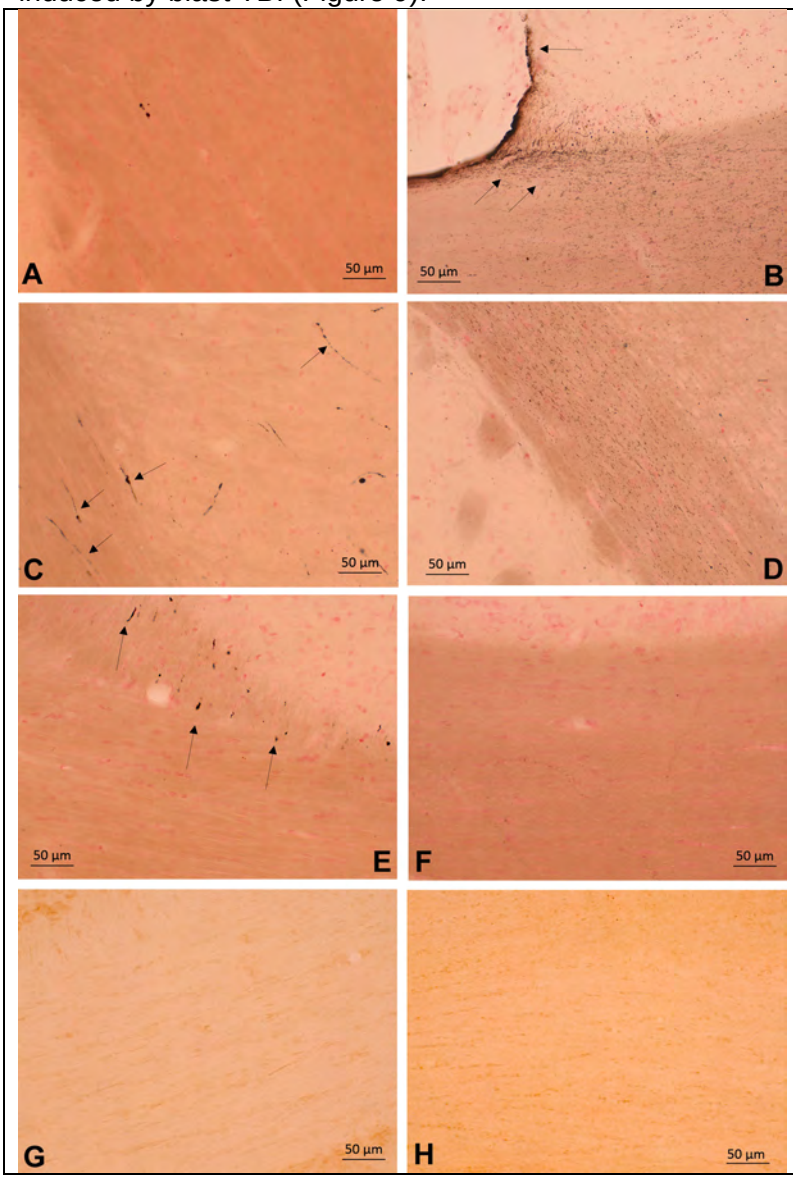

Figure 9. Multiple photomicrographs from rodents experiencing blast overpressure exposure demonstrate subtle axonal changes. Modified silver degeneration stain in SHAM animals allowed to survive 24 hours following preparation (A,F), 2 hours following blast exposure (B), and 24 hours following blast exposure (C-E). Plates A-D are acquired from frontal cortical/subcortical regions while Plates E and F are from cortical and white matter regions within the region of the body of the corpus callosum. Plate G is acquired from frontal subcortical white matter in slides stained with RM014 neurofilament antibody while plate H is stained with amyloid precursor protein (APP). Plates G and H are both derived from animals allowed to survive for 24 hours following blast exposure. These images demonstrate a dark stain associated with axonal degeneration in animals allowed to survive 2 hours and 24 hours following blast overpressure exposure. Similar findings are not present within SHAM animals. Additionally, axonal degeneration is not observed in RM014 or APP stains suggesting a form of axonal degeneration that does not involve either neurofilament dephosphorylation or appreciable accumulation of APP at the studied time points.

Specific Aim # 2: Directly measure the intrinsic stiffness of brain tissue of different types: normal gray and white matter; hemorrhagic brain; edematous brain; ischemic brain; traumatized axons.

Task (5): Calibrate indenter system and apply it in vitro as well as to rodent brain tissue samples dominated by one of each of normal gray and white matter; hemorrhagic brain; edematous brain; traumatized axons.

5a) This system is calibrated and working after quite extensive development of the technique. We have shown statistically significant changes in brain tissue viscoelastic structure at the site of CCI – Figure 10. We have published work – (Gabler et al, 2013 - attached).

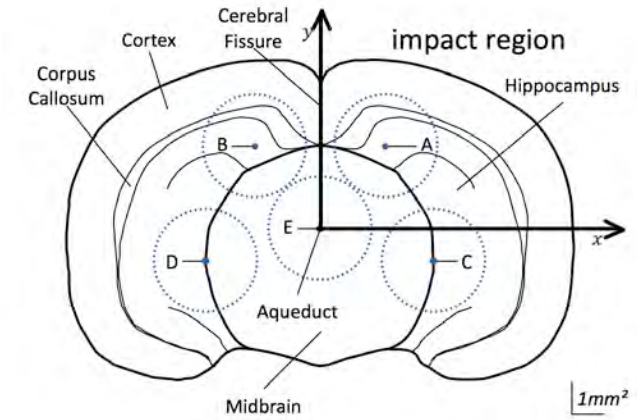

A

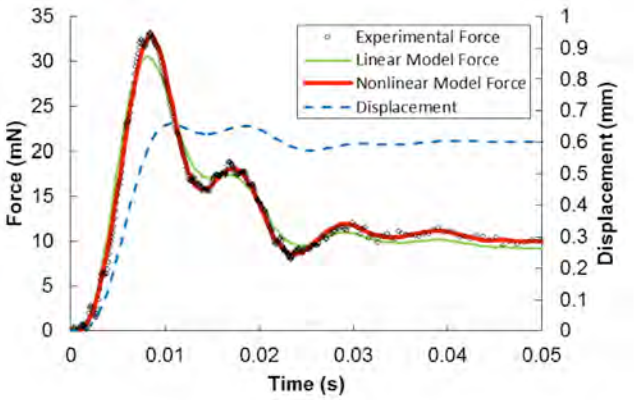

B

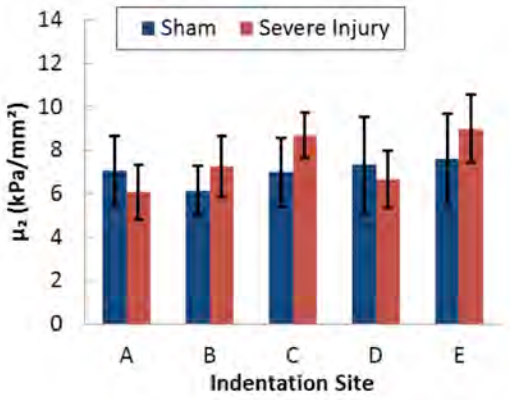

C

Figure 10 shows our indenter results for CCI rats. Figure **(A)** shows a schematic of indenter position measurements while Figure **(B)** shows measurements of rat-brain displacement (horizontal axis) versus measured elastic response in milliNewtons, all as a function of time, along with associated mathematical modeling. Figure **(C)** shows the results that demonstrate increase in the viscoelasticity, hence stiffness of brain after CCI at the various spots within the brain from which data was collected.

5a) We applied this same indentation methodology to rats after sham or blast injury, both acutely (within 2 hours of blast) and 24 hours after blast injury – Figure 11. Throughout the majority of brain we did not observe a change in brain-tissue stiffness, either acutely or after 24 hours, for either low or high blast. We did observe sub-regions of brain with changes in brain-tissue stiffness. Specifically, we observed for high blast rats significantly higher peak forces (+57.7%) in the midbrain inferior region, showing an increase in brain tissue stiffness for these animals at that location. In contrast, we observed for low blast rats lower peak forces (-39%) in the brain stem, demonstrating a decrease in brain tissue stiffness for these animals at that location. We have offered these results in a poster presentation (Alshareef et al, 2015 – attached).

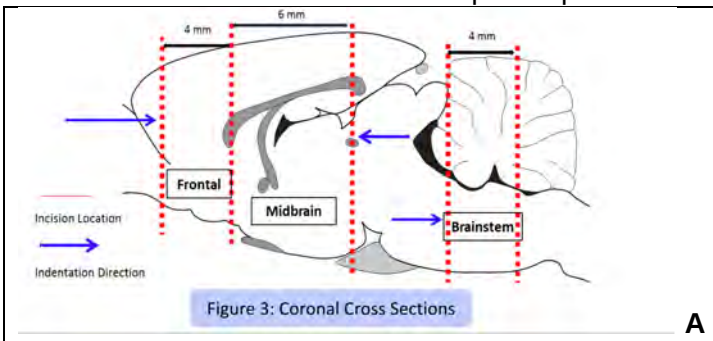

A

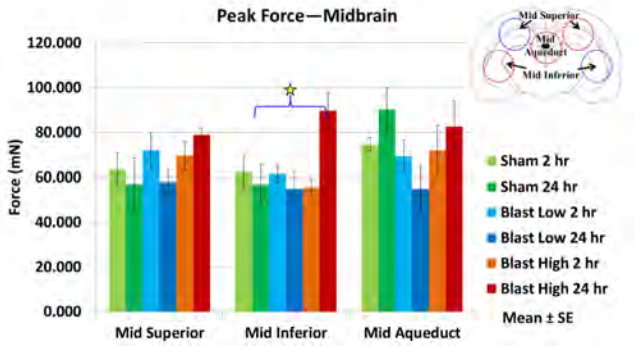

B

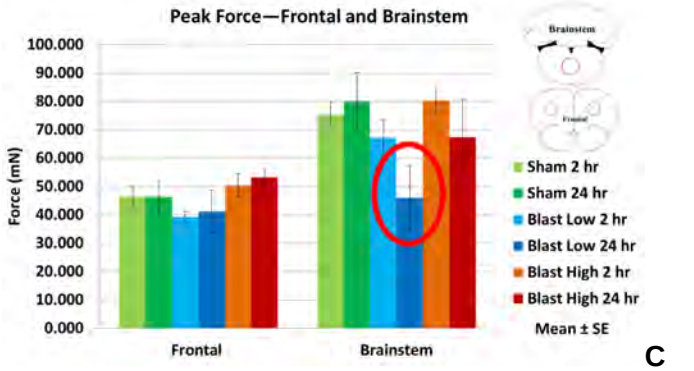

C

Figure 11. (A) This figure shows the three different sections of brain whose stiffness we measured at the University of Virginia. In almost all areas of mid-brain we did not observe a difference in brain-tissue stiffness, either acutely or after 24 hours, either for low or high blast. Exceptions include **(B)** an increase in brain stiffness within the ventral aspect of the mid-brain for high-blast brain 24 hours after exposure and **(C)** a decrease in brain stiffness within the brainstem for low-blast brain 24 hours after exposure.

Specific Aim # 3: Use displacement-based ultrasound to image intrinsic brain tissue stiffness of normal versus traumatized rodent brains and their component parts.

Task (6): Optimize commercial ultrasound-imaging device based on measurement of exogenous brain palpation.

6a) We have established a procedure (Figure 12) for optimizing the analysis of images from the commercial ultrasound imaging system, based on exogenous brain palpation by the SuperSonic Imagine (SSI) machine via the acoustic radiation force and subsequent monitoring of the propagation of the shear wave.

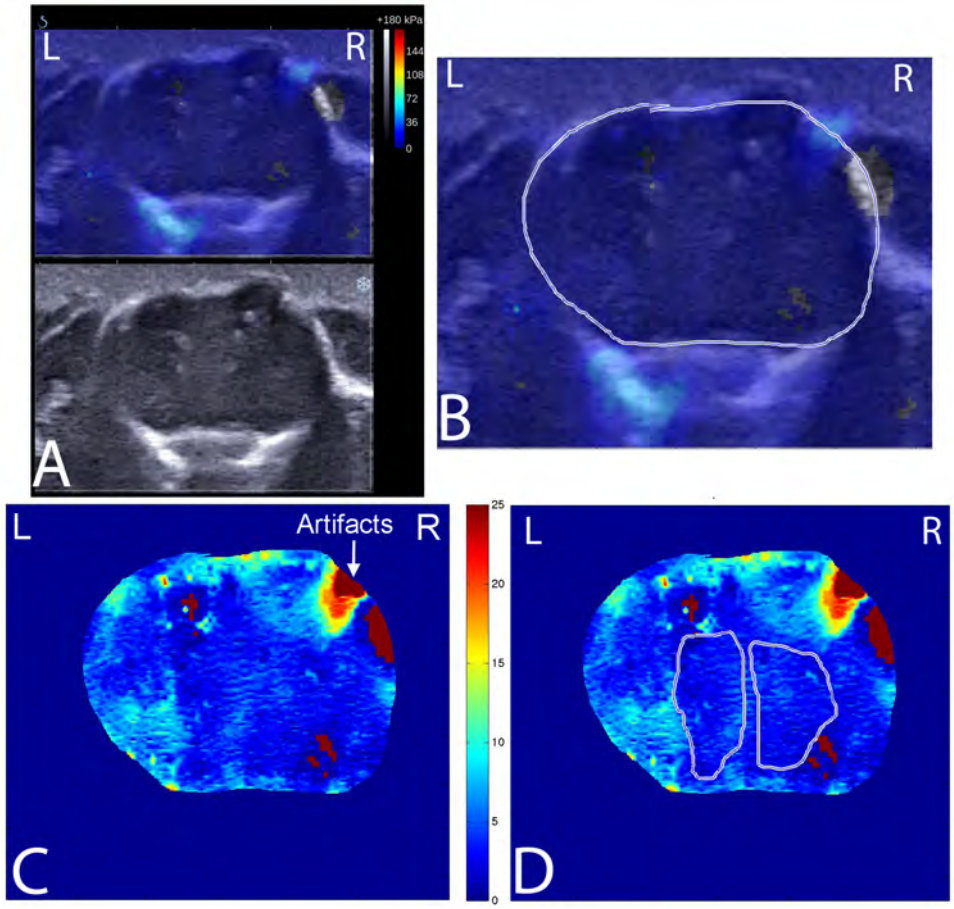

Figure 12. Image Processing associated with the SuperSonic Imagine commercial ultrasound imaging system. (A) Aixplorer images in SWE mode (top) and B-mode (bottom) (B) The brain region was selected from the elastographic image (0-180 kPa) with reference to the B-mode image. (C) The SWE image of the brain was rescaled to 0-35 kPa to enhance the contrast. (D) Regions of Interest selected manually to avoid skull and artifacts (large values of Young's Modulus greater than that of brain).

Task (7): <u>Optimize</u> research ultrasound-imaging device based on measurement of exogenous and endogenous brain palpation.

7a) With regard to exogenous brain palpation, we can track shear-wave propagation using our research ultrasound-imaging device (the VUE system) – Fig. 13. We discuss the details of this methodology in the attached senior thesis (Yayun, 2013).

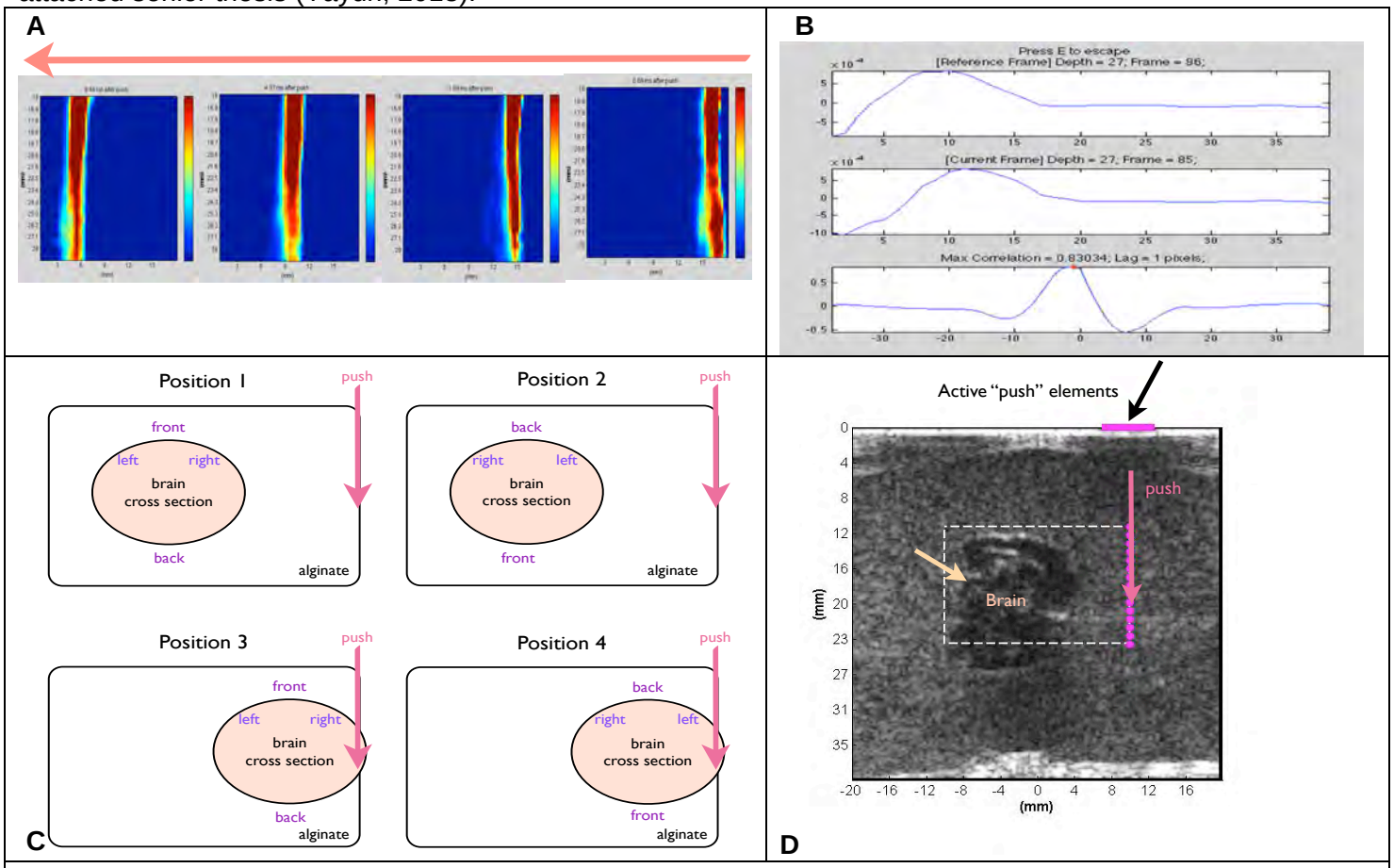

Figure 13. Quantification of shear wave propagation in alginate. We can create a focal and vertically elongated, vertical push within alginate (and tissue – below) that **(A)** generates a horizontally propagating shear wave, whose speed we can quantify and translate **(B)** through custom software that cross-correlates temporally adjacent ultrasound images along a given horizontal line. The local stiffness of tissue is proportional to the square of that local speed of the shear-wave propagation. **(C, D)** We studied shear-wave propagation into damaged brain *ex vivo* from a variety of angles relative to the injury in brain in an attempt to develop an image of the contusion injury created by the CCI mechanism.

7b) We have developed and validated an exogenous brain palpation system based on vibrating brain with focused ultrasound, whose methodology we review in Figure 14a and demonstrate capable of measuring acoustic emissions from brain (Figure 14b). We report results below.

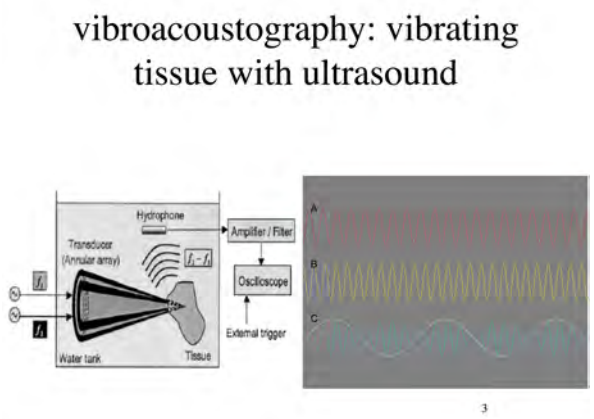

A

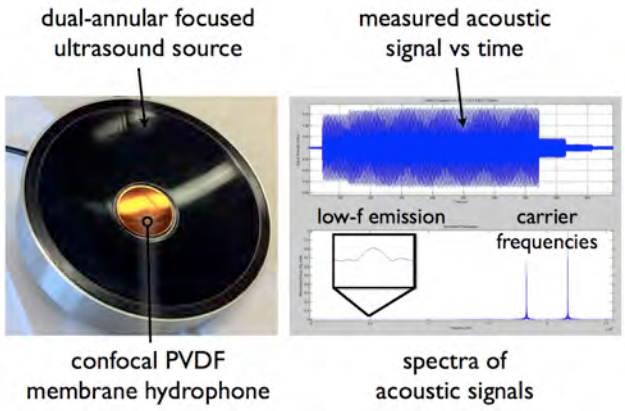

B

Figure 14. Vibro-acoustography as a means of assaying for the presence of traumatic brain injury. (A) In vibro-acoustography, a dual-transducer device ('transducer (annular array)") emits two, separate pulses of ultrasound at two different, but close frequencies – pulse train 'A' and 'B'. At their mutual focus, high frequency oscillations move the tissue slightly; their beat frequency generates a low-frequency emission, itself sampled from a separate hydrophone placed either in the water tank or within the iFU source itself for *in vivo* applications. **(B)** This figure shows our device and real data rather than the conceptualization of Figure 6A, highlighting a measured waveform that demonstrates the signal generated by the two, spatially overlapping high frequency iFU signals, and small amplitude, low-frequency acoustic emissions.

7c) To create endogenous ultrasound imaging results we have demonstrated that we can measure the pulsation of mouse brains completely enclosed within their crania, pulsations created by both their breathing and their heart beat. We deployed our tissue pulsatility imaging (TPI) system at each of the University of Virginia and at the Veterans Association of Puget Sound. Here we describe the data collection and analysis procedures.

Tissue Pulsatility Imaging System

An L12-5 ATL scan head connected to a Verasonics ultrasound acquisition system was used to capture pulsatility data from the brain. Ultrasonic emissions from the scan head, pulse repetition frequency (PRF) of 64 Hz and sampling frequency 30MHz, were then used to produce coronal brain images at locations relative to the interaural line. Data acquired by the scan head was linked to the Verasonics ultrasound platform, which facilitated data conversion and real time visualization in MATLAB. Once in MATLAB, data was processed via custom scripts that were developed to extract the tissue pulsatility signal.

Application of Ultrasound

The L12-5 ATL TPI scan head was coupled to the head of the rodent (mice at the VA and rats at UVa) and aimed at the cerebral ventricles within the middle of the rodent brain via sterile ultrasound gel (Figure 15a). Data collected from the TPI scan head was transferred to the Verasonics acquisition system for MATLAB based processing. The scan head was mounted on a three-way micro-positioning system (Velmex, INC., East Bloomfield, NY, USA) to allow the imaging plane (in the case of TPI) to be moved to any anatomical region of interest. In similar fashion the micro-positioner was used to move the B-mode imaging plane of the TPI transducer to each of the target locations slice A, B, C, and D (Figure 15b). These target locations were defined relative to the interaural line such that the TPI imaging plane would fall on the lateral ventricles. Therefore, slice A was 4mm anterior to the interaural line, slice B 3.6mm, slice C 3.2 mm, and slice D 2.8 mm. B-mode images captured via TPI were exported to MATLAB for analysis. In MATLAB a region of interest (ROI) around the ventricles was selected (Figure 15c), custom scripts were utilized in order to extract the tissue displacement waveform from each pixel within the ROI. This process was conducted for each of the five TPI imaging locations.

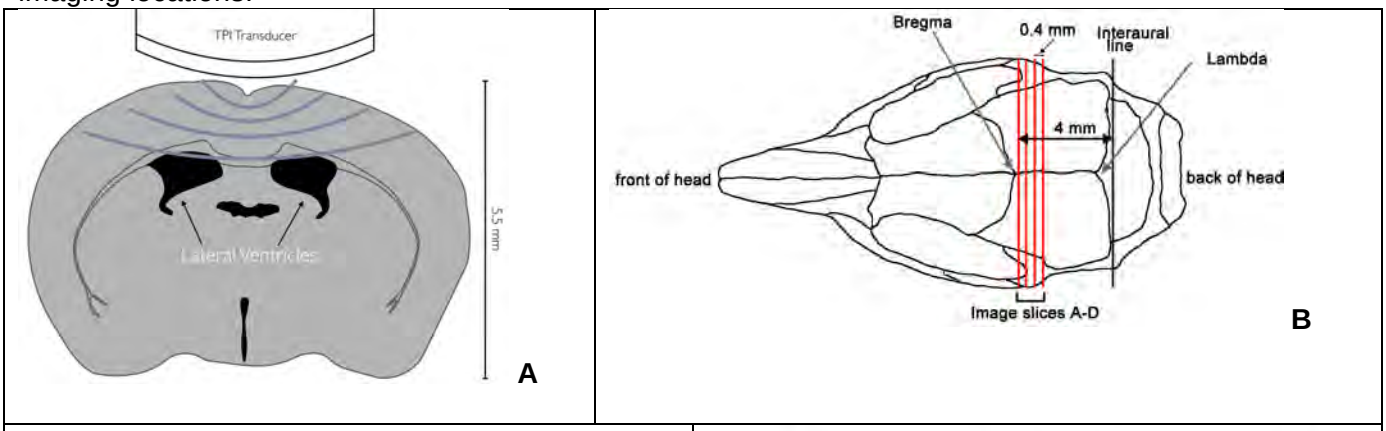

Figure 15: collection of tissue pulsatility imaging data from blast mouse and rats. In **(A)** we offer a schematic that shows the relationship between the ultrasound scan head ('TPI transducer) and a coronal slice of brain at the point of largest ventricle volume, where we targeted our imaging studies. In **(B)** we offer a schematic that shows a planar view of rodent head and the position of the ultrasound image slices (A-D). In **(C)** we offer an ultrasound image of mouse brain (dark oval) within which we have defined a region of interest centered on the ventricles.

Analysis of Tissue Pulsatility Data

Initial review of extracted tissue pulsatility waveforms indicated the presence of large-scale trends of unknown origin, to eliminate these distortions all waveforms were de-trended such that the mean value of the displacements become zero (Figure 16a). Following de-trending a fast Fourier transform (FFT) was performed on the data (Figure 16b). The FFT contain peak values of displacement that correspond to the respiratory and tissue components of the pulsatility signal: The respiratory component has a frequency of approximately 1 Hz and the tissue component has a frequency of approximately 4 Hz.

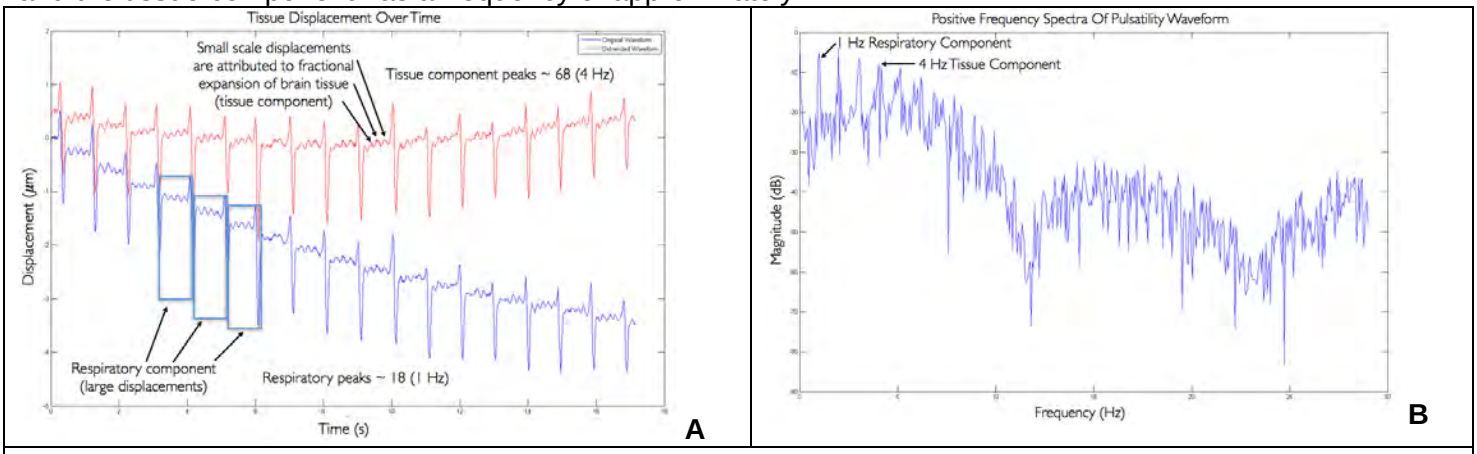

Figure 16: tissue pulsation at various scales of rodent brain. (A) From each pixel within the ROI a displacement waveform (shown above) is extracted. Note the original waveform (blue) includes a net trend that influences both the respiratory and tissue components). We remove this trend to set the mean value of the signal to zero (red). Remaining are brain-tissue displacements on time scales of the heart beat (4 Hz 'tissue component') and respiration (1 Hz). **(B)** The fast Fourier transform of the de-trended pulsatility waveform shows peaks in frequency that corresponds to the respiratory and tissue components of the pulsatility signal as well as their harmonics.

Next, we then apply a bandpass filter to the data, with cutoffs at 3 and 9 Hz in order to remove low/high frequency noise and to remove the respiratory component (Figure 17a). After filtering, the root mean square (RMS) of the pulsatility waveform as extracted (Figure 17b) for analysis, described below.

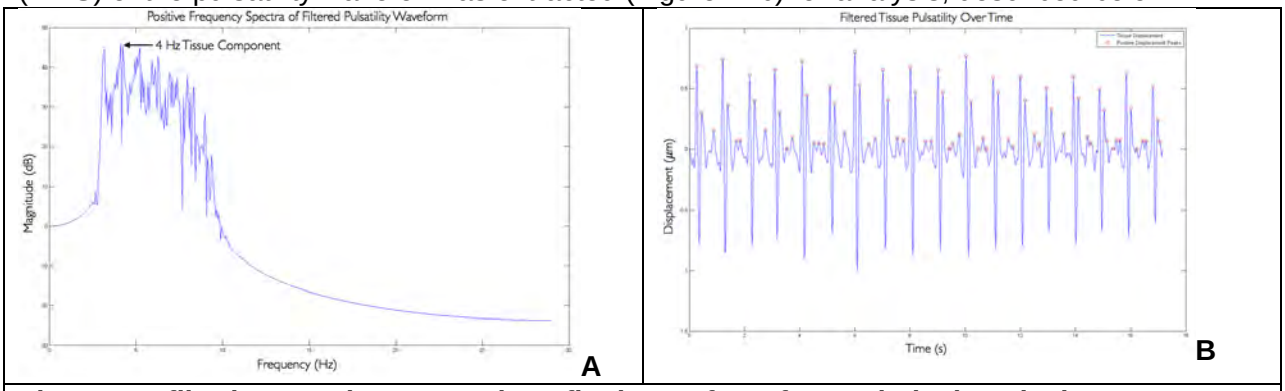

Figure 17: filtering TPI data to produce final waveform for statistical analysis.
(A) Implementing a bandpass filter with cut-offs at 3 and 9 Hz we are able to extract the tissue component and eliminate some low/high frequency noise as well as the unwanted respiratory component. **(B)** This figure shows the filtered time series of brain tissue pulsation from a single pixel. (As a visual aid the peak positive values are shown here as circles on this waveform).

These RMS of the TPI signal was extracted for every pixel within the ROI for a given animal and used to calculation a distribution of RMS TPI displacement for each imaging plane for reach animal. As we discuss below, by comparing these characterization distributions between blast and sham animals the Kolmogorov-Smirnov (KS) test, a single distribution of KS measures was developed to seek differences (as determined by KS metrics) between sham and blast brains. By comparing the true mean value of the KS distribution with the expected mean value derived by assuming that Blast and Sham TPI pixel distributions are the same, we were able to determine the statistical significance of brain-tissue displacement between blast and sham blast rodents.

Task (8): Image or detect normal versus damaged rodent brains with commercial and research ultrasound devices.

(8a) We used the technique developed in Task 6 to study the brains of CCI-induced TBI mice and rats – Figure 8 – and have published the results (Xu et al, 2014). Specifically, these results demonstrate changes in hemispherically averaged shear modulus for each of the hemispheres due to ipsilateral TBI (Figure 18). The ipsilateral decrease in shear modulus relative to control is consistent with the combination of focal ischemia and wide spread edema formation after CCI, a well-established phenomenon in this animal model for TBI. interestingly, we also see a contralateral increase in shear modulus relative to control by 24 hours after CCI injury, consistent with other's observation of reduction of blood flow contralateral to injury as well as elevated global ICP.

Figure 18 demonstrates our ability to <u>detect</u> changes in intra-hemispheric brain stiffness after TBI using our commercial imaging system. Average values of 'shear-modulus' values (normalized by the average value for the entire given brain) within a hemisphere of mouse or rat brain, averaged across five **(A)** mice and **(B)** rats demonstrate that the ipsilateral hemisphere has a lower mean, normalized shear modulus than the contralateral hemisphere by 24 hours after CCI injury. These values change also relative to sham TBI values, which themselves agree between hemispheres. We see comparable results for stroke (Xu et al, 2013).

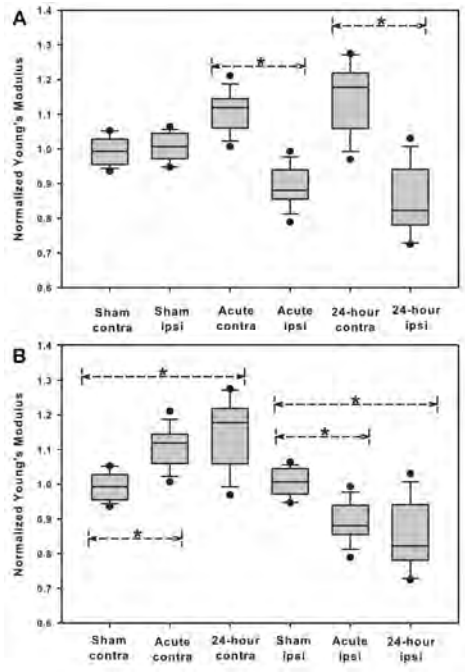

A

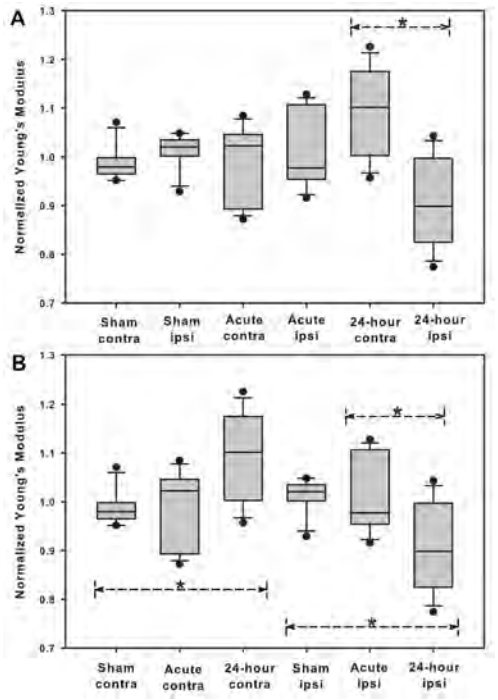

B

(8b) We used the technique developed in Task 7a on CCI-induced TBI mouse brain *ex vivo* – Figure 19, as described in the senior thesis (Yayun, 2013). These preliminary results suggest that we can image small brain contusions with shear-wave based methods, although translating this to transcranial results has thus far proved quite difficult, due to the skull's tendency to severely distort and attenuate the impulsive force generated by the ultrasound necessary to create the propagating shear wave.

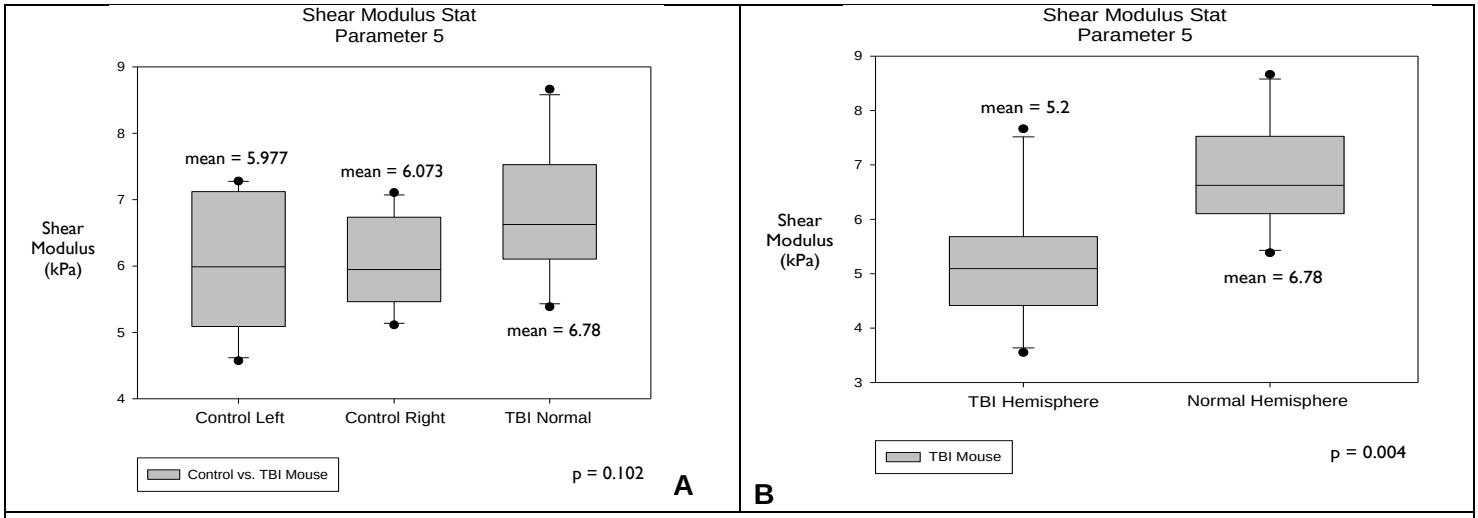

Figure 19 – results of analysis of ex vivo shear-wave propagation in mouse brain. Figure **(A)** shows that the measured shear modulus of each hemisphere of control brains are comparable to each other and slightly less stiff than the hemisphere of TBI brain contralateral to hemisphere, consistent with our published results using the commercial system. Figure **(B)** shows that the TBI hemisphere has reduced shear modulus compared to the contralateral (here, 'normal') hemisphere, again consistent with our published results using the commercial system.

(8c) We used the vibroacousticography technique of Task 7b to show statistically significant variations in acoustic emissions from within severe acute CCI TBI rat brain relative to sham TBI rat brain, with data collected several millimeters away from the TBI site (Figure 20a,b), published in Suarez et al. (2015). These results show that brain tissue is stiffer after CCI injury as compared to sham CCI injury. In contrast, we observed the no statistically significant differences between blast and sham-blast mice 24 hours after exposure in the regions centered on their ventricles, suggesting that by this measure the brains of blast mice do not change their stiffness in a way detectable via our use of vibroacoustography.

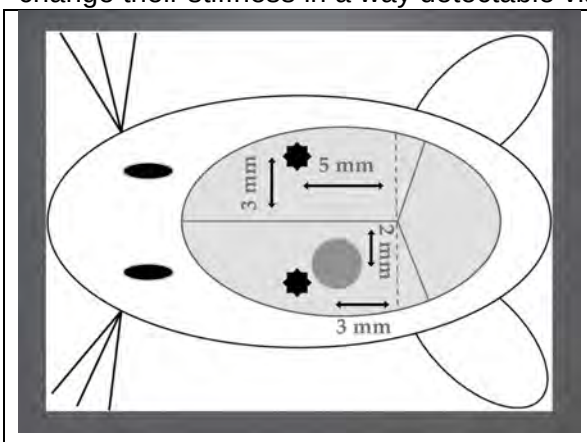

A

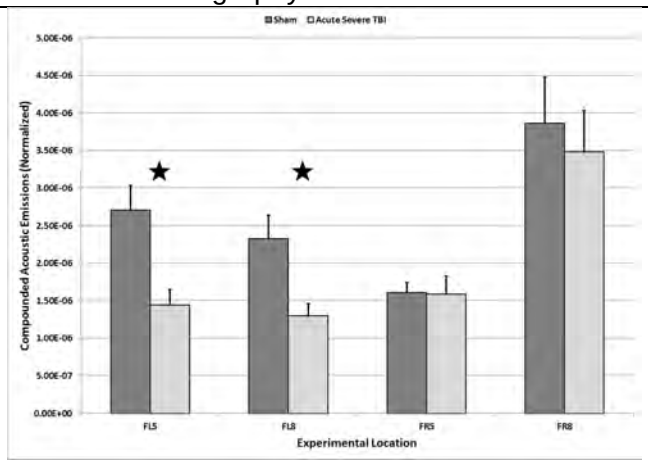

B

Figure 20 – experimental results for vibroacoustography for CCI TBI rats. Figure **(A)** shows a schematic of the experimental setup for acute CCI TBI. The large ellipse represents the portion of the skull from which skin and fascia were removed, exposing the suture lines. The circle represents the placement of the brain contusion after performing a small craniectomy. Black stars denote superficial projection of placement of the vibroacoustography focus at 5mm or 8mm deep within the cranium, one in the front left (FL) hemisphere and the other in the front right (FR) hemisphere. Figure **(B)** demonstrates that the acoustic emissions associated with acute sham (dark) are larger than that measured from acute severe CCI when compounded across the difference frequencies from 200-270 kHz.

8d) We used the TPI procedure of Task 7c to look for changes in brain tissue pulsation in CCI mice and blast mice (at the VA) and blast rats (at UVa). We observed trends in differences in TPI amplitude for sham versus actual CCI mice (a tendency towards smaller brain-tissue displacements, hence stiffer brain, for actual versus sham CCI animals) without, however achieving statistical significance (data not shown). We hypothesize that adding more mice to the protocol will allow these trends to become statistically significant.

In contrast, we found a statistically significant reduction between brain tissue pulsation in the region of the maximum volume of the ventricles for actual versus sham blast mice (moderate blast; 24 hours after exposure) at the VA and actual versus sham blast rats (mild blast, acutely) at UVa. Figure 21 shows sample distributions of RMS tissue pulsation in a single slice of sham versus mouse brain (left) and in a single slice of sham versus rat brain (right).

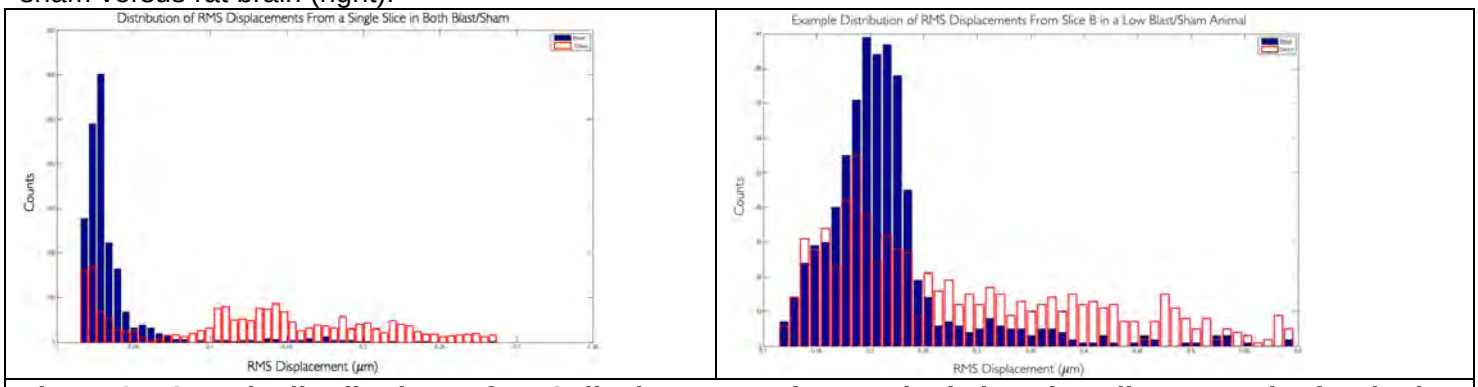

Figure 21. Sample distributions of RMS displacements from a single imaging slice on each of a single Blast (blue) and a single Sham rodent (red). A mouse sample is on the left and a rat sample is on the right. Average displacement of blasted rodent brain was smaller than that of corresponding sham animals.

We averaged the measured distributions of tissue pulsation for a given slice, separately, for each of blast and sham-blast animals. The Kolmogorov-Smirnov (KS) test quantifies the difference between measured tissue-displacement distributions from two separate collections of data (sham blast versus actual blast, for a chosen slice of TPI data) for a single slice (A, B, C, or D) in the following fashion. In Step 1 all samples of tissue pulsation distribution from a given sham slice A (for example) are compared via the KS test with all samples of tissue pulsation distribution from a given blast slice A, in a random fashion. This produces a new distribution of a new variable: of KS values themselves (blue histograms in Figures 22) that arise from this comparison. In Step 2 we determine if that distribution of KS values has significance, by comparing the actual KS distribution (again, blue histograms) with the KS value that arises after analyzing the two distributions that arise after randomly mixing the sham and blast tissue pulsation distributions together (red line). Blast mice and rats 24 hours after exposure each showed a statistically significant reduction in brain-tissue displacement in the region of the ventricles as compared to sham blast rodents (Figure 22).

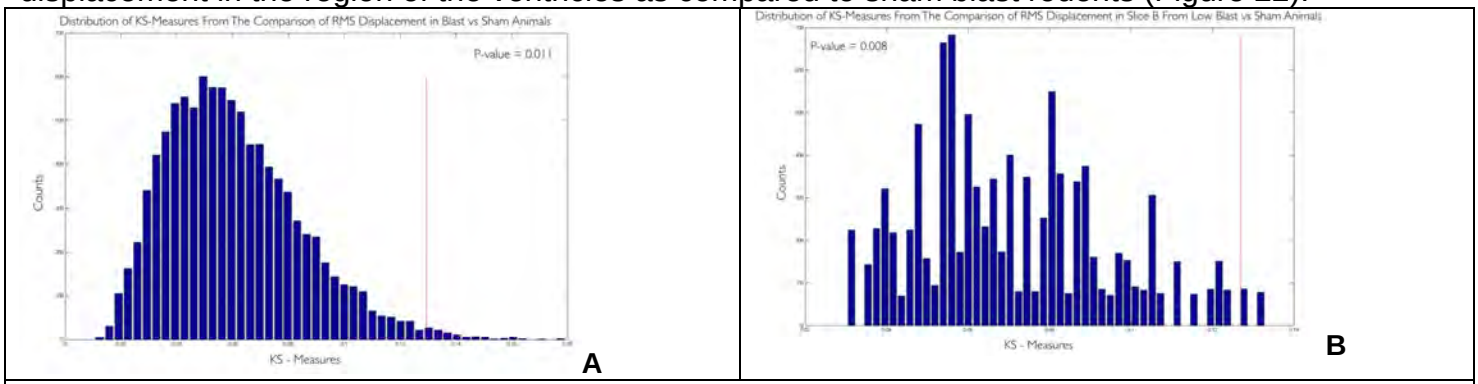

Figure 22. (A) Distribution of KS-measures comparing RMS of displacement in Blast vs Sham mice with a combination of two slices centered on the maximum volume of the ventricles (p = 0.011). **(B)** Distribution of KS-measures comparing RMS displacement in Blast vs Sham rats on a single slice (p = 0.008). The red line on each graph indicates where we would expect the distributions to center if there was no significant difference between the two groups. We are in the process of writing up these results.

Task (9): Compare images of strain, and of bulk and shear modulus of blasted rat brain with histological and MR-based images of hemorrhage, edema, ischemia and TAI.

Task (10): Compare images of strain, and of bulk and shear modulus of brain tissue with images of bulk and shear modulus derived by assigning directly measured values of bulk and shear modulus to portions of histological images.

9-10) We were able to detect (versus image) focal brain injury due to controlled-cortical impact (CCI) and due to ischemic injury, in mice and rats, acutely, 24 hours and 72 hours after injury, using shear-wave elastography, and acutely, for vibroacoustography. We could not, however, image small focal volumes of damaged brain with shear wave elastography because of their small size (roughly 0.5-1.0 cm^2) and the need to average the ultrasound signals more than anticipated. Thus far, tissue pulsatility imaging cannot image differences between CCI and sham-CCI induced damage, likely due to a need for a larger number of animals than used in our preliminary study. Happily, in human studies funded by DARPA we were able to *image* focal TBI consisting of hemorrhage and edema, using tissue pulsatility imaging (see below).

Directly measured differences in CCI brain-tissue stiffness correlate on average with ultrasound measures of stiffness. We could not, however, directly compare images with maps of stiffness, for lack of resolution in the imaging.

With regard to blast animals, we sought to detect differences between the brains of blast and sham-blast mice with vibroacoustography and, separately, tissue pulsation analysis. Again, we tried detection rather than imaging because of the small size of the brains and MRI-based indications that the ventricles of the blast animals (mice in particular) differed significantly in size from that of sham-blast animals.

We did not detect differences between blast and sham-blast mice via vibroacoustography – trends, but nothing definitive. By this measure, blast brains do not change their stiffness in a way detectable by our implementation of vibroacoustography.

In contrast, our analysis of tissue pulsatility shows statistically significant differences between the ventricular region of mice and of rats after mild blast versus after sham blast, each 24 hours after exposure, that is, the region of brain that consists of brain tissue as well as the actual ventricles. Perhaps this points to a change in brain-tissue stiffness, with blast brains appearing stiffer by this metric as compared to sham blast brains. This result may also (or instead) point to differences in cerebrovascular structure or function, which we discuss below.

Interestingly, we did not detect differences, between brain tissue pulsations of moderate/severe blast versus sham moderate/severe blast rats. Moreover, there existed little difference in brain structure (observed using histology and MRI) of rats after a single blast. Hosever, for mice, there existed subtle structural changes in brain based upon histology (the beginning of tau buildup, for example, as well as activated astrocytes, themselves tied to the capillaries) with a statistically significant change in ventricle size. Interestingly, while there exist some changes in the directly measured stiffness of rat brain after blast, this was true in only small portions of brain, while histological changes, such as they were, occurred throughout the brain.

It would appear that blast injury – versus focal contusion – may not produce a large change in brain-tissue stiffness. However, our work and that of others, point to the hypothesis that pure blast injury can produce cerebro-vascular changes with some mild alteration of axonal structure, rather than the highly sheared axons that arise in impact based injury. This is consistent with observations from the Boston group of tau proteins building up primarily near cerebral blood vessels (including capillaries), with our observations of activated astrocytes, build up of tau, as well as the observed enlarged ventricles, as examples. This view makes most promising the imaging based method we developed here based upon ultrasound's measurement of brain-tissue pulsation, itself caused by movement of blood into and through the cerebrovasculature. As we note below, we have data gathered with funding independent from this grant, that we can collect data using brain-tissue pulsation imaging paradigm from human brain, and observe changes in that pulsation caused by TBI.

Task (11): Generate first-order specifications for a device capable of imaging TBI in humans.

11) With funds from a separate unrelated grant, we have performed initial studies of tissue pulsatility imaging on humans with brain injuries. We have collected tissue pulsatility images of the areas of damage and compared them with MRI/CT of those patients (below), showing it possible that low-frequency ultrasound devices, with a carrier frequency of approximately 2 MHz or a little lower, can achieve a useful balance of skull penetration and spatial resolution of focal volumes of damaged brain.

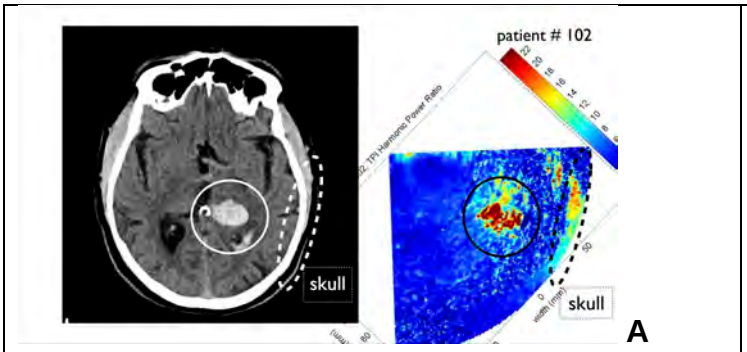

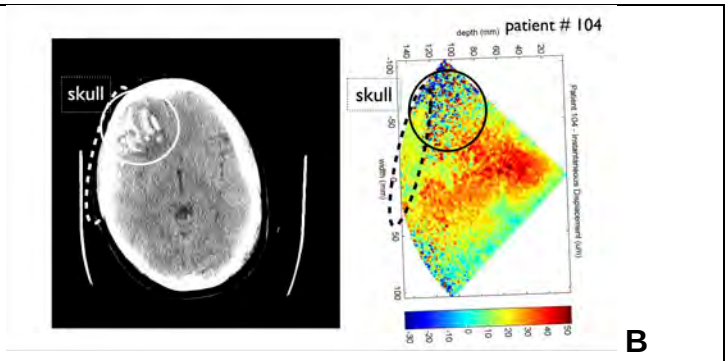

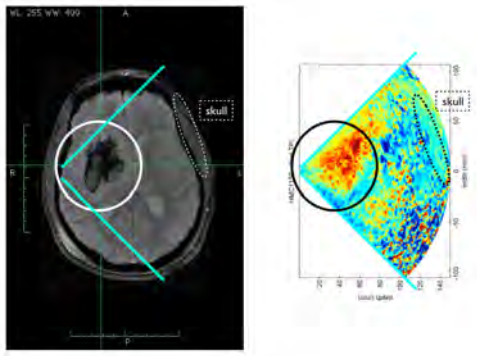

Figure 16. Comparison of CT or MR images with structural TPI images (sTPI). The same area of skull is identified in both sets of images to corroborate the location of the lesion and facilitate quantitative comparison of its size and structure. **(A)** Lesion seen in CT image (left) and sTPI (right). **(B)** Lesion seen in CT image (left) and sTPI (right)**. (C)** Lesion seen in MR image compared to corresponding sTPI. Central hemorrhage appears dark in the MR image and with enhanced peak systolic displacement in the sTPI image. The rim of edema appears as a light ring in the MR image and as an arc of reduced peak systolic displacement in the sTPI image. Measurements of maximum extent of abnormalities in each image pair shows consistent sTPI-derived values ~20% greater than that shown in standard imaging, consistent with the hypothesis that sTPI may measure abnormal vascular function in regions adjacent to injury readily observable via standard clinical imaging.

KEY RESEARCH ACCOMPLISHMENTS

- We have developed and demonstrated *in vivo* a new means of detecting severe focal (CCI-induced) TBI acutely based on generation and detection of focal, low-frequency vibration within brain via a process known as vibro-acoustography (Suarez et al, 2015). Vibro-acoustography applied to blast mouse brain did not show differences between actual and sham blast. This approach may one day find application to detection of human TBI.
- We have developed and demonstrated *in vivo* and *ex vivo* a new means of detecting moderate focal CCI-induced TBI (Xu et al, 2014) and, ischemic stroke (Xu et al, 2013), both acutely and after 24 and 72 hours, based on generation and detection of propagating shear waves within the cranium. This approach will not likely translate to human applications, because of the severe distortion of the shear-wave generating pulse of ultrasound caused by human skull.
- We have demonstrated our enablement of a novel ultrasound-based imaging system capable of translating diagnostic ultrasound images, derived transcranially, into images of endogenous brain-tissue displacement that may highlight focal CCI-induced TBI and can see changes in blast TBI, based on our ability to image *mouse- and rat-brain* pulsatility. Papers describing these results are currently under construction. This approach holds promise for translation to human use – see below.
- We have observed changes in hemispherically averaged brain-tissue stiffness in TBI generated by the controlled cortical impact (CCI) method in mice and rats consistent with physiological changes in brain observed in rodent models of TBI as well as in patients with TBI (Gabler et al, 2013). These observations include ipsilateral edema and hemorrhage formation (observed in rodents and in patients) and short-term contralateral reduction in blood flow (observed in patients and sometimes in rodents) along with a reduction in cerebral perfusion pressure.
- We have observed changes in isolated portions of rat brain 24 hours after blast injury (though not acutely), with a presentation scheduled (Alshareef et al, 2015) and full writeup of the results anticipated.
- With separate funding we have shown that the tissue pulsatility imaging paradigm refined and tested here *in vivo* can image human TBI.

REPORTABLE OUTCOMES
(copies of relevant documents are attached to the end of this document)

Gabler LF, Stone JR, Mourad PD, Crandall JR, Salzar RS (2013) Region Specific Viscoelastic Properties of the Adult Rat Brain under Indentation following Traumatic Brain Injury, Proc. Ircobi Conf., paper no. IRC-13-52, pp. 470- 482

Xu JS, Chu S, Lee RJ, Paun M, Yao A, Murphy S, Mourad PD. (2013) Evidence of diaschisis after ischemic stroke through ultrasound-based elastography. *J. Ultrasound in Medicine.* 32(3):485-494.

Xu, Z. S., Yao, A., Chu, S. S., Paun, M. K., McClintic, A. M., Murphy, S. P., & Mourad, P. D. (2014). Detection of Mild Traumatic Brain Injury in Rodent Models Using Shear Wave Elastography: Preliminary Studies. *Journal of Ultrasound in Medicine*, *33*(10), 1763–1771. doi:10.7863/ultra.33.10.1763

Chen Y (2013) Optimization of ultrasound elastography for diagnosis of traumatic brain injury. Senior Capstone Thesis with the Department of Bioengineering, University of Washington.

Suarez, M. W., Dever, D. D., Gu, X., Ray Illian, P., McClintic, A. M., Mehic, E., & Mourad, P. D. (2015). Transcranial vibro-acoustography can detect traumatic brain injury, in-vivo: Preliminary studies. *Ultrasonics*, 6–11. doi:10.1016/j.ultras.2015.04.014

Alshareef AA, Gabler LF, Stone JR, Panzer MB, Pierre D. Mourad PD. (2015) Changes in the Mechanical Response of Brain Tissue Following Primary Blast Injury. Poster presentation at the National Neurotrauma Society, Santa Fe.

CONCLUSIONS

We have generated evidence supportive of the hypothesis that ultrasound-derived brain-tissue stiffness imaging using exogeneous ‘palpation’ of brain with diagnostic ultrasound can successfully detect changes in rat brain caused by both ischemic stroke and in focal TBI. We have also generated evidence supportive of the hypothesis that we can detect endogeneous palpation of rodent brain by cerebral blood flow and that those measurements highlight differences between blast and sham-blast rodent brain that may arise due to changes in cerebrovasculature caused by the blast. We have offered to first order a design of a diagnostic ultrasound system capable of creating images of TBI in humans. Future work might most profitably target use of endogenous brain-tissue imaging to observe (1) changes in brain structure due to focal injury and (2) changes in cerebrovascular function and structure due to blast injury.

Introduction

- ❖ Motivation
  - 52-63% of traumatic brain injury (TBI) associated with explosions.
  - Approximately 360,000 soldiers in past decade
- ❖ Primary blast TBI
  - Caused by propagating pressure wave
  - Not well diagnosed; no treatment options
  - Often underreported and physical manifestations confused with other neurological disorders (PTSD, depression)
- ❖ Why Mechanical Response?
  - Better diagnostic imaging—magnetic resonance elastography (MRE) and focused diagnostic ultrasound (fDU)
    - Use prior information about how injury changes mechanical response—need to be validated and calibrated against absolute measurements.
- ❖ OBJECTIVES
  1. Develop an experimental method to study mechanical correlates to brain blast injury
  2. Identify regional and temporal changes in tissue mechanical response to primary blast

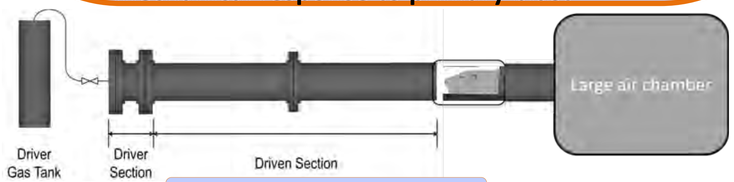

Figure 1: Schematic of Shock Tube

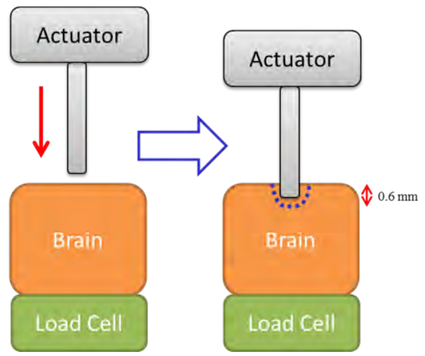

Figure 2: Illustration of Indentation Test

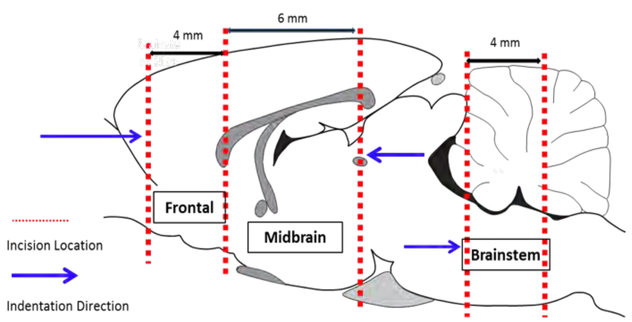

Figure 3: Coronal Cross Sections

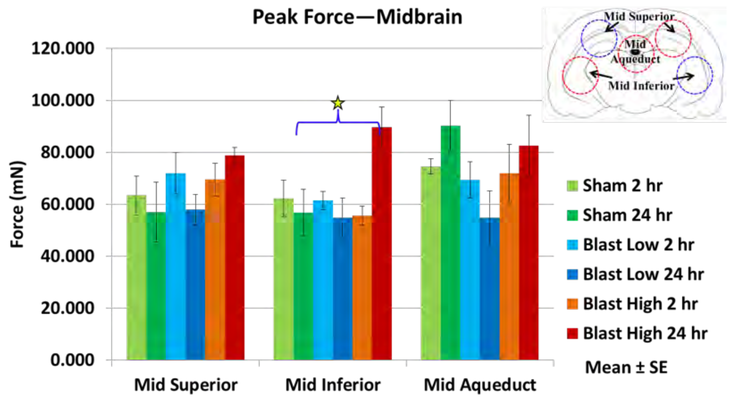

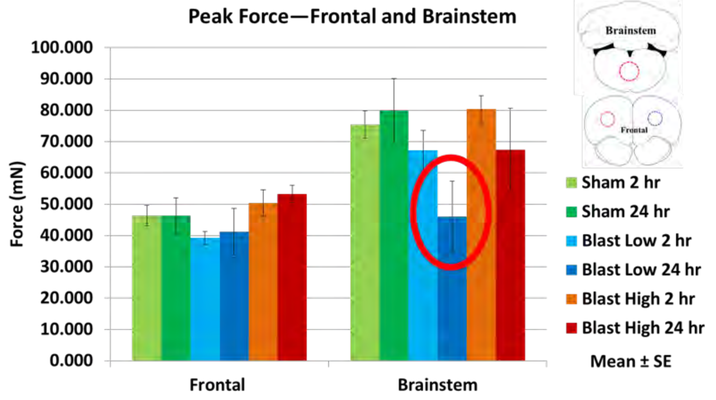

Figure 5: Peak Force Responses

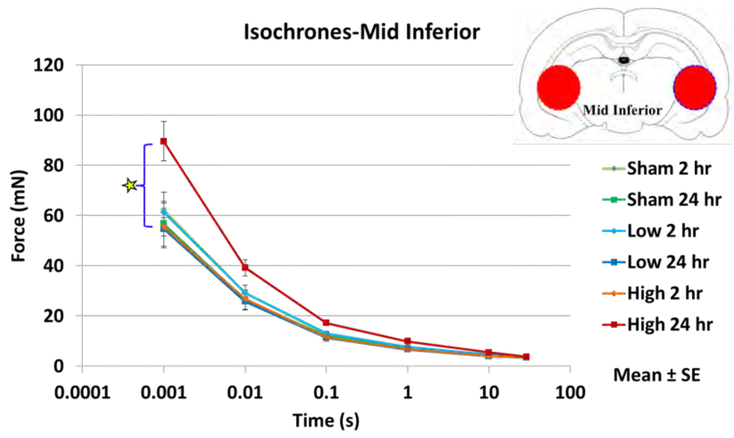

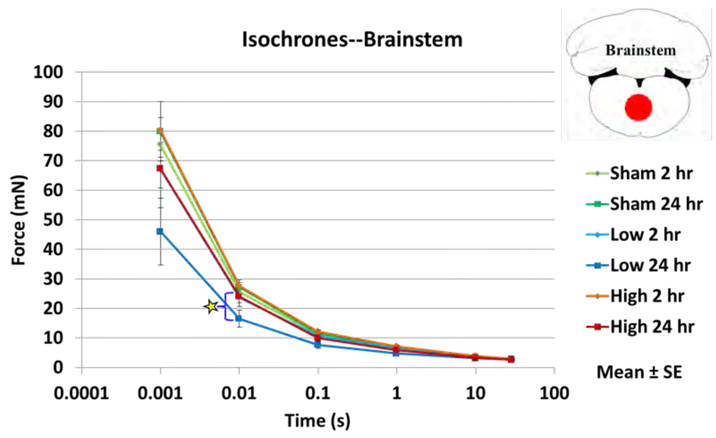

Figure 6: Force Isochrones for Indentation Tests

Methods

- ❖ Injury model
  - 30 male, adult Sprague Dawley rats
  - Blast wave generated through shock tube (Figure 1), with restrained animal facing head-on to blast.
  - Two blast levels—high (18-20 psi) and low (30-35 psi) both with 5 ms duration.
  - Sham control receiving anesthetic, placed inside shock tube but not blasted.
- ❖ Material Response Characterization
  - Indentation 30 sec ramp-hold constant strain tests (illustrated in Figure 2)
  - Three coronal cross-sections—frontal, midbrain, and brainstem (Figure 3)
  - Five regions—frontal, midbrain superior, midbrain inferior, midbrain aqueduct, and brainstem (Figure 4).
- ❖ Testing Procedure
  - Animals were sacrificed at either 2 OR 24 hours post-injury. Whole brains were extracted.
  - Thirty animals were tested, five in each group (Table 1)
  - All testing was completed within 45-60 minutes of sacrifice.

Table 1: Final Test Matrix

Treatment	#	Weight (g)
Sham 2 hr	5	296 ± 8.9
Sham 24 hr	5	279 ± 26.2
Blast Low 2 hr	5	284 ± 23.2
Blast Low 24 hr	5	274 ± 20.5
Blast High 2 hr	5	292 ± 14.6
Blast High 24 hr (1 animal died!)	4	273 ± 7.8
TOTAL	29	284 ± 19.18

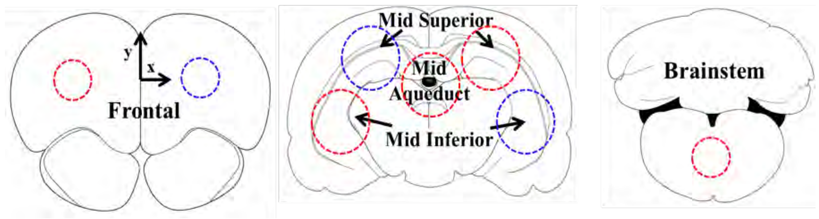

Figure 4: Indentation Regions

- ❖ Significantly l
  midbrain infe
  compared to
- ❖ Lower peak f
  region of the
  sham 24 hou
- ❖ Significantly l
  inferior of th
  time points e
- ❖ No significant
  compared to
- ❖ Forces for all
  the last time
- ❖ All forces retu
  after complet

- ❖ Previous stu
  (CCI) found 2
  injury at bot
  study finds s
  softening in
- ❖ Blast injury i
  impact to th
  response is r
  response to
  regions and
- ❖ Possible cell
  cause this ch
  blood and CS
  breakdown.
- ❖ Some limitat
  - Small sa
  - Limited
  - Assumpt
    hemisph
  - Mechani

- ❖ Presented an
  head blast TB
  mechanical ch
- ❖ Results show
  severity-depe
  - Stiffening
    high blas
  - Softening
    at 24 hou
  - No signif

Region Specific Viscoelastic Properties of the Adult Rat Brain under Indentation following Traumatic Brain Injury

Lee F. Gabler, James R. Stone, Pierre D. Mourad, Jeff R. Crandall, Robert S. Salzar

Abstract Traumatic Brain Injury (TBI) is a serious health epidemic that places high societal and economic burdens on victims and their caregivers. Further, the associated neuropathological consequences that result from TBI are often complex and cause secondary injuries that are focal, diffuse and time dependent. Current computational models can predict loading and deformation associated with TBI; however, accurate knowledge of region specific material properties from both healthy and mechanically damaged brain is needed. In this study, the mechanical properties of both uninjured and traumatically injured brain tissue are presented. Adult male Sprague-Dawley rats were injured through a controlled cortical impact protocol. Ramp and hold indentation tests were performed at five locations on the surface of tissue samples excised from whole brain specimens. Force displacement data were analyzed using quasi-linear viscoelastic theory. An analysis revealed the tissue to be viscoelastic and spatially nonlinear with mechanical properties that depend on both region and level of injury. After normalizing the data, the nonlinear components of the instantaneous elastic force and shear modulus were found to be significantly lower, 26%, in the region containing the contusion cavity on severely injured samples compared to uninjured tissue at the same region in controls.

Keywords Traumatic brain injury, focal, diffuse, controlled cortical impact, mechanical damage, quasi-linear viscoelasticity

I. INTRODUCTION

Traumatic Brain Injury (TBI) is an important national health concern in the United States [1]. Approximately 1.7 million incidences and 52,000 deaths are reported annually due to automobile collisions, sports accidents, falls, and other head impacts [1]. Further, severe TBI has a high economic burden, costing nearly $76.5 billion each year in medical and societal costs [1]. On the battlefield, improvised explosive devices have led to TBI in as many as 62% of soldiers sustaining head injuries, and an estimated 360,000 service members have been affected by TBI over the past decade [2], [3]. Since the 1960s there has been a dramatic improvement in understanding the complex pathobiological behavior associated with TBI [4]. Brain injury, as a result of an impact or insult to the head, leads to a number of complex neuropathological consequences that result in further tissue dysfunction and eventually cell death [5]. However, injury quantification remains challenging because the neurochemical cascades that accompany TBI often involve complex secondary sequelae that are focal, diffuse, and time dependent [6]. A better understanding of the mechanical response of the brain during these events would improve diagnosis and treatment of TBI in both clinical and battlefield scenarios.

The material properties of brain during an injurious event were studied as early as the 1940s [7]. Not until more recently has an emphasis been placed on understanding the complex mechanical behavior of the brain during loadings that lead to TBI. Much of this can be attributed to an increase in awareness of the damaging, long-term effects following even mild brain injuries [1]-[3]. Material properties of brain are reported in the literature as viscoelastic [8]-[13], both spatially and temporally non-linear [9], [10], anisotropic [11], age-dependent [11]-[14], inhomogeneous [12], [13] and nearly incompressible [15]. Additionally, experimental factors such as specimen preparation, temperature [16] and level of hydration [14], [17] have been shown to influence these properties. There is considerable variation in the mechanical response reported in these

L.F. Gabler, B.A., J.R. Crandall, Ph.D., and R.S. Salzar, Ph.D., Department of Mechanical and Aerospace Engineering at the University of Virginia's Center for Applied Biomechanics, 4040 Lewis and Clark Drive, Charlottesville, VA 22911 USA (phone: (434) 296-7288 ext. 164, email: lfg4dc@virginia.edu). J.R. Stone, M.D., Ph.D., PI, Department of Radiology and Medical Imaging at the University of Virginia. P.D. Mourad, Ph.D., PI, Department of Neurological Surgery at the University of Washington.

studies. Much of this variation can be attributed to differences in the type of species, experimental protocols, and anatomical regions tested. Still, no definitive set of material properties exist for brain.

Computational models of TBI are commonly used to study the mechanical behavior of brain tissue during a traumatic event. Finite element modeling (FEM) can predict loading of various substructures through simulations of mild to severe TBI in rat brain [18]. These simulations have the added capability of predicting injury, because model-prediction of tissue strains were shown to correlate well with experimentally determined strain and strain rate injury tolerance criterion [19]-[21]. For more region-specific predictions of injuries, local material properties, including both traumatically injured and healthy brain tissue, need to be determined. Such knowledge would provide existing computational models with the added ability to predict the subsequent mechanical response of damaged tissue and allow for a better understanding of brain excitotoxicity beyond that of the initial trauma.

A survey of the literature revealed a number of studies that report thresholds for axonal damage. The reported mechanical limits for diffuse axonal Injury are between 0.1-0.2 Lagrangian strain at strain rates greater than $10s^{-1}$ [9], [19]-[22]. However, there is little information regarding changes in the mechanical properties of traumatically injured brain tissue. Shafieian et al. [23] used an impact acceleration model (IAM) to generate diffuse axonal injury (DAI) in the brainstem of adult male Sprague-Dawley (SD) rats. They reported a 35% reduction in the linear coefficient of the instantaneous shear modulus in injured rats compared to uninjured controls. Saxena et al. [24] studied traumatic spinal cord injury in adult female SD rats over the course of 2 and 8 weeks post injury. They observed a 50% reduction in elastic modulus for injured compared to healthy tissue. The goal of this study is to acquire accurate, region-specific material properties for both traumatically injured and uninjured rat brain to better understand the mechanical behavior of damaged tissue and to improve existing models of TBI.

II. METHODS

Animal Injury

All animal protocols were approved by the University of Virginia's Institutional Animal Care and Use Committee. Twenty adult male SD rats of average weight (mean ± SD), (320±27)gram, underwent surgical procedures for this study. Anesthesia was induced with a mixture of 4% isoflurane and 100% medical grade O_2 for 3-4 minutes in an induction chamber. Once the animals were sedated, the level of isoflurane was reduced to 2-2.5% and maintained for the duration of the surgery. The animals were then placed in a stereotaxic reference device (MyNeuroLab Leica Digital Stereotaxic Instrument, Leica Biosystems, Richmond, IL) and prepared for injury. A midline scalp incision was made along the forehead of each animal. The skin and underlying soft tissue were retracted exposing the sagittal, coronal, and lamboid sutures on the skull. A 4.5-5mm diameter hole was drilled from the skull above the right cerebral cortex exposing the dura at the coordinates of injury: A = -4mm bregma and L = 2mm (Ideal Micro-Drill™, Harvard Apparatus, Holliston, MA). An electromagnetically driven controlled cortical impact (CCI) device (MyNeuroLab Leica Impact One, Leica Biosystems, Richmond, IL) was used to deliver repeatable, severe, open head injury to nine of the animals; the remaining animals were prepared for *Sham* injury and used as controls. The 2mm diameter impact cylinder was positioned directly on the dura at the coordinates of injury. Contact between the probe tip and dura was verified via an electric circuit. The probe tip was then retracted from the dura and injury parameters were inputted to the device. Severe traumatic brain injury was delivered to the right ipsilateral cortex through a rapid 2.5mm compression of the dura, sustained for 200ms, with an initial impact velocity of 3.5m/s. In the instance of Sham injury, the impact probe was retracted from the dura, but no impact was performed on the tissue. The animals were then resuscitated and monitored for a period of twenty-four hours after which they were sacrificed and their brain tissue immediately collected.

Sample Preparation

Whole brain specimens were prepared for indentation tests immediately following tissue collection. To reduce the effects of temperature and level of hydration on the results, specimens were submerged in a physiological buffer (Millonig's Phosphate Buffer) for five minutes at room temperature (19-20)°C. Hydrated specimens were then placed into a coronal slice matrix (Braintree Scientific, Inc.) with incision planes spaced 1mm apart. Tissue cross-sections were cut to approximately 8mm in thickness from each whole brain specimen

using a 0.23mm thick razor blade (VWR Scientific, Media, PA). To accomplish this, two incisions were made in the coronal plane and parallel to each other. The first incision was made 1mm posteriorly to the injury plane at -5mm bregma and the second 8mm anteriorly to the first at 3mm bregma. In both Sham and severely injured specimens, the injury plane was identified by petechial hemorrhage on the dorsal surface of the tissue. However, in the case of a severe injury, the hemorrhage was more extensive and included a *contusion cavity*. Samples were then removed from the slicing matrix and placed on an aluminum test stage with the 5mm bregma coronal plane oriented upwards. The thickness of each sample deformed approximately 1mm under its own weight. The weight and dimensions of each sample were measured and recorded.

The coordinates of five regions, A-E, on the samples were determined using a stereotaxic reference frame [25] and are illustrated in Figure 1. Substructures of the brain under the indenter at these coordinates included both healthy and damaged tissue within the cerebral cortex, corpus callosum, hippocampus and midbrain. For severely injured samples, region A was located directly over the contusion cavity and within the injured hemisphere of the brain. Samples were assumed to be symmetric about the cerebral fissure, and regions B and D were located contralateral to regions A and C, respectively. Region E was positioned at approximately the center of the sample on the aqueduct. Coordinates were normalized to account for differences in the cross-sectional dimensions between samples due to intra-specimen variability. The normalization was performed by making length and width measurements on the cross-section of each sample; the five indentation coordinates were then multiplied by the ratio of the cross-sectional dimensions of the first sample tested under this protocol, ID NIB00287, to those of the sample of interest; the normalized coordinate locations were then dimensioned from region E using digital micrometers. Evan's Blue Dye was used to mark each coordinate on the tissue cross-section for a visual reference onto which the indenter could be positioned. The amount of dye under the indenter was assumed to have a negligible effect on the tissue properties. A total of 30 minutes were allotted for sample preparation, i.e. from the time of tissue collection to the time indentation testing began.

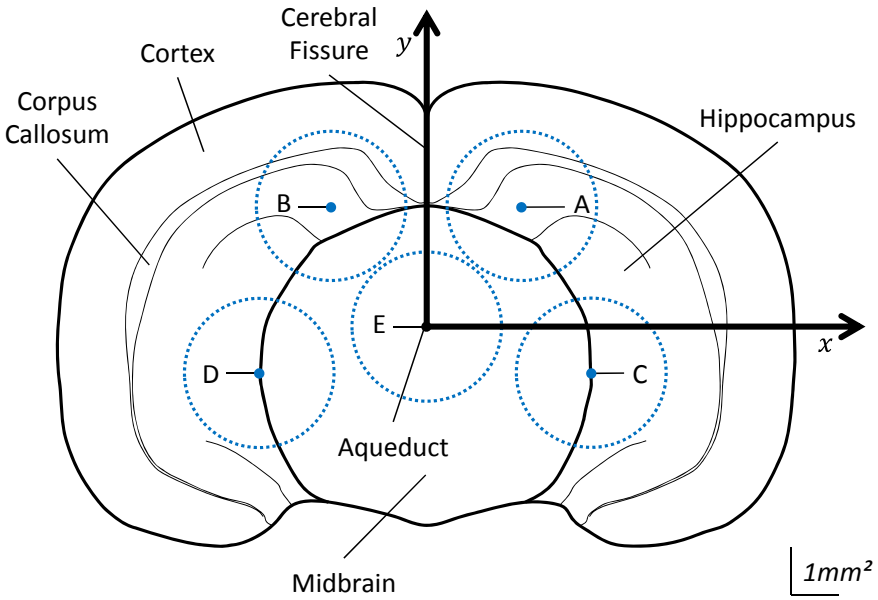

Figure 1: Schematic of a tissue sample showing the coordinate locations of the five un-normalized indentation regions (x, y): A = (2, 2.5), B = (-2, 2.5), C = (3.5, -1), D = (-3.5, -1) and E = (0, 0). Dashed circles represent the cross-sectional area of the indenter overlaid onto the tissue sample.

Indentation Testing

The aluminum test stage with sample was mounted atop a 50gram load cell (Model 31 Low, Honeywell International Inc., Golden Valley, MN), and beneath a 3.18mm diameter plane-ended cylindrical indenter mounted to a linear actuator equipped with an LVDT to measure displacement (ElectroForce® 3100 Test Instrument, Bose Corporation – ElectroForce Systems Group, Eden Prairie, MN). Excess compliance in the test frame due to the motion of the actuator induced an inertial based force response in the load cell. A 500g linear accelerometer (Model#: 7264B-500, Humanetics Innovative Solutions, Plymouth, MI) was mounted to the test stage to subtract off this effect. Force, displacement, and acceleration data were acquired at 20kHz (DEWE-

2010, Dewetron Inc., Wakefield, RI). Regions were tested in a randomized order for each experiment. At each coordinate the indenter was centered on the Evan's Blue Dye. This was accomplished by mounting a 1.3mm diameter spherical tip punch to the actuator and positing directly over the dye via visual inspection. The spherical punch was exchanged with the plane-ended cylindrical indenter, which was assumed to be centered over the indentation coordinate. The indenter was advanced slowly toward the tissue at a rate of 0.01mm/s until a tare load of 0.3gram was achieved. The indenter tip was then pressed 0.6mm into the tissue, normal with respect to the local surface, in approximately 8ms and then held for 30s to measure the tissue's relaxation. A peak displacement velocity of 120mm/s, at an approximate strain rate of $17s^{-1}$, was observed during the ramp portion of the displacement. After each test the indenter was carefully removed from the tissue. Five minutes were allotted between tests to allow for tissue recovery and instrumentation adjustments [26]. The tissue was sprayed with Millonig's in between each indentation test. The protocol was repeated for the remaining four regions and all testing was completed within 75 minutes of animal sacrifice.

Mathematical Modeling

All data were filtered in accordance to the SAE-J211 standard, CFC 1000, using a zero-phase, digital IIR 8 pole butterworth filter at a Low Pass frequency of 1650Hz. The data were resampled in a logarithmically scaled time step to give equal weights to both ramp and hold portions of the test. Samples were assumed to be incompressible and isotropic [9], [10]. The force response, $F(h,t)$, to the displacement input, $h = h(t)$, was modeled using a quasi-linear viscoelastic (QLV) mathematical framework [27]:

$$F(h,t) = \int_0^t G(t-t')\frac{\partial F^e(h)}{\partial h}\frac{\partial h}{\partial t'}dt' \tag{1}$$

where $F^e(h)$ is the instantaneous elastic response, $G(t)$ is the reduced relaxation function, t is the time, and t' is a dummy variable over which the convolution integral (1) is evaluated. The instantaneous elastic response was modeled using the solution to the Boussinesq problem for a flat-ended cylindrical punch [28]:

$$F^e(h) = \frac{4R\kappa\mu}{1-\nu}h \tag{2}$$

where R is the radius of the indenter, ν is Poisson's ratio, which was assumed to be 0.5, μ is the shear modulus, and κ is a constant used to incorporate the effect of substrate on finite sample thickness [29]. Values of κ were obtained for each sample and found to be between 1.26 and 1.3. The shear modulus was chosen to be a second-order, even function of h to capture the spatial nonlinearity of the tissue [23]:

$$\mu = \mu(h) = \mu_0 + \mu_2 h^2 \tag{3}$$

where μ_0 and μ_2 are the *instantaneous linear* and *nonlinear shear modulus coefficients*, respectively. Using this form for the shear modulus results in

$$F^e(h) = F_1 h + F_3 h^3 \tag{4}$$

where F_1 and F_3 are the *linear* and *nonlinear coefficients* of $F^e(h)$, respectively, described in (2). The mathematical solutions for the values of μ_0 and μ_2 in terms of F_1 and F_3 are determined through the use of equations (2-4).

$$\mu_0 = \frac{1-\nu}{4R\kappa}F_1 \qquad\qquad \mu_2 = \frac{1-\nu}{4R\kappa}F_3 \tag{5}$$

A six term prony series with five time constants was chosen to model the relaxation behavior of the tissue:

$$G(t) = G_\infty + \sum_{i=1}^{5} G_i \cdot e^{-\frac{t}{\tau_i}} \qquad \text{under the constraint that} \qquad G_\infty + \sum_{i=1}^{5} G_i = 1 \tag{6}$$

where G_i's are the normalized relaxation coefficients of the corresponding time decades and G_∞ is the coefficient of the steady-state response. Values for the thirteen coefficients F_1, F_3, τ_i, G_i, for i=1 to 5 and G_∞ were determined through a reduced gradient algorithm (Excel Solver®, Microsoft®, Redmond, WA) that was used to minimize the sum squared error between the model-predicted force, resulting from numerical integration of (1), and the experimental data. An individual set of optimal coefficients was determined for each indentation test. Preliminary analysis of the model fit to the first few data sets; test ID NIB00288A through NIB00288E, indicated marginal variability in the values for the optimized time constants, τ_1≈0.001s, τ_2≈0.01s, τ_3≈0.1s, τ_4≈1s, τ_5≈10s. To simplify the model the time constants were fixed at theses decades for the remainder of the analysis and only eight parameters needed to be optimized through model fitting.

Statistics

The number of terms, i, in equation (6) were determined via an F-test [30]. Data from test ID NIB00318E was modeled with four, five, and six time constants to see if there was a statistically significant improvement in the model's fit to the data. The model with five time constants gave a significantly better fit (F≈9, p < 0.001) than the model with four time constants and the model with six time constants showed no improvement in fit over five time constants (F≈0, p≈1). Therefore the model with five time constants was chosen for the analysis. The critical F-statistic at the α=0.05 level of significance for both tests was F_c ≈1. A total of n=8 indentation tests were performed per region, A-E, and per injury treatment, Sham and severe injury, for a total of 10 groups. For each group, an average $F^e(h)$ and $G(t)$ were determined using least squares optimization between the average and the eight individual measurements. The coefficients of the shear modulus, μ_0 and μ_2 were calculated from F_1 and F_3 of the eight individual curves using expression (5). An average μ_0 and μ_2 were then determined for each group. Additionally, the coefficients of $F^e(h)$ and $G(t)$ at regions A and C were normalized to the values at the contralateral regions B and D, respectively. Specifically, normalization was performed by dividing the value of a particular absolute coefficient F_1, F_3, μ_0 and μ_2 at region A by its corresponding absolute contralateral value at region B. For example, F_1 from indentation test ID NIB00290A was divided by F_1 from indentation test ID NIB00290B, etc. The process was repeated for the coefficients at region C, dividing by the corresponding contralateral values at region D. The absolute structural and material properties (F_1, F_3, μ_0, μ_2, G_i, for i=1..5 and G_∞) were compared separately to evaluate for the effect of region and injury treatment using a two-way ANOVA. *Post-hoc* comparisons were made using a student's t-test with the appropriate Bonferroni correction. Samples were assumed to be independent measurements of a particular tissue property, normally distributed and homoscedastic. To evaluate the differences observed in the normalized ratios, student's t-tests with a Bonferroni correction were used to make comparisons across injury treatment at a particular region. Specifically, a direct comparison was made between the normalized ratios of Sham and severely injured tissue at region A to evaluate the effect of injury at the location of the contusion cavity.

III. RESULTS

Eighty indentation tests were performed on the tissue samples, and data from 16 of the original 20 animals were used in analysis. The tissue from animal ID NIB00311 was damaged upon collection and the data from 3 additional experiments were compromised due to either unpreventable noise from the surroundings (animal ID NIB00287), or experimental error (animal IDs NIB00295 and NIB00298). Average $F^e(h)$ and $G(t)$ for region and injury treatment are shown in Figure 2. Region specific, *absolute* structural and material properties, *normalized* ratios, and results of the t-tests are reported in Table 1 (see appendix). ANOVA indicated significant (p < 0.05) main effects of both region and injury treatment on the absolute coefficients. On average, F_1 and μ_0 were higher (p < α=0.005) in region E compared to region A (F_1: +36.3mN/mm, p=0.002 and μ_0: +2.23kPa, p=0.002). The relaxation coefficient, G_1, was found to be higher while G_3 and G_∞ were lower (p < α=0.05) in severely injured samples compared to Sham controls (G_1: +0.011, p=0.0164, G_3: -0.003, p=0.008, and G_∞: -0.003, p=0.044). The student's t-test, revealed a significant decrease (p < α=0.025) in the value of the normalized ratios of F_3 and μ_2, (-26%, p=0.0084 each), in severely injured tissue compared to Sham controls. Conversely, the t-tests revealed a significant increase in the normalized ratios of F_3 and μ_2, (+38%, p=0.0156 each) on severely injured compared to sham controls in region C. The percentages reported here are calculated as percent differences in the sample means from Sham samples.

(Region A)

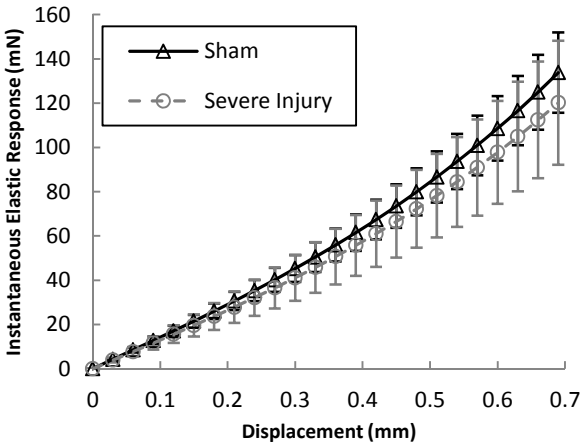

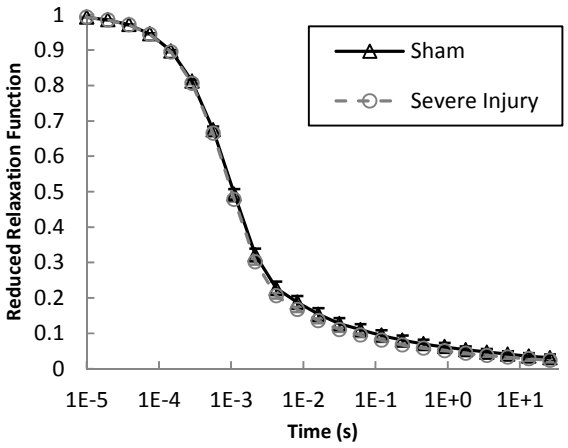

(Region B)

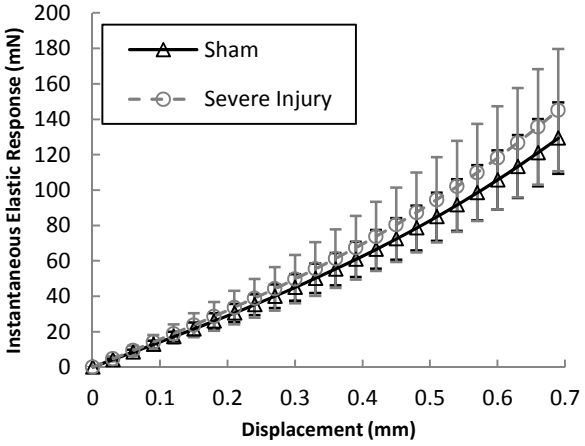

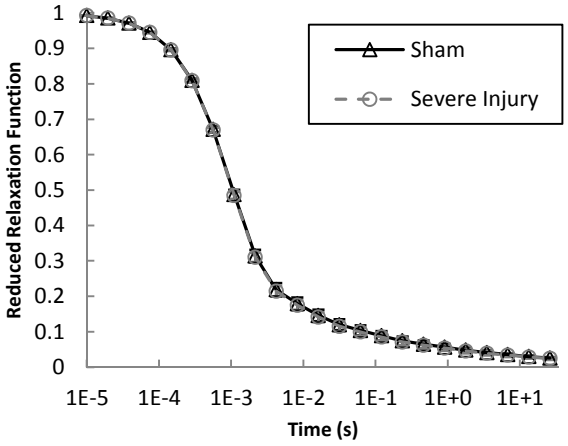

(Region C)

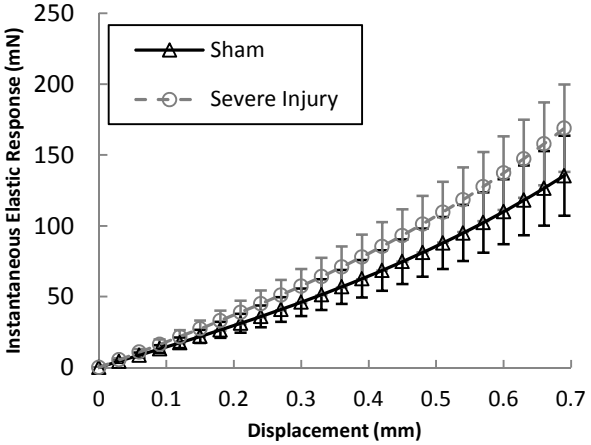

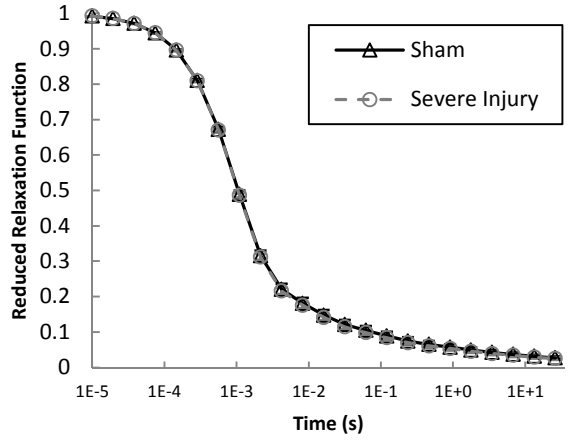

(Region D)

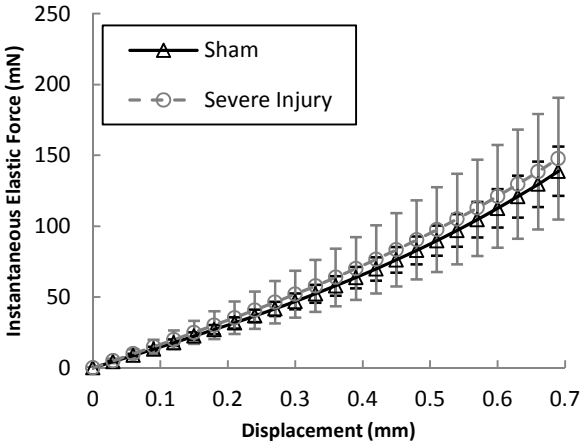

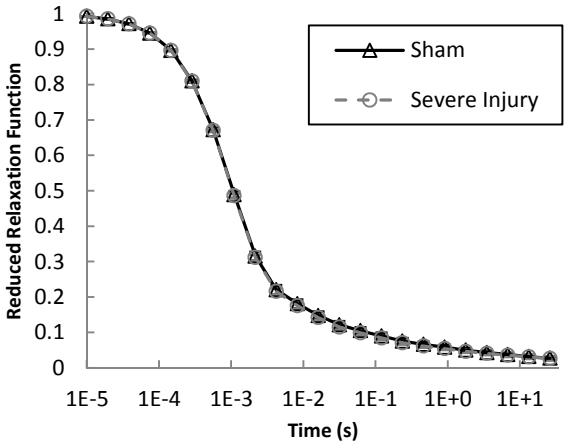

(Region E)

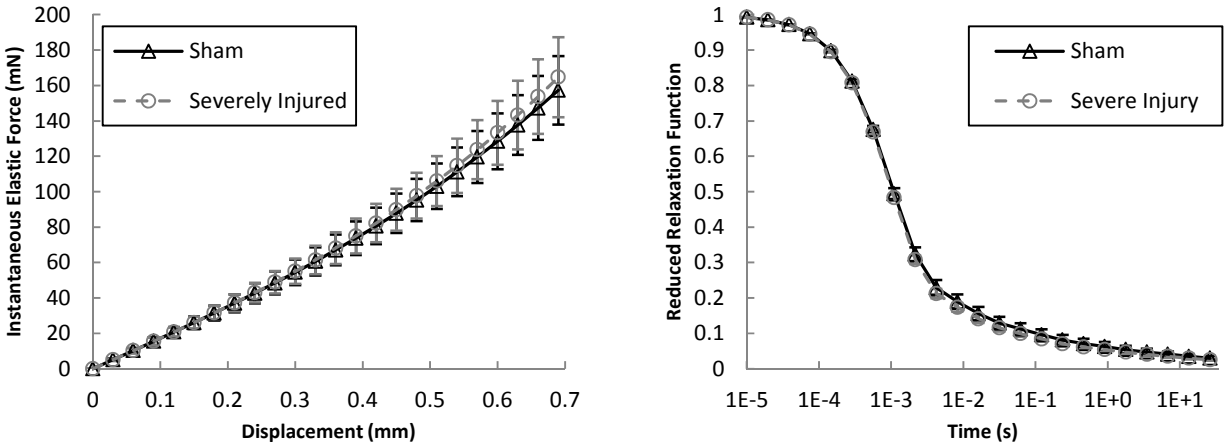

Figure 2: Average $F^e(h)$ and $G(t)$ for region and injury treatment. Error bars are 95% Confidence Intervals. Average $F^e(h)$ curves for severe injury were on average stiffer than the average Sham curves in all regions except for region A. The reduced relaxation functions were nearly identical in all cases.

IV. DISCUSSION

This study found the mechanical properties of the rat brain to be viscoelastic, spatially nonlinear, and dependent on both region and injury treatment. A linear viscoelastic model was fit to the experimental data, in addition to the QLV model, where equation (3) was assumed to be a function of μ_0 only. With the same number of prony series terms, the fits of both the linear and QLV models were visually assessed using tissue force time histories, and compared statistically using the F-test, Figure 3. The linear model fit the data well during the first of half of the ramp and long term relaxation of the tissue; however, the addition of the nonlinear term through QLV showed a statistically significant improvement in the model fit ($p < 0.001$) to the experimental data, capturing the entire ramp, peak force, and initial tissue relaxation, Figure 3a. To justify the use of QLV over a fully nonlinear viscoelastic model the ratio of the relaxation forces from two different displacement steps were calculated and then checked to be approximately constant in time using linear regression. Two displacement steps, the first to 0.6mm and the second to 1.2mm, were applied to tissue from a severely injured animal; ID NIB00291 at region A and region E. Results from the linear regression were used to evaluate whether or not the slope of the force ratio was statistically significant from zero. Data up to 100ms after the peak force were not included in the analysis due to transience of the displacement ramp. The value of the regression coefficient, the slope, was found to be statistically significant (slope = $0.035s^{-1}$, $p < 0.001$) at region A and (slope = $0.007s^{-1}$, $p < 0.001$) at region E. However, the magnitude of the slope was not thought to be meaningful. That is, the ability to detect small changes in the value of the slope was due to the large amount of data being used, and that the resulting values were not influential, suggesting a relatively constant response over time. These results indicated that the relaxation behavior of the tissue was independent of displacement and that no temporal nonlinearities were observed up to approximately 18% sample penetration.

(a)

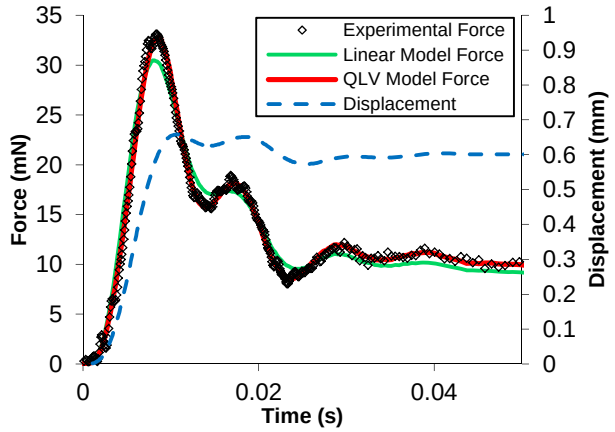

(b)

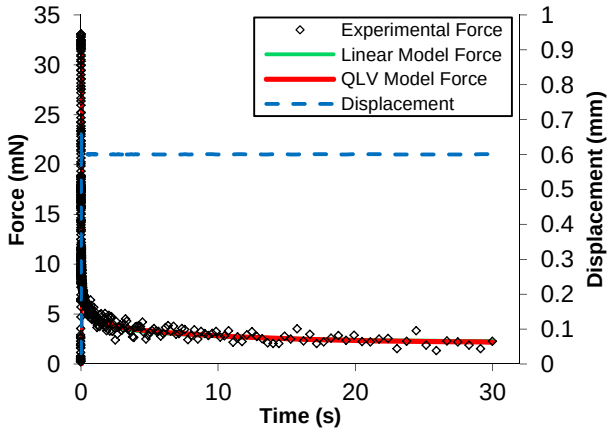

Figure 3: Examples of the QLV model fit to the experimental data for both the ramp (a) and hold (b) portions of an arbitrarily chosen indentation test (NIB00308B). The QLV model followed the experimental data more closely than the linear model during the ramp, peak, and initial relaxation of the tissue (a). Both models followed the data closely during the hold portion of the test (b). A similar result was observed when modeling other experimental data. The increase in force near 16ms and 30ms is due to the increase in displacement of the indenter into the tissue at these times.

Validation of the test methodology selected for the current study involves a comparison to other brain studies reported in the literature. The absolute mechanical properties and uncertainties found in the current study are consistent with those determined experimentally for shear [9], [31], compression [32] and indentation [23]. Further, the data fit within the reported range of shear moduli for brain tissue (0.1-22) kPa [8]-[16], [23] and [32]-[34]. Darvish and Crandall characterized bovine brain using QLV under oscillatory shear tests up to 200Hz and 20% Lagrangian strain [9]. They observed 16kPa and 2.62kPa for the linear and nonlinear instantaneous elastic shear moduli, respectively. On the other hand, Takhounts et al. tested both bovine and human brain up to 100% Lagrangian shear strain in ramp and hold tests and determined the instantaneous linear shear moduli to be approximately 2kPa and 1.5kPa, respectively [10]. Shuck and Advani found large variability in the shear modulus [31]. They performed oscillatory torsion tests on human brain up to 60Hz and observed (3-16)kPa. In each of these studies the brain was modeled under the assumptions of isotropy and incompressibility.

In regards to the results reported for indentation studies, Gefen et al. tested both young and mature rats in vivo and in situ under spherical indentation, and determined values for the instantaneous shear modulus between (1.2-3.3)kPa [15]. Further, Gefen and Margulies [33] compared the effects of in vitro, to in vivo and in situ on the material properties of porcine brain. They used a hemispherical indenter and found the short term shear modulus between (0.7-2.8)kPa. In both studies preconditioning was found to significantly reduce the value of the shear modulus and in vitro results tended to be lower than in vivo and in situ. Samples were not preconditioned in the current study as work by Shafieian et al. [23] suggests preconditioning may have damaged their samples and reduced the effect of injury. Various other studies have used micro-indentation to determine region specific material properties in rat brain [13], [34]. These studies observed values for the short term shear modulus on the order of (0.1-1.5)kPa, nearly one order of magnitude lower than the values reported in the current study. The material properties of brain have shown to be rate sensitive and increase with increasing strain rate or frequency [9] [10]. The load rates reported in these studies were less than 1mm/s, (0.4-0.5)s^{-1}, and much less than that of the current study which could explain this discrepancy. Additionally, these studies performed indentation tests up to depths of 40μm on the surface of tissue cross sections that had previously been blocked and then mechanically cut using a vibratome. Consequently, their findings may have been significantly altered from that of normal, healthy tissue. The tissue samples tested in the current study were hand cut and tested in vitro. As a result of sample preparation, a thin layer on the surface of the tissue likely sustained damage. Even though the indentation depths used in the current study were much higher than those used in micro-indentation, it is reasonable to expect some alterations in the mechanical properties from that of normal, healthy, living tissue.

In a similar study to the current, Shafieian et al. performed cylindrical indentation at two locations, PDx and PmJ, on the brainstem of impacted rats and found a statistically significant reduction in $F^e(h)$ between uninjured and injured specimens [23]. They reported values for μ_0 and μ_2 between (1-10)kPa and (1-25)kPa/mm^2, respectively with similar uncertainties to that of the current study. The reported reduction in μ_0 between injured specimens and Sham controls was 35%. This value was an average taken from both preconditioned and un-preconditioned samples and found to be in agreement with the work of Darvish and Crandall [12] who reported a 33% reduction in the linear shear modulus after non-recoverable strain conditioning. However, Shafieian et al. did not specify the significance of change in μ_0 and μ_2 with respect to injury treatment, making it unclear which parameter, if any, was driving the reduction in shear modulus after tissue damage [23]. On average, they saw a 28% and 47% reduction in μ_0 and μ_2, respectively, for un-preconditioned samples at PDx. Further, they observed a 14% and 29% reduction in μ_0 and μ_2 for un-preconditioned samples at PmJ; however, this result was not statistically significant. In the current study μ_0 and μ_2 were reduced on average 17% and 26%, respectively at the location of the contusion cavity, region A. This was observed after normalizing the data and the reduction in μ_0 was not statistically significant. In the case of

the absolute material properties, the observed differences in μ_0 and μ_2 between severely injured and Sham samples were not significant. Additionally, the reported 38% increase in μ_2 at region C on severely injured compared to sham tissue contradicts the findings for the normalized properties at region A. Further investigation into this matter is needed; however there was no evidence of mechanical damage in this region when compared to the visible damage of the contusion cavity in region A.

Possible reasons for these discrepancies can be attributed to a number of factors. In the current study, a CCI model was used to deliver injury directly to the cortex [35]. On the other hand, Shafieian et al. chose an impact acceleration model to generate DAI in the brainstem due to its predictable pattern of injury there [23], [36]. Further, regions tested in the current study incorporate both white and grey matter and are heterogeneous compared to the brainstem which is comprised of predominantly white matter and is relatively homogenous and stiffer than the cortex [37]. Another explanation for these discrepancies is the rate at which the tissue samples were loaded under indentation. Peak Loading rates determined from the tests conducted by Shafieian et al. [23] were between (16-33)mm/s, (8-16)s^{-1}, while that of the current study was approximately 120mm/s, 17s^{-1}. High rate inputs are necessary to characterize the mechanical response of the brain during TBI [38]. The peak loading rates reported in the current study are within the range of those reported for impact traumas [13], [38], and [39]. An understanding of the brain's mechanical response at high load rates would be useful for computational models of these events. However, testing at these rates may cause further damage to the tissue and reduce the effect of injury on the mechanical properties. Strain and strain rate tissue tolerance thresholds have previously been studied and the reported values associated with axonal injury are between 0.1-0.2 Lagrangian strain with strain rates greater than 10s^{-1} [9], [19]-[22].

The hypothesis that the tissue samples were damaged upon loading was examined in a separate analysis. A QLV model with only 1 time constant τ_1= 0.001s was fit to the ramp portion the experimental data (n=16) for region A. The form of $F^e(h)$ was kept the same as expression (4). The model was fit in three ways. The sum squared error was minimized between the model and experimental forces from: (1) the toe region to the force corresponding to the peak loading rate; (2) the force corresponding to the peak loading rate up to the peak force; and (3) over the entire ramp from the toe region to the peak force. Average $\mu_0$and μ_2 were determined from the (n=16) individual fits. ANOVA revealed significant ($p < 0.05$) differences between the three model fits. Post-hoc Bonferroni comparisons were made between individual samples and revealed the following information. The value of μ_0 was approximately constant across all three models, while the value of μ_2 decreased by 34% ($p < 0.001$) after the peak displacement rate of 120mm/s. This observation was made independent of injury treatment. The stability of the model was evaluated during each of the three fits due to the relatively small amount of data being fitted. Regardless of initial inputs, model parameters optimized to the same values, indicating a stable solution. These results suggest that the tissue may have been damaged during loading up to 5% tissue penetration and at a peak rate of 17s^{-1}.

V. CONCLUSIONS

This study presents an experimental methodology and analytical framework for modeling the region specific structural and material properties of mechanically injured and uninjured brain tissue. Force data were acquired under high rate loading inputs in the range of those related to impact traumas. Quasi-linear viscoelasticity, a popular, constitutive model that is commonly used to model soft biological materials was chosen to fit the experimental data over both linear and fully nonlinear viscoelastic models. The tissue was assumed to be isotropic and incompressible for model simplification. The mechanical properties were found to be viscoelastic, nonlinear, and regionally dependent. Additionally, these properties were quantified under a well characterized injury model capable of delivering repeatable levels of mechanical damage directly to the dura. To the authors' knowledge, this is the first study to examine the mechanical properties of the brain after CCI. The results for the shear modulus were within the range reported in the literature for shear, compression, and indentation tests. The material and structural properties were found to be roughly constant across region and injury treatment. However, after normalizing the region specific mechanical properties in regions A and C, there were statistically significant differences in the values of the nonlinear coefficients of the instantaneous shear and elastic response. A 26% reduction in the nonlinear material and structural coefficients were observed in severely injured samples compared to healthy controls at the location of the contusion cavity. The utility of this research is crucial for understanding the mechanical response of the brain after TBI. Knowledge of such

material properties may be useful to uniquely identify different types of brain injury and to better understand the mechanics of repetitive brain injuries.

VI. LIMITATIONS

There are a number of limitations that may influence overall response of the tissue samples during mechanical loading. First, the solution to the Boussinesq problem assumes indentation of a semi-infinite elastic half-space. The samples used in the current study have finite boundaries and exhibit damping as well as elastic properties. This solution was modified by [29] to incorporate the effect of a rigid substrate on finite sample thickness. The corrective factor κ was developed for indentation on articular cartilage and subsequently applied to indentation tests performed on other soft biological tissues including brain [13], [23]. The factor κ functions to reduce the applied load, measured within the tissue, by an amount that depends on the ratio of the indenter radius to sample height. As the indenter radius increases or sample height decreases, higher forces are transmitted from the substrate to the tissue. To avoid the effect of substrate on mechanical properties, a common rule of thumb is to limit indenter penetration to depths of no greater than 10% of the total sample thickness [40]. Penetration depths in the current study obey this rule. However, more recent work has observed noticeable substrate effects within 10% penetration and claim that the ratio of the indenter radius to sample height must be kept within 10% [41]. The ratio of radius to sample height is 20% in the current study and κ was implemented to adjust for this limitation. In addition to substrate effects, other boundary conditions have been violated. In all regions except E, the distance between the indenter and edge of the tissue sample was less than the recommended distance of one indenter's width. This would have the effect of reducing the material properties observed in regions A-D compared to E. Indenter interference is an additional concern in this study. The process by which the coordinates were dimensioned on the surface of the tissue was imperfect. Slight offsets in the dimensioning may have led to overlapping indentation tests. Further, the indentations made on the surface of the samples were within one diameter of each other. However, adequate time was allotted for tissue recovery in between subsequent tests. Finally, contusion cavities can be problematic for material studies [23]. They are often near the edge of the sample and create discontinuities in the tissue surface making it difficult to obey boundary conditions under most mechanical tests. It is suggested that future studies involving contusion cavities be made in vivo or situ with the brain left in the skull.

A number of studies including the current have used the F-test to statistically determine an appropriate model for fitting experimental brain data [13], [23], [34]; however, there are limitations. The F-test assumes the data to be independently measured and normally distributed. In addition, there must be a linear relationship between independent and dependent variables in the models chosen to fit the data. The force data in the current study are not normally distributed and not independent measurements in time. Further, in both the linear viscoelastic and QLV models the relationship between force and time is not linear. Therefore it is not clear that hypothesis testing using the F-test is suitable or meaningful to determine the most appropriate model. In this case, visual inspection of the model fit to the data may provide a better indicator of goodness of fit.

VII. ACKNOWLEDGEMENT

This work was performed at the University of Virginia, and in collaboration with the University of Washington. Funded in part by the Defense Medical Research and Development Program (DMRDP), award No. DM090796.

VIII. REFERENCES

[1] Faul M, Xu L, Wald MM, Coronado VG, "Traumatic brain injury in the United States: emergency department visits, hospitalizations, and deaths, Atlanta (GA): Centers for Disease Control and Prevention, National Center for Injury Prevention and Control, 2010", Internet: [http://www.cdc.gov/traumaticbraininjury/tbi_ed.html], January 7, 2013, [February 21, 2013]

[2] Owens BD, Kragh JF Jr, Wenke JC, Macaitis J, Wade CE, Holcomb JB, Combat wounds in Operation Iraqi Freedom and Operation Enduring Freedom, *Journal of Trauma-Injury Infection & Critical Care*, 64(2):295-299, 2008.

[3] Pascrell B Jr, Congressman, Introduction to the report of the international conference on behavioral health and traumatic brain injury, *The Clinical Neuropsychologist*, 23(8):1281-1290, 2009.

[4] Farkas O, Povlishock JT, Cellular and subcellular change evoked by diffuse traumatic brain injury: a complex web of change extending far beyond focal damage, *Progress in Brain Research* 161:43-58, 2007.
[5] McAllister TW, Neurobiological consequences of traumatic brain injury*, Dialogues in Clinical Neuroscience*, 13(3):287-300, 2011.
[6] Povlishock JT, Katz DI, Update of neuropathology and neurological recovery after traumatic brain injury, *The Journal of Head Trauma Rehabilitation* 20(1):76-94, 2005.
[7] Holbourn AHS, Mechanics of head injury, *The Lancet*, 2, 6267, 438-441, 1943.
[8] Galford JE, McElhaney JH, A viscoelastic study of scalp, brain, and dura, *Journal of Biomechanics*, 3(2):211-221, 1970.
[9] Darvish K, Crandall JR, Nonlinear viscoelastic effects in oscillatory shear deformation of brain tissue, *Medical Engineering & Physics*, 23:633-645, 2001.
[10] Takhounts EG, Crandall JR, Darvish KK, On the importance of nonlinearity of brain tissue under large deformations, *Stapp Car Crash Journal*, 47:79-92, 2003.
[11] Gefen A et al., Age-dependent changes in the material properties of the brain and braincase of the rat, *Journal of Neurotrauma*, 20(11):1163-1177, 2003.
[12] Prange MT, Margulies SS, Regional, directional, and age-dependent properties of the brain undergoing large deformation, *Journal of Biomechanical Engineering*, 124:244-252, 2002.
[13] Finan JD, Pearson EM, Morrison III B, Viscoelastic properties of the rat brain in the horizontal plane, *Proceedings of IRCOBI Conference*, Dublin, Ireland, pp. 474-485, 2012.
[14] Thibault KL, Margulies SS, Age-dependent material properties of the porcine cerebrum: effect on pediatric inertial head injury criteria, *Journal of Biomechanics* 31(12):1119-1126, 1998.
[15] McElhaney JH, Roberts VL, Hilyard JF, Handbook of Human Tolerance, Japan Automobile Research Institute, Incorporated (JARI), p. 143, 1976.
[16] Arbogast KB et al., A high-frequency shear device for testing soft biological tissues, *Journal of Biomechanics,* 30(7):757-759, 1997.
[17] Dobbing J, The later development of the brain and its vulnerability. In: Davis J A, Dobbing J (Eds.), Scientific Foundations of Paediatrics, *Heinemann Medical*, London, UK, 1974.
[18] Mao H, Jin X, Zhang L, Yang KH, Igarashi T, Noble-Haeusslein LJ, et al., Finite element analysis of controlled cortical impact-induced cell loss, *Journal of Neurotrauma*, 27(5):877-88, 2010.
[19] Elkin BS, Morrison B III, Region-specific tolerance criteria for the living brain, *Stapp Car Crash Journal,* 51: 127-138, 2007.
[20] Cater HL, Sundstrom LE, and Morrison B, Temporal development of hippocampal cell death is dependent on tissue strain but not strain rate, *Journal of Biomechanics* 39(15):2810-2818, 2006.
[21] Morrison III B, Cater HL, Wang CC, Thomas FC, Hung CT, Ateshian GA, et al., A tissue level tolerance criterion for living brain developed with an in vitro model of traumatic mechanical loading, *Stapp Car Crash Journal*, 47:93-105, 2003.
[22] Bain AC, Meaney DF, Tissue-level thresholds for axonal damage in an experimental model of central nervous system white matter injury, *Journal of Biomechanical Engineering,* 122:615-622, 2000.
[23] Shafieian M, Darvish KK, and Stone JR, Changes to the viscoelastic properties of brain tissue after traumatic axonal injury, *Journal of Biomechanics,* 42(13):2136-2142, 2009.
[24] Saxena T, et al., Mechanical characterization of the injured spinal cord after lateral spinal hemisection injury in the rat, *Journal of Neurotrauma*, 29(9):1747-1757, 2012.
[25] Paxinos G, Watson C, The Rat Brain in Stereotaxic Coordinates 5th Edition, Bregma -5.04 mm, *Elsevier*, Oxford, UK, 2005.
[26] Hrapko M et al., The mechanical behavior of the brain tissue: Large strain response and constitutive modeling, Biorheology, 43:623-636, 2006.
[27] Fung YC, Biomechanics: Mechanical Properties of Living Tissues, 277-280, *Springer*, New York, NY, 1993.
[28] Sneddon IN, The relation between load and penetration in the axisymmetric Boussinesq problem for a punch of arbitrary profile, *International Journal of Engineering Science* 3(1):47-57, 1965.
[29] Hayes WC, Keer LM, Herrmann G, and Mockros LF, A mathematical analysis for indentation tests of articular cartilage, *Journal of Biomechanics*, 5(5):541-551, 1972.

[30]Motulsky HJ, Cristopoulos A, Fitting Models to Biological Data using Linear and Nonlinear Regression. A Practical Guide to Curve Fitting. 2003, GraphPad Software Inc., San Diego CA, www.graphpad.com.
[31]Shuck LZ, and Advani SH, Rheological response of human brain tissue in shear, *Journal of Basic Engineering*, 94 (D), 905-911, 1972.
[32]Estes MS and McElhaney JH, Response of the brain tissue of compressive loading. ASME, No 70-BHF-13, 1970.
[33]Gefen A, Margulies SS, Are in vivo and in situ brain tissues mechanically similar? *Journal of Biomechanics*, 37:1339-1352, 2004.
[34]Elkin BS, Ilankovan A, and Morrison III B, A detailed viscoelastic characterization of the rat brain*, Journal of Neurotrauma* 28:2235-2244, 2011.
[35]Lighthall JW, Controlled cortical impact: a new experimental brain injury model, *Journal of Neurotruama*, 5(1):1-15, 1988.
[36]Marmarou A et al., A new model of diffuse brain injury in rats, *Journal of Neurosurgery* 80:291-300, 1994.
[37]Arbogast K, Margulies S, Material characterization of the brainstem from oscillatory shear tests, *Journal of Biomechanics* 31(9):801–807, 1998.
[38]Mertz HJ, Anthropomorphic test devices, In: Nahum, A.M., Melvin, J.W. (Eds.), Accidental Injuries. *Springer,* New York, pp. 72–88, 2002.
[39]Hardy WN et al., A study of the response of the human cadaver head to impact, *Stapp Car Crash Journal* 51:17, 2007.
[40]Bückle H, Progress in micro-indentation hardness testing, *Metallurgical Reviews*, 4(1):49-100, 1959.
[41]Wang M et al., Nanoindentation of polymeric thin films with an interfacial force microscope, *Journal of the Mechanics and Physics of Solids*, 52:2329-2354, 2004.

IX. APPENDIX

Table 1: Absolute Structural and Material Coefficients of $F^e(h)$, $G(t)$, and $\mu(h)$ and Normalized Ratios for Region and Injury Treatment.

Absolute		A		B		C	
Unit	Coef.	Sham	Severe Injury	Sham	Severe Injury	Sham	Severe Injury
mN/mm	F_1	140.8 ± 19.2	128.2 ± 33.0	141.1 ± 24.1	155.2 ± 44.7	143.4 ± 30.7	179.0 ± 38.7
mN/mm³	F_3	111.6 ± 24.1	96.6 ± 19.7	97.3 ± 17.4	115.6 ± 22.3	110.8 ± 23.6	138.1 ± 16.4
kPa	μ_o	8.66 ± 1.23	7.89 ± 2.04	8.68 ± 1.51	9.55 ± 2.76	8.85 ± 2.00	11.02 ± 2.40
kPa/mm²	μ_2	6.88 ± 1.57	5.95 ± 1.23	5.99 ± 1.12	7.11 ± 1.38	6.83 ± 1.53	8.50 ± 1.03
-	G_1	0.739 ± 0.021	0.763 ± 0.010	0.749 ± 0.021	0.752 ± 0.015	0.746 ± 0.018	0.750 ± 0.010
-	G_2	0.122 ± 0.007	0.117 ± 0.007	0.121 ± 0.006	0.123 ± 0.004	0.122 ± 0.006	0.126 ± 0.004
-	G_3	0.057 ± 0.005	0.053 ± 0.004	0.055 ± 0.002	0.053 ± 0.006	0.057 ± 0.003	0.054 ± 0.003
-	G_4	0.029 ± 0.005	0.026 ± 0.002	0.029 ± 0.008	0.028 ± 0.003	0.027 ± 0.005	0.027 ± 0.002
-	G_5	0.023 ± 0.007	0.020 ± 0.005	0.023 ± 0.008	0.022 ± 0.006	0.023 ± 0.004	0.021 ± 0.002
-	G_∞	0.029 ± 0.009	0.022 ± 0.005	0.024 ± 0.003	0.022 ± 0.003	0.025 ± 0.004	0.023 ± 0.004

Absolute		D		E	
Unit	Coef.	Sham	Severe Injury	Sham	Severe Injury
mN/mm	F_1	145.7 ± 18.4	163.6 ± 54.1	170.8 ± 24.0	170.7 ± 21.8
mN/mm³	F_3	116.2 ± 33.5	106.0 ± 20.6	120.2 ± 32.3	142.8 ± 24.5
kPa	μ_o	8.96 ± 1.15	10.07 ± 3.35	10.49 ± 1.42	10.51 ± 1.39
kPa/mm²	μ_2	7.17 ± 2.15	6.52 ± 1.28	7.42 ± 2.07	8.79 ± 1.54
-	G_1	0.746 ± 0.015	0.750 ± 0.009	0.737 ± 0.024	0.756 ± 0.015
-	G_2	0.122 ± 0.006	0.125 ± 0.003	0.122 ± 0.007	0.118 ± 0.004
-	G_3	0.055 ± 0.004	0.054 ± 0.003	0.059 ± 0.004	0.056 ± 0.004
-	G_4	0.028 ± 0.004	0.026 ± 0.002	0.029 ± 0.005	0.024 ± 0.004
-	G_5	0.024 ± 0.007	0.020 ± 0.004	0.025 ± 0.010	0.023 ± 0.005
-	G_∞	0.025 ± 0.005	0.025 ± 0.006	0.028 ± 0.006	0.024 ± 0.002

Normalized Ratios		A			C		
Unit	Coef.	Sham		Severe Injury	Sham		Severe Injury
-	F_1	1.017 ± 0.144		0.843 ± 0.145	0.999 ± 0.228		1.187 ± 0.357
-	F_3	1.149 ± 0.182	*	0.848 ± 0.144	0.992 ± 0.158	†	1.361 ± 0.275
-	μ_o	1.017 ± 0.144		0.843 ± 0.145	0.999 ± 0.228		1.188 ± 0.357
-	μ_2	1.149 ± 0.182	**	0.848 ± 0.144	0.992 ± 0.158	††	1.362 ± 0.276

All symbols indicate a statistically significant result. Asterisks (*,**) and daggers (†,††) are comparisons between injury treatment at a particular region. (p = resulting p-value from a student's t-test and α = 0.025 is the Bonferroni corrected significance level). (*p = 0.0084, **p = 0.0085, †p = 0.0156, ††p = 0.0156. All uncertainties are ±95%CI.

Evidence of Changes in Brain Tissue Stiffness After Ischemic Stroke Derived From Ultrasound-Based Elastography

Zinnia S. Xu, BS, Rona J. Lee, BS, Stephanie S. Chu, BS, Anning Yao, BS, Marla K. Paun, BS, Sean P. Murphy, PhD, Pierre D. Mourad, PhD

Objectives—Ischemia, edema, elevated intracranial pressure, and reduced blood flow can occur in the brain as a result of ischemic stroke, including contralateral to the stroke via a process known as diaschisis. In this study, ultrasound elastography, an imaging process sensitive to the stiffness of tissue, including its relative fluid content, was used to study changes in the stiffness of individual cerebral hemispheres after transient ischemic injury.

Methods—Elastographic images of mouse brains were collected 24 and 72 hours after middle cerebral artery occlusion. The shear moduli of both ipsilateral and contralateral brain hemispheres for these mice were measured and compared to corresponding values of control animals.

Results—At 24 hours (but not 72 hours) after induction of ischemic stroke, there was a significant decrease in the shear modulus in the ipsilateral hemisphere ($P < .01$) and a significant increase in the shear modulus in the contralateral hemisphere compared to that of control animals ($P < .01$). Significant differences were also evident between ipsilateral and contralateral shear modulus values at 24 and 72 hours after infarction ($P < .01$ for both).

Conclusions—The differences between intrahemispheric averages of shear moduli of the brains of animals with stroke at 24 and 72 hours after stroke induction likely reflect the initial formation of edema and reduction of cerebral blood flow known to develop ipsilateral to ischemic infarction, the known transient increase in intracranial pressure, as well as the known initial reduction of blood flow and subsequent development of edema in the contralateral hemisphere (diaschisis). Thus, elastography offers a possible method to detect subtle changes in brain after ischemic stroke.

Key Words—cerebral stroke; diaschisis; elastography; middle cerebral artery occlusion; ultrasound

Received April 10, 2012, from the Departments of Bioengineering (Z.S.X., S.S.C., A.Y., P.D.M.) and Neurological Surgery (R.J.L., S.P.M., P.D.M.) and Applied Physics Laboratory (M.K.P., P.D.M.), University of Washington, Seattle, Washington USA. Revision requested June 16, 2012. Revised manuscript accepted for publication August 3, 2012.

This work was funded by the Congressionally Directed Medical Research Program.

Address correspondence to Pierre D. Mourad, PhD, Department of Neurological Surgery, University of Washington, Box 356470, Seattle WA 98195-6470 USA.

E-mail: pierre@apl.washington.edu

Abbreviations

MRI, magnetic resonance imaging; TTC, 2,3,5-triphenyltetrazolium chloride

Reduction of cerebral blood flow after stroke produces ischemia and edema in the ipsilateral hemisphere of the brain and globally elevated intracranial pressure as well as induces subtle effects in the contralateral hemisphere, the latter known as diaschisis.[1] Physiologic phenomena associated with diaschisis include a substantial decrease in regional cerebral blood flow of the contralateral hemisphere after middle cerebral artery occlusion, as shown in cats.[2] Furthermore, in addition to characterization of the progression of edema on the ipsilateral hemisphere,[3] others have observed edema in the contralateral hemisphere after ischemic injury on magnetic resonance imaging (MRI) as early as 9 hours after occlusion.[4]

Elastography has been used for many years to detect tissue stiffness and is growing in importance for breast cancer diagnoses.[5] One elastographic method evaluates tissue stiffness by analyzing the rate of propagation of mechanical shear waves generated within tissue through a variety of means, using various ways of monitoring the propagation of those shear waves, such as MRI[6] and sonography.[7]

Ultrasonic shear wave elastography measures local tissue stiffness by assaying ultrasound-induced shear wave propagation. Specifically, the transducer uses the acoustic radiation force to push on the tissue in a focal manner, which creates a shear wave that propagates transversely from its initiation site (Figure 1, A and C). The local speed of shear wave propagation is proportional to the Young modulus with the following relationship: $E = 3\rho c^2$, where E is the Young modulus (kilopascals), a measure of the resistance of tissue to shearing; ρ is the density (kilograms per cubic meter), and c is the speed of shear waves (meters per second). This particular version of ultrasound-based elastography (known as shear wave elastography) is sensitive to the average fluid content in tissue,[7] since shear waves do not propagate through fluid.

This imaging technique was developed to highlight small, stiff, calcified breast lesions within a large, relatively homogeneous field of view. In this study, following the technique shown by Derieppe et al,[8] we used it on small heterogeneous tissue (the brains of mice after stroke), where scattering of the propagating shear waves reduced details from the image (Figure 1, B and C), to assay the temporal evolution of hemispheric averages of brain tissue stiffness after ischemic injury.

Materials and Methods

Middle Cerebral Artery Occlusion

Male C57BL/6 mice (25–30 g) were used for the 45-minute middle cerebral artery occlusion. Anesthesia was induced by inhalation of 3% isoflurane and maintained with 1.5% to 2% isoflurane. Body temperature was monitored throughout the surgery with a rectal probe and maintained at 36°C to 38°C with a heating blanket. A midline incision was made on the ventral surface of the neck. The right common carotid artery was isolated and ligated, after which a 12-mm-long, 6-0 nylon filament was introduced and advanced up through the internal carotid artery and into the middle cerebral artery. Mice were kept under anesthesia for the entire duration of the 45-minute occlusion. After the occlusion, the filament was pulled back and removed from the artery to allow for reperfusion. Cerebral blood flow in the area was monitored during the occlusion and reperfusion with a laser Doppler device (MoorLab laser Doppler perfusion monitor; Moor Instruments, Inc, Wilmington, DE). Mice were euthanized either 24 or 72 hours later by cervical dislocation.

Control animals did not undergo surgical preparation. Pilot studies by us performed over the years have shown no difference in brain structure as shown by MRI and histopathologic examination between control animals that received the sham surgery and control animals that received no surgical procedure. Therefore, at the urging of our local Institutional Animal Care and Use Committee, we chose to use controls without surgery for this imaging study. There were a total of 13 control mice and 16 mice that underwent the middle cerebral artery occlusion procedure: 8 euthanized after 24 hours and 8 after 72 hours. All procedures were approved by the University of Washington Institutional Animal Care and Use Committee.

Ultrasound Image Acquisition

Anesthesia was induced in the animals by inhalation of 3% isoflurane and maintained at 1% to 2% isoflurane during data acquisition. Hair was removed from the head to decrease attenuation of ultrasound caused by air trapped within the hair. The skull and skin were left intact. A custom-made polyvinyl alcohol standoff[9] was used to maintain an optimal distance of approximately 30 mm between the transducer and the bottom of the mouse brain. Ultrasound gel (Polysonic multipurpose gel; Cone Instruments, Solon, OH) was applied to the mouse and the standoff. The standoff was placed over the mouse.

An Aixplorer multiwave ultrasound system (SuperSonic Imagine, Aix-en-Provence, France) with its linear SL 15–4-MHz transducer was used to measure the shear modulus of brain tissue in our animals. The transducer's imaging frequency ranged between 4.0 and 15.0 MHz, with a standard center frequency of 8.5 MHz. Two types of images were collected: shear wave elastography and B-mode. B-mode imaging assessed the 2-dimensional anatomy of the brain region from the echoes returning from tissue of different density.[10] The B-mode gain was adjusted for clear visualization of the skull. Shear wave elastography uses ultrasound-generated shear wave propagation to measure the absolute tissue elasticity displayed per pixel. In the shear wave elastographic mode, the penetration depth was approximately 30 mm.[7] Imaging was performed within a range of 0 to 180 kPa in an unblinded fashion to minimize gross imaging artifacts associated with the surrounding tissue and skull (Figure 2), since typical brain shear modulus values lie between 2.7 and 25 kPa, as reviewed below. This method therefore blinded the user to the imaging of the brain itself.[6,11]

Figure 1. Shear wave propagation within a tissue phantom. **A**, Shear wave propagation with no lesion at an early time. **B**, Shear wave propagation with scattering from a lesion on the top left side at an early time. **C**, Shear wave propagation with no lesion at a later time. **D**, Shear wave propagation with scattering from a lesion on left side at a later time. **A** and **C** show propagation without undue complexity in the shear wave, whereas **B** and **D** show the back-propagation of a portion of the shear wave due to its scattering by a lesion in the tissue phantom. Averaging of signals over time derived from shear waves propagating in multiple directions causes a given feature in the tissue to appear bigger than it is. The color scheme describes axial displacement in the direction of the transducer (top). Red represents maximum positive displacement, whereas blue represents maximum negative displacement. The color scale of each image is adjusted for the maximum and minimum displacement values for that particular image.

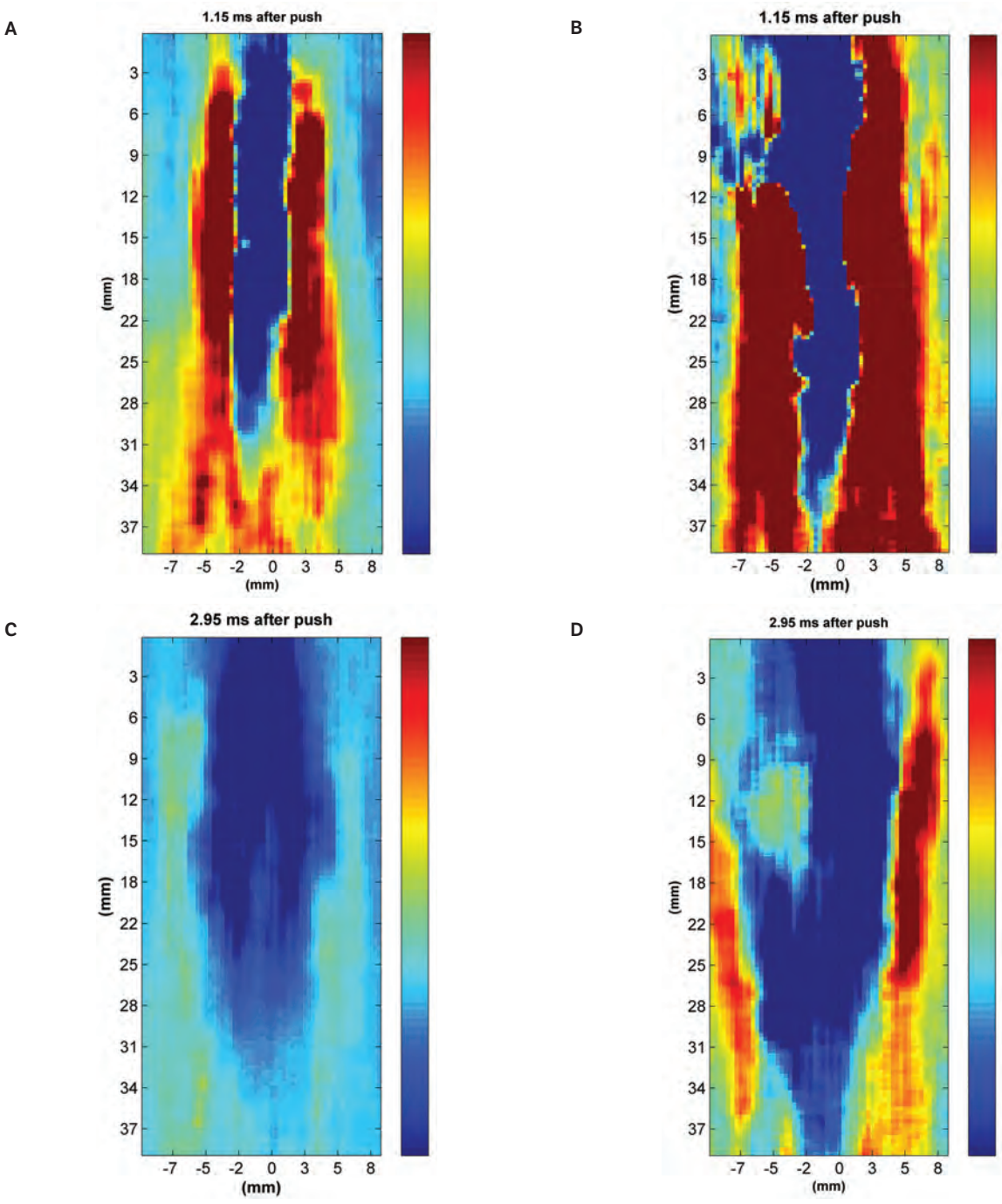

Specifically, ultrasound gel was applied to the ultrasound transducer, itself placed on the standoff. Coronal images of the mouse head including the brain were obtained. We defined the region of interest as the brain. The ultrasound was beamed into the brain inside the skull from its superior to its inferior aspect. The grayscale gain was adjusted to compensate for attenuation. The grayscale gain was set as low as possible to obtain a clear image and give priority to the quality of the shear wave image. The selected shear wave imaging region was reduced to the smallest size that still encompassed the brain to reduce the presence of artifacts from outside the mouse skull. The shear wave gain was adjusted for the same reason. The transducer was moved along the anteroposterior axis of the brain. Multiple coronal images were taken from the front, middle, and back sections of the brain. Image artifacts associated with the skull were avoided as much as possible when selecting images in the shear wave elastographic mode. Approximately 3 to 6 images were taken from each section of the brain.

2,3,5-Triphenyltetrazolium Chloride Staining

Mouse brains were removed after cervical dislocation and cut into eight 1-mm coronal sections. Slices were stained with 0.1% 2,3,5-triphenyltetrazolium chloride (TTC; Sigma-Aldrich, St Louis, MO) in phosphate-buffered saline for 40 minutes to 1 hour at room temperature in the dark (see Figure 3E). They were then fixed in 4% formalin and stored at 4°C. Nine mice that showed no infarct through TTC stain was excluded from the study.

Ultrasound Image Analysis

Ultrasound images were chosen for analysis from the same section of the brain (front, middle, or back) that showed an infarct after TTC staining. We chose 1 of the approximately 5 ultrasound images per mouse that had minimal imaging artifacts (eg, Figure 3A). Since the volume in the murine skull is small, shear waves reflect and scatter off the skull (eg, Figure 1, B and D). During the image-averaging process intrinsic to this commercial machine, the result is imaging artifacts that appear as high shear modulus areas, with their basis in the skull, that diffuse into the brain region. As in the study by Derieppe et al[8] on assaying kidney stiffness, discussed below, our postprocessing of the images sought not to highlight particular intrahemispheric features of brain but instead to simply avoid specific imaging artifacts and develop measures for average intrahemispheric brain tissue stiffness for comparison with control-derived stiffness images.

All postprocessing of the images was done with MATLAB (The MathWorks, Natick, MA). In postprocessing, the entire brain region within the skull was manually selected by a freehand technique using MATLAB software applied to the shear wave elastographic image obtained from the Aixplorer system (Figure 3B). Because the shear wave elastographic image shows the elastographic image on top of the B-mode image, the operator can directly select the portion of the brain within the cranium based on the structure of the skull seen in B-mode. After the selection,

Figure 2. A, Shear wave elastographic image from a mouse with middle cerebral artery occlusion showing a substantial image artifact (hot colors) diffusing intracranially. **B**, The skull can be distinguished in the B-mode image.

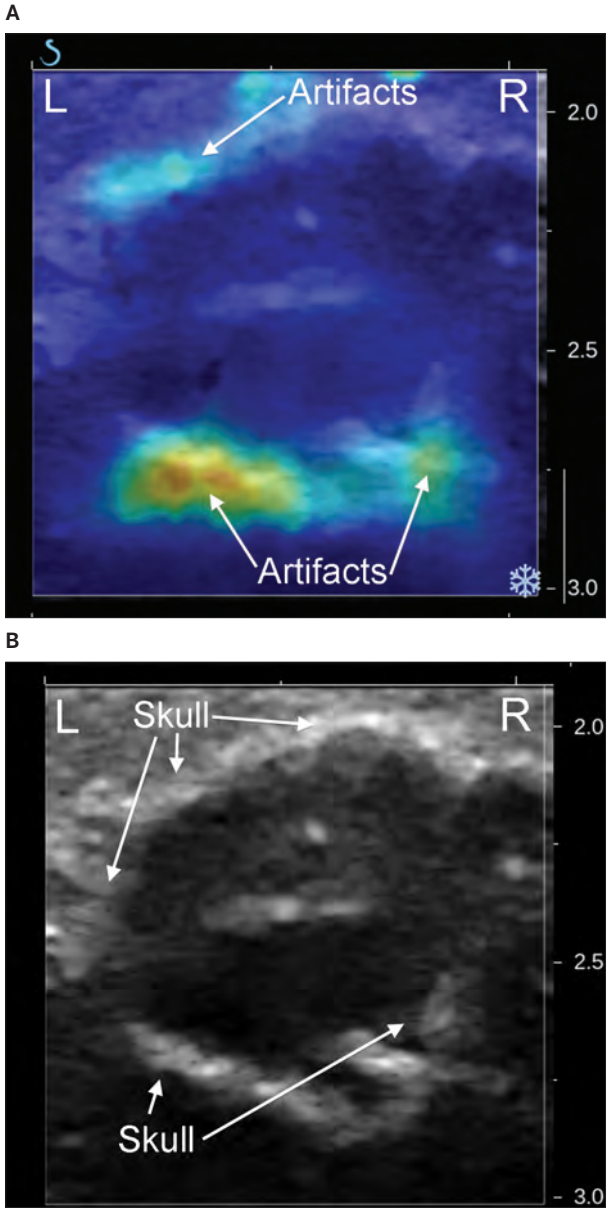

the elastographic image of the selected brain region was compressed to an elasticity range of 0 to 35 kPa (from 0–180 kPa) for increased visualization and contrast within the brain, which tends to have a lower shear modulus than the skull (Figure 3C). The ipsilateral and contralateral hemispheres of the brain were then manually selected directly from the elastographic image of the brain (Figure 3D). These regions were selected with care to avoid skull and imaging artifacts from the skull. These image artifacts are defined as areas with a high shear modulus (greater than that of the brain and tied anatomically to the skull) that extend from outside the brain into the brain region (Figure 3D). The shear moduli of the two hemispheric selections were then averaged to obtain a mean shear modulus for each mouse brain.

This feature extraction analysis was performed 3 times for each image in a blinded fashion to ensure that there was no operator bias. As an example of the robustness of this procedure, Figure 4 shows 3 region of interest analyses derived in a blinded fashion from the same raw shear wave elastographic image. The images were coded so that the operator did not know whether the image was from control, 24-hour stroke, or 72-hour stroke mice.

Finally, all selections were reviewed a posteriori, and shear wave elastographic selections (Figure 3D) were compared to TTC histologic specimens (Figure 3E) to ensure that all region of interest selections from the shear wave elastographic images included areas of damage according to TTC staining.

2,3,5-Triphenyltetrazolium Chloride Image Analysis

The TTC-stained brain slices were optically scanned. The operator who performed the TTC image analysis was blinded to whether the mouse had a stroke for 24 or 72 hours. By the same freehand technique described above, the entire portion of the image that contained brain was selected. The core infarct area was then selected. This area is distinguished by tissue that did not pick up the stain (white). The penumbra, surrounding the core, also includes damaged tissue but is less obviously distinguishable with the TTC stain. The number of pixels in the core infarct area was divided by the number of pixels within the entire brain. With this information, the percentage of the brain that contained a core infarct was calculated. The selection of the infarct area was done 3 times for every image, and the percentage of the brain with an infarct was averaged over the 3 images.

Data Analysis

Mean shear modulus values were normalized for each individual mouse. The mean shear modulus (G) of each hemisphere was divided by the average of the two hemispheres for each mouse:

$$G_{\mathrm{N\,ipsi}} = \frac{G_{\mathrm{ipsi}}}{\frac{G_{\mathrm{ipsi}} + G_{\mathrm{contra}}}{2}}$$

$$G_{\mathrm{N\,contra}} = \frac{G_{\mathrm{contra}}}{\frac{G_{\mathrm{ipsi}} + G_{\mathrm{contra}}}{2}} \quad .$$

The normalized shear modulus (G_{N}) reports the value of the shear modulus of each hemisphere for each given mouse relative to the average value across the entire brain. Note that a normalized value of 1 means that contralateral and ipsilateral hemispheres have the same average shear modulus.

The Student *t* test was used to compare the average shear modulus for each hemisphere (ipsilateral and contralateral) for 3 populations: control, 24-hour, and 72-hour mice. The *t* test values were calculated between respective hemispheres (contralateral or ipsilateral) among the 3 populations to see whether the mean shear modulus differed significantly between populations. The Student *t* test was also performed on the data for ipsilateral and contralateral hemispheres for each population to identify interhemispheric differences. Box plots showing the spread of normalized mean shear modulus values from control, 24-hour, and 72-hour mice were prepared for each hemisphere in SigmaPlot (Systat Software, Inc, San Jose, CA).

Results

Percentage of Stroke-Damaged Tissue

The area of infarct for 72-hour animals (mean, 15.2%) did not vary in a statistically significant fashion from the area of infarct for the 24-hour animals (mean, 10.9%; $P = .20$).

Normalized Shear Modulus of Hemispheres

Average normalized stiffness values for ipsilateral and contralateral brain hemispheres were measured, and the results are summarized in Figures 5 and 6 and Table 1. Figure 5A and Table 1 show that 24-hour animals had a significantly decreased ipsilateral shear modulus compared to control animals ($P < .01$). There was no difference between ipsilateral 72-hour stroke and control animal shear modulus values ($P = .09$). In addition, there was no difference between ipsilateral 72- and 24-hour stroke animal shear modulus values ($P = .13$).

The contralateral hemisphere of 24-hour stroke animals showed a significant increase in elasticity when compared to

Figure 3. Stroke image processing in a mouse with 72-hour middle cerebral artery occlusion. **A**, Aixplorer images in the shear wave elastographic mode (top) and B-mode (bottom). **B**, The brain was selected from the elastographic image (0–180 kPa) displayed on top of the corresponding B-mode image. There is a visible area with a lower shear modulus value in the right hemisphere (dark blue). **C**, The elastographic image of the entire brain was scaled to 0 to 35 kPa to enhance the contrast. Regions of high stiffness indicate image artifacts. **D**, The hemispheric regions to be analyzed were selected manually by the operator to avoid the skull and artifacts (hot color regions associated with large shear modulus values). **E**, Corresponding TTC histologic specimen from the same mouse showing damage in the right hemisphere, distinguished by the white region. This damage correlates with the location of the low shear modulus seen in the elastographic images.

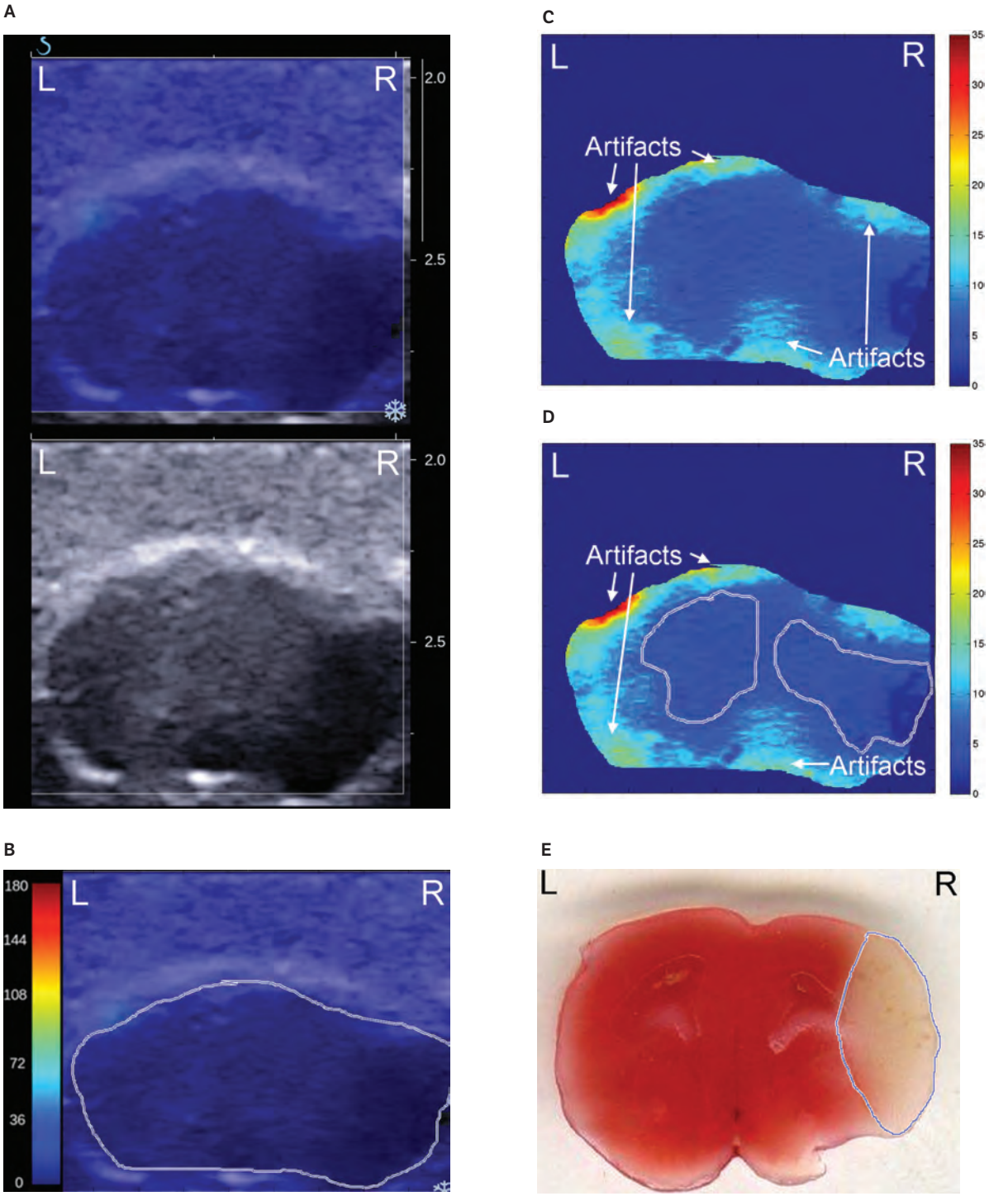

the control population ($P < .01$; Figure 5B). At 72 hours, stroke and control populations exhibited no difference ($P = .09$), nor was there a difference between contralateral hemisphere elasticity values at 24 versus 72 hours after stroke ($P = .13$).

Figure 6 shows that there was a difference between ipsilateral and contralateral shear modulus values both 24 and 72 hours after stroke ($P < .01$). There was also a weak difference in the interhemispheric shear modulus for the control animals ($P = .04$).

Discussion

Our observations included a weak but statistically significant difference ($P = .04$) between the stiffness measures of the 2 hemispheres of the control brain. This observed difference was more significant for the interhemispheric stiffness of brains in mice at both 24 and 72 hours after stroke ($P < .01$). We have therefore chosen to make our assertions of statistical significance at the more stringent *P* value of .01. This relatively weak difference for control animals could have arisen because of asymmetries in delivery of the focused ultrasonic pulse generated by our system or could reflect a real but weak interhemispheric difference in blood content between each hemisphere, due to the asymmetric input of blood from the heart into the brain.

Comparison to Other Measures of Brain Tissue Stiffness

Previous work describing magnetic resonance elastography has shown shear modulus measurements similar to what we found.[6,11] Kruse et al[6] reported the stiffness of white matter as 13.6 kPa and that of gray matter as 5.22 kPa in a study of 25 healthy people, whereas Green et al[11] reported findings that white matter measured 3.1 kPa and gray matter measured 2.7 kPa in a study of 5 healthy men. Moreover, recent work by Mace et al[12] using a research version of the clinical ultrasound machine we used reported shear modulus values from rat brain ranging between 2 and 25 kPa, with an average of 12 kPa.

Although our studies did not distinguish between white and gray matter of the brain, our elastographic measurements of tissue stiffness (4.32 kPa, control ipsilateral; and 4.49 kPa, control contralateral) are within the values noted for magnetic resonance elastography and research sonoelastographic machines.

Changes in the Ipsilateral Hemisphere

In animals 24 hours after stroke, the shear moduli of the ipsilateral hemispheres were significantly less than those of control animals. This finding was likely due to ischemia caused directly by the occlusion as well as the rapid development of edema.[4] According to Gotoh et al,[3] edema in the ipsilateral hemisphere can start developing a few hours after middle cerebral artery occlusion, increasing until it reaches a maximum at around 2 to 3 days. Edema slows the propagation of shear waves, thereby directly affecting the shear modulus of the tissue.[7] Magnetic resonance elastography of the brain has also shown that edema leads to a decrease in elasticity.[13] Ischemic brain edema results initially from cell swelling (cytotoxic edema) caused by depleted

Figure 4. A–C, Representative selections of average hemispheric shear moduli chosen for blinded analysis.

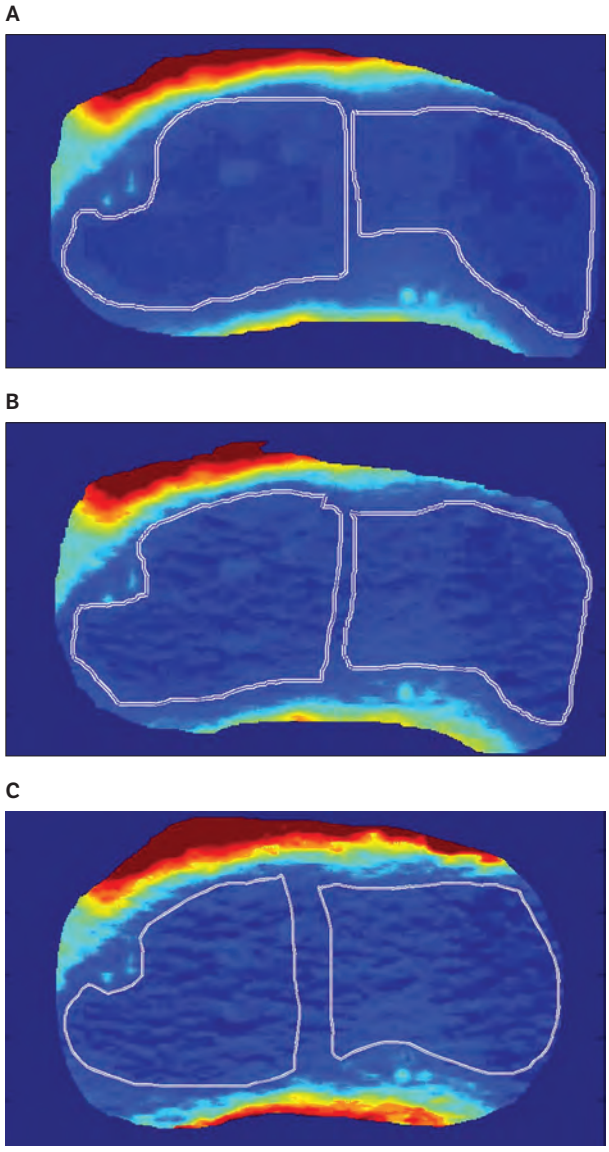

energy substrates in brain cells by ischemia. Eventually, vasogenic edema also develops, caused by increased blood vessel permeability.[14] Vasogenic edema causes the fluidity of the tissue to increase with a decrease in elasticity.[15] The decrease in ipsilateral elasticity reported here is also consistent with the work of Rousseaux and Steinling,[16] who found mean cerebral blood flow values in stroke patients to be generally lower than those of control participants in the ipsilateral hemisphere. Finally, this observation is also consistent with very recently published work on the elasticity of rat brains after stroke.[17]

In animals 72 hours after stroke, the mean ipsilateral shear moduli were not significantly different from those of control animals. One possible explanation is that brain edema ipsilateral to stroke reaches a maximum 2 to 3 days after ischemic injury and then began to decrease.[3] Another explanation is the evolution of intracranial pressure after stroke discussed by Jiang et al 2011,[18] who, in a rat model of middle cerebral artery occlusion stroke, found that intracranial pressure increased throughout the times they measured (up to 24 hours after the procedure). Perhaps an increase in intracranial pressure, caused by the buildup of edema in the brain, eventually worked to stiffen the tissue. Therefore, the average stiffness of the ipsilateral brain at 72 hours may have decreased back to baseline because of a combination of reduced edema relative to 24 hours, continued ischemia, and increasing intracranial pressure.

Changes in the Contralateral Hemisphere

We hypothesize that the observed increase in contralateral hemispheric tissue elasticity for the 24-hour animals arose because of a reduction in contralateral cerebral blood flow[1,16] in combination with elevated intracranial pressure created by the large volume of edema formed in the ipsilateral hemisphere. Although Warner et al[19] and Kim et al[20] showed that elasticity decreases with decreased perfusion, these experiments were done in the liver and kidney, where the internal pressure applied by the blood within the freely suspended organs provides a meaningful source of tissue stiffness, quite like air blown into a balloon. In contrast, the brain is enclosed within a hard skull, nearly filling it. After stroke, observations show not only a reduction in fluid content within the brain contralateral to stroke but also increased intracranial pressure within the entire cranium. Increased intracranial pressure (measuring high at least 24 hours after middle cerebral artery occlusion induction[18]) will put pressure on contralateral (as well as ipsilateral) brain tissue. Therefore, brain tissue may increase in stiffness contralateral to stroke due to both the intracranial pressure increase and the reduction in fluid content within the contralateral hemisphere, instead of sagging like liver or kidney. At 72 hours, the elasticity values for the contralateral cerebral hemisphere of stroke animals are no different than those of control animals. Observations by Gotoh et al[3] show that edema develops in the contralateral hemisphere after infarction and reaches a peak within 2 to 3 days of infarction. We hypothesize that development of edema may decrease the overall tissue elasticity due to increasing fluid content, accounting perhaps for the difference seen between contralateral tissue stiffness in 24- and 72-hour animals.[18]

Figure 5. A, Normalized ipsilateral shear modulus values for control, 24-hour, and 72-hour mice. **B**, Normalized contralateral shear modulus values for control, 24-hour. and 72-hour mice. *$P < .01$.

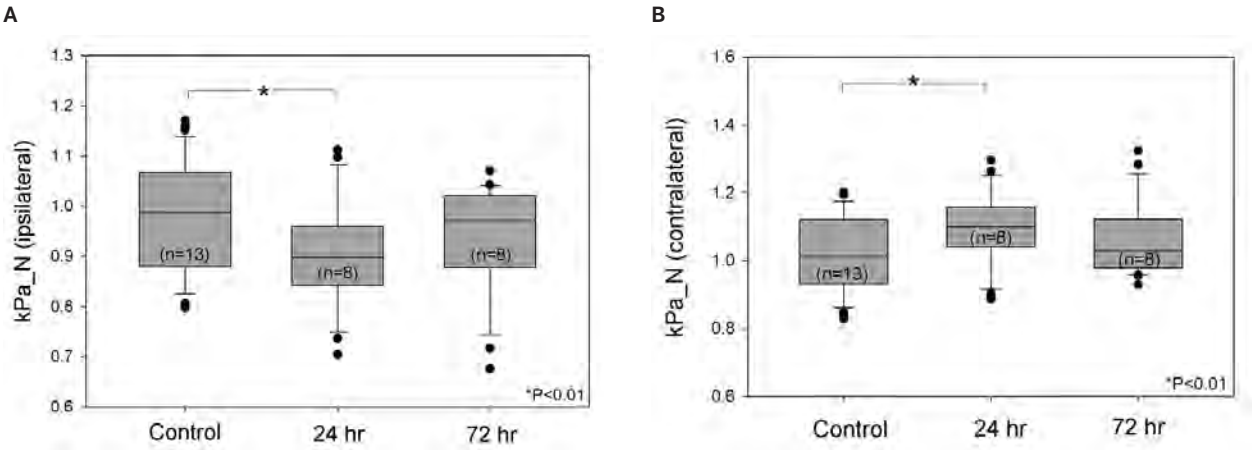

Table 1. Non-Normalized and Normalized Shear Modulus Values for Control, 24-Hour, and 72-Hour Populations

Parameter	Control	24 h	72 h
Ipsilateral non-normalized, kPa	4.32 ± 1.44	3.85 ± 0.96	3.66 ± 1.02
Contralateral non-normalized, kPa	4.49 ± 1.32	4.86 ± 1.79	4.23 ± 1.49
Ipsilateral normalized	0.98 ± 0.11	0.90 ± 0.10	0.94 ± 0.10
Contralateral normalized	1.02 ± 0.11	1.10 ± 0.10	1.06 ± 0.10

Values are mean ± SD.

Limitations

The work as presented takes advantage of the averaging performed within the ultrasound machine to develop estimates of the intrahemispheric average of brain tissue stiffness. This process is at the cost, however, of the requirement that we minimize the influence on our analysis of the imaging artifacts that arise through the imaging procedure itself. To reduce the influence of these features in the images on our quantitative results, we performed individual analyses of each shear wave image in triplicate, in a blinded fashion, to highlight portions of the brain likely independent of those artifacts that also overlap with damage assessed separately, via histologic examination. We have also made careful comparisons with the same shear wave image analysis on control tissue. Performing more detailed analysis requires access to the shear wave propagation data themselves (again, Figure 1), so that we can analyze down to the millimeter scale the propagation of a given shear wave within a given hemisphere of brain. Mace et al[12] have successfully performed this detailed analysis in large and normal rat brains through a large cranial window, using a research version of the commercial device we had for our use. We have begun this kind of analysis and anticipate reporting on it in future work.

Our analysis allow us to hypothesize that a variety of physiologic processes associated with stroke (edema formation, intracranial pressure variations, and alterations of cerebral blood flow) explain the changes in the mechanical properties of brain tissue we observed using intrahemispheric averages of the ultrasound-derived brain tissue shear modulus. Clearly, future studies are required to test these hypotheses. Specifically required are measurements of intracranial pressure and the extent and time course of edema in both hemispheres of the brain along with cerebral blood flow simultaneous with direct imaging of intrahemispheric structures within the brain to verify and further analyze the features of the brain we inferred after stroke.

Figure 6. Comparison of normalized mean shear modulus values of ipsilateral and contralateral hemispheres for control, 24-hour, and 72-hour populations. *$P < .01$; **$P = .04$.

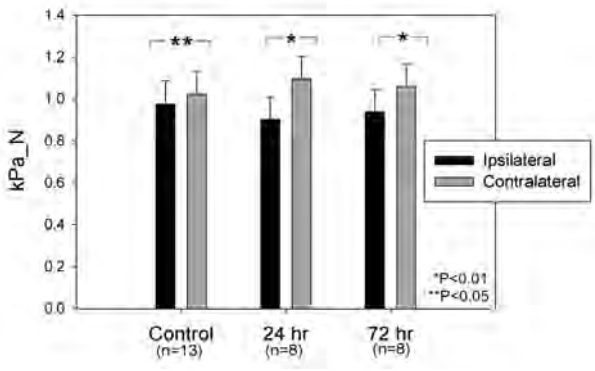

Future Work

Changes in the distribution of fluids within the brain (blood and edema) as well as intracranial pressure have been observed after stroke, based on MRI and positron emission tomography as well as direct analysis of tissue in both the ipsilateral and contralateral hemispheres.[1,3,4,14,16] Using ultrasound-based elastography, we have observed changes in brain stiffness consistent with those physiologic observations, including diaschisis. Successful testing of these hypotheses should motivate future imaging work in humans after stroke and the possible application of this imaging modality in the clinic. For example, the portable and economical aspects of the technology we have used may prove to have an impact on the management and detection of stroke in areas where computed tomography and MRI are not readily available or appropriate.

References

1. Andrews RJ. Transhemispheric diaschisis: a review and comment. *Stroke* 1991; 22:943–949.
2. Han DH, Jung HW, Lee SH, Kim HJ, Choi KS, Sim BS. Acute cerebral infarction and changes of regional cerebral blow flow (rCBF) following

experimental middle cerebral artery (MCA) occlusion. *Neurol Res* 1988; 10:203–212.

3. Gotoh O, Asano T, Koide T, Takakura K. Ischemic brain edema following occlusion of the middle cerebral artery in the rat, I: the time courses of the brain water, sodium and potassium contents and blood-brain barrier permeability to ^{125}I-albumin. *Stroke* 1985; 16:101–109.
4. Izumi Y, Haida M, Hata T, Isozumi K, Kurita D, Shinohara Y. Distribution of brain oedema in the contralateral hemisphere after cerebral infarction: repeated MRI measurement in the rat. *J Clin Neurosci* 2002; 9:289–293.
5. Garra BS. Elastography: current status, future prospects, and making it work for you. *Ultrasound Q* 2011; 27:177–186.
6. Kruse SA, Rose GH, Glaser KJ, et al. Magnetic resonance elastography of the brain. *Neuroimage* 2008; 39:231–237.
7. Tanter M, Bercoff J, Athanasiou A, et al. Quantitative assessment of breast lesion viscoelasticity: initial clinical results using supersonic shear imaging. *Ultrasound Med Biol* 2008; 34:1373–1386.
8. Derieppe M, Delmas Y, Gennisson JL, et al. Detection of intrarenal microstructural changes with supersonic shear wave elastography in rats. *Eur Radiol* 2012; 22:243–250.
9. Fromageau J, Brusseau E, Vray D, Gimenez G, Delachartre P. Characterization of PVA cryogel for intravascular ultrasound elasticity imaging. *IEEE Trans Ultrason Ferroelectr Freq Control* 2003; 50:1318–1324.
10. Mourad P. Biological effects of ultrasound. In: Webster JL (ed). *Encyclopedia of Electronics and Electrical Engineering*. Vol 2. Philadelphia, PA: John Wiley & Sons; 1999:368–386.
11. Green MA, Bilston LE, Sinkus R. In vivo brain viscoelastic properties measured by magnetic resonance elastography. *NMR Biomed* 2008; 21:755–764.
12. Mace E, Cohen I, Montaldo G, Miles R, Fink M, Tanter M. In vivo mapping of brain elasticity in small animals using shear wave imaging. *IEEE Trans Med Imaging* 2011; 30:550–558.
13. Larrat B, Pernot M, Aubry JF, et al. MR-guided transcranial brain HIFU in small animal models. *Phys Med Biol* 2010; 55:365–388.
14. Rosenberg GA. Ischemic brain edema. *Prog Cardiovasc Di*s 1999; 42:209–216.
15. Kuroiwa T, Ueki M, Ichiki H, et al. Time course of tissue elasticity and fluidity in vasogenic brain edema. *Acta Neurochir Suppl* 1997; 70:87–90.
16. Rousseaux M, Steinling M. Crossed hemispheric diaschisis in unilateral cerebellar lesions. *Stroke* 1992; 23:511–514.
17. Martin A, Mace E, Boisgard R, et al. Imaging of perfusion, angiogenesis, and tissue elasticity after stroke. *J Cereb Blood Flow Metab* 2012; 32:1496–1507.
18. Jiang X, Cheng CB, Fang M, Jiang WQ, Zhu GF, Zeng HK. Effect of hydroxyethyl starch on intracranial pressure and plasma colloid osmotic pressure in rats with cerebral ischemia/reperfusion injury [in Chinese]. *Zhongguo Wei Zhong Bing Ji Jiu Yi Xue* 2011; 23:166–168.
19. Warner L, Yin M, Glaser KJ, et al. Noninvasive In vivo assessment of renal tissue elasticity during graded renal ischemia using MR elastography. *Invest Radiol* 2011; 46:509–514.
20. Kim SU, Kim JK, Park YN, Han KH. Discordance between liver biopsy and Fibroscan® in assessing liver fibrosis in chronic hepatitis B: risk factors and influence of necroinflammation. *PloS One* 2012; 7:e32233.

Detection of mild traumatic brain injury in rodent models using shear wave elastography: preliminary studies.

Zinnia S. Xu[1], Anning Yao[1], Stephanie S. Chu[1], Marla K. Paun[2], Abbi M. McClintic[3], Sean P. Murphy, Ph.D.[3], Pierre D. Mourad, Ph.D.[1,2,3].

[1]Department of Bioengineering
University of Washington
Box 356470
Seattle, WA 98195

[2]Applied Physics Laboratory
University of Washington
Box 355640
Seattle, WA 98195

[3]Department of Neurological Surgery
University of Washington
Box 356470
Seattle, WA 98195

Corresponding Author:
Pierre D. Mourad
Department of Neurological Surgery
University of Washington
Box 356470
Seattle WA 98195

(main)	206-543-3570
(fax)	206-543-6785
(office & voicemail)	206-543-9125
(email)	pierre@apl.washington.edu

Running title: Ultrasound elastography detection of TBI

Manuscript category: Original Research

Abstract

Objectives: Traumatic brain injury (TBI) can cause adverse physiological changes in fluid content within brain, which may lead to changes in tissue elasticity (e.g., stiffness). This study evaluated the ability of ultrasonic shear wave elastography (SWE) imaging to observe these changes in brain after TBI, *in vivo*.

Methods: Mice and rats received a mild TBI or sham surgery and were imaged acutely or 24 hours after injury using SWE and the hemispheric stiffness values were compared.

Results: Stiffness values were consistent across brain hemispheres of sham TBI rodents. By 24 hours after TBI, relative brain-tissue stiffness values for mice and rats each decreased ipsilaterally and increased contralaterally, both relative to each other and as compared to sham TBI rodents ($p<0.05$). The absolute value of tissue elasticity increased for rats ($p<0.05$) but not for mice.

Conclusion: Differences between intra-hemispheric stiffness values of rodent brain by 24 hours after mild TBI may reflect the observed edema and hemorrhage ipsilateral to TBI, and the known reduction of cerebral blood flow in both brain hemispheres. If these hypotheses hold true, ultrasonic shear wave elastography may offer a method to detect adverse changes in fluid content within brain after mild TBI.

Keywords: Brain; Edema; Elastography; Ultrasound; Traumatic Brain Injury;

Introduction

Incidence of traumatic brain injury (TBI) has increased significantly in recent years owing to the growing use of improvised explosive devices in operations in the Middle East [1]. TBI also occurs among civilians, primarily caused by falls, motor vehicle accidents, struck by/against events, contributing up to 30% of injury-related deaths [2].

Computed tomography (CT) and magnetic resonance imaging (MRI) are the current civilian standards for imaging traumatic brain injury, with CT more commonly available, thanks to its speed and relatively low cost. It is therefore generally used acutely, if available, while MRI finds more use a few days after initial injury because of its sensitivity to blood products [3]. Both imaging technologies are often insufficiently accessible for military TBI (Ken Curley, MD, personal communication) with the additional requirement of patient transport to the imaging site, relevant in either the civilian or military context. Transcranial ultrasound imaging offers a rapid, portable and point-of-care system for imaging brain but lacks sufficient contrast to provide much diagnostic utility [4].

Here we consider ultrasonic shear wave elastography (SWE) as a possible alternative or adjunct to CT and MRI. SWE creates images of Young's Modulus, a measure of the resistance to such that larger values describe stiffer tissue. Therefore, maps of Young's Modulus describe the spatial dependence of tissue shear elasticity or stiffness. The SWE system works by generating within tissue a rapid, net axial displacement of tissue. This spatially focal impulse force then creates a shear wave that propagates outward from the 'pushed' region [5-7]. SWE systems use diagnostic ultrasound to track the propagating shear wave, with the existing commercial system from SuperSonic Imagine (SSI) translating the square of that local speed into a local value of Young's Modulus [5].

SWE via the SSI clinical system has found well-documented use on humans for large and primarily homogenous organs such as breast [5, 8-9]. Studies exist that have used the clinical system in animal models of disease such as kidney [10] and ischemic cerebral stroke [11]. Relevant here, Xu et al [11] resolved inter-hemispheric differences in the stiffness of mouse brain after complete occlusion of the middle cerebral artery. They hypothesized that known formation of edema and ischemia due to stroke ipsilateral to the occlusion and diaschisis contralateral to the occlusion caused the observed inter-hemispheric differences in stiffness.

When using small animal models internal scatter of the shear wave can produce aliasing in stiffness images [10-12]. Indeed, Macé et al. [12] used a research version of the

SSI to remove this aliasing effect by tracking individual shear waves between scattering events. Their maps of brain-tissue stiffness displayed intra-hemispheric features in exquisite detail.

As a first step towards the goal of making SWE applicable to human brain, we used SWE images from the SSI of the brains of rats and mice that received a focal traumatic brain injury to analyze the temporal evolution of the stiffness of brain associated with that injury.

Materials and methods

All animal procedures were approved by the Institutional Animal Care and Use Committee (IACUC) of the University of Washington and the US Army Medical Research and Materiel Command (USAMRMC) Animal Care and Use Review Office (ACURO).

Animal techniques

Surgery

Fifteen male Sprague Dawley rats (250-300 grams, Charles River) and fifteen male mitoCFP mice (20-30 grams, bred at the University of Washington [13]) were used. These were divided into three experimental groups for both rats and mice: sham TBI group (n=5), acute TBI group (n=5) and 24-hour TBI group (n=5). We induced mild TBI following the controlled cortical impact (CCI) protocol of Lighthall [14] as refined by Dixon et al [15], which produced a repeatable and localizable cortical contusion.

Anesthesia was induced via inhalation isoflurane (5% isoflurane for rats; 3% for mice) and maintained (2-3% isoflurane for rats; 1-2% isoflurane for mice) during surgery and cortical impact. The surgical technique was nearly identical for rats and mice; therefore we describe the procedure generally referring to the subjects as “rodents.”

The rodent was placed in a stereotaxic device within a pneumatic controlled cortical impact device (AmScien Instruments, Richmond, VA, USA) to hold the head steady. A heating pad was used to maintain the core body temperature of approximately 37° C. The surgical site was prepared by shaving the top of the head then application of a lotion hair remover. Prior to surgery, lidocaine (1 mg/kg) was injected subcutaneously to the surgery site. For TBI rodents allowed to survive 24 hours after injury, bupivacaine (1 mg/kg) was also injected subcutaneously to the surgery site and buprenorphine (0.05 mg/kg) was delivered as an intraperitoneal injection.

After establishing an anesthetic plane via toe pinch and respiratory observation, an incision was made from the bregma to just posterior of the lambda suture line and the skull was exposed. A small (of order 1 mm) hole was drilled in the right (ipsilateral) parietal portion of the skull bone using a surgical drill (Dremel, Racine, WI). Bone rongeurs were used to enlarge the drilled hole to approximately 4 mm in diameter between the bregma and lambda of the right parietal bone of each of mice and rats. (For mice this cranial window encompassed nearly the entire cranial vault above the ipsilateral hemisphere of brain. For rats, this hole took up less than 40% of available ipsilateral cranial vault.) The cranial window was then aligned with the tip of the cortical impact device. At this point sham animals were removed from the apparatus. For TBI animals, the cortical impact device was then fired to create an impact at the surface of the brain of a velocity of 3.5 m/s and a depth of 1.0 mm for rats and 0.5 mm mice.

For sham and acute TBI rats, the ipsilateral cranial window was enlarged after impact to approximately the entire right parietal bone up to the bregma, lambda, and sagittal suture line. For mice we worked with the existing ipsilateral cranial window. For each of the sham and acute TBI rats and mice an identical cranial window was then created on the contralateral side of the skull.

For the rodents in the 24-hour TBI groups, after impact the unilateral cranial window was filled with bone wax. The surgery site was then closed with 3-0 nylon sutures (Covidien, Mansfield, MA, USA) and the rodents were returned to their cages. After 24 hours, these received bilateral craniectomies as described above.

SWE Image Acquisition

After the creation of bilateral cranial windows we imaged the brains of each rodent with a linear SL15-4 MHz transducer of an Aixplorer Multiwave Ultrasound System (SuperSonic Imagine, Aix-en-Provence, France). The transducer's imaging frequency ranged between 4.0-15.0 MHz, with a standard center frequency of 8.5 MHz. Two types of images were collected, Shear Wave Elastography (SWE) and standard B-mode. Images were collected with an elasticity range of 0-180 kPa to minimize gross imaging artifacts associated with the surrounding tissue and skull while blinding the user to intra-hemispheric features at low values of Young's Modulus, which generally lie between 2 and 25 kPa [11-12,16-18].

A micro-positioner was used to maintain the SWE transducer over the rodent's head perpendicular to show coronal slices. Multi-purpose ultrasound lotion (Polysonic, Cone

Instruments, Solon, OH, USA) was used to maintain ultrasound conduction between the transducer and the head.

The brain was first imaged using traditional B-mode; combined B-mode and SWE imaging began when the brain had been located and centered in the B-mode image (Fig. 1 A). Significant effort was made to minimize creation of imaging artifacts in the SWE images. These artifacts (e.g., Fig. 1 C,D) are areas of high Young's Modulus that do not correlate with the neuroanatomy [11-12,16-17]. For each rodent, we collected 10 – 30 images. We selected 3 images where both the impact site was identifiable in the B-mode imaging and had minimal elasticity artifacts.

After imaging the animals were sacrificed and perfused and the brains were harvested for histological analysis. The brains were sectioned through the injury site at 8-10 micron thick that were stained with hematoxylin and eosin (H&E) and, separately, cresyl violet (CV). The slides were digitized and the extent of TBI damage was quantified by manual selection of the injured area using ImageJ.

Post-processing of SWE Images

Image post-processing was completed using MATLAB (Natick, MA, USA). The entire brain region was manually selected in the SWE-mode image obtained from the Aixplorer (Fig. 1 B). The brain region in the SWE image was selected based on the structure of the skull as seen in the corresponding B-mode image.

After the selection of images, the elasticity map of the selected brain region was reduced to display an elasticity range of 0-35 kPa (Fig. 1 C,D), down from 0-180kPa (Fig. 1 A,B). Regions of interest from within each hemisphere of brain tissue within the skull were then manually selected directly from the elasticity map (Fig. 1 D). Regions of comparable size and location but free of imaging artifacts were selected from both hemispheres.

Regional selection and analysis was performed three times for each image and then averaged together to produce the intra-hemispheric average of brain-tissue stiffness for each of the two hemispheres of brain within the image.

Data Analysis

For each image for each rodent, a representative value of the Young's Modulus value of each hemisphere was used directly for analysis as well as normalized by dividing the average value of Young's Modulus for a given hemisphere by the average of the two

hemispheres. The normalized Young's Modulus therefore provides a measure of the elasticity of a given hemisphere relative to the average value across the entire brain.

Kruskal-Wallis One Way Analysis of Variance tests on Ranks (ANOVA) was applied to the data using SigmaPlot (Systat Software, San Jose CA).

Results

Quantification of areal extent of damage in H&E and Creysl Violet.

We quantified the anatomical extent of TBI damage as shown histologically (Fig. 1 E,F). There was no difference between groups with regard to the extent of damage shown by H&E versus cresyl-violet stains nor in the extent of damage between the acute and 24-hour groups for either species (Table 1).

Directly measured values of Young's Modulus for rats.

Figure 2 shows directly measured average values of Young's Modulus for each hemisphere of sham, acute, and 24-hour TBI rats. There was no significant difference between average Young's Modulus values within any of the sham or acute or 24-hour TBI groups (Fig. 2 A). We did, however, observe changes in average Young's Modulus between groups. Specifically, each of the contralateral and ipsilateral hemispheric values of the acute and 24-hour TBI groups have values of Young's Modulus that increased significantly relative to their respective values for the sham TBI group (Fig. 2 B).

Normalized values of Young's Modulus for rats.

Figure 3 shows normalized Young's Modulus values for each hemisphere of sham, acute, and 24-hour TBI rats. There was no significant difference between average Young's Modulus values within the sham or acute TBI groups while by 24 hours there existed a significant difference between ipsilateral and contralateral hemispheric averages of normalized Young's Modulus (Fig. 3 A). With regard to between-group changes, by 24 hours after TBI the ipsilateral values of normalized Young's Modulus decreased with time while the contralateral values increased with time (Fig. 3 B).

Directly measured values of Young's Modulus values for mice.

Figure 4 shows directly measured values of Young's Modulus for each hemisphere of sham, acute, and 24-hour TBI mice. There was no significant difference between average Young's Modulus values within the sham group while there exist significant differences between the average ipsilateral and contralateral values of Young's Modulus both acutely and at 24 hours after TBI (Fig. 4 A). Relative to the sham value of Young's Modulus the ipsilateral value decreased by 24 hours after TBI while the contralateral value increased acutely before returning to a value comparable to the sham value of Young's Modulus (Fig. 4 B).

Normalized values of Young's Modulus for mice.

Figure 5 shows normalized Young's Modulus values for each hemisphere of sham, acute, and 24-hour TBI mice. There was no significant difference between average Young's Modulus values within the sham group. In contrast, the average value of Young's Modulus for the ipsilateral hemisphere was significantly smaller than that of its contralateral value both acutely and at 24 hours after TBI (Fig. 5 A). In addition, by 24 hours after TBI the ipsilateral values of normalized Young's Modulus decreased with time while the contralateral values increased with time (Fig. 5 B).

Discussion

We created mild traumatic brain injury (TBI) in mice and rats using the controlled cortical impact (CCI) paradigm. We then used a commercial diagnostic ultrasound machine to measure intra-hemispheric averages of brain-tissue stiffness (the Young's modulus, a measure of shear resistance of tissue) of the brains both acutely and 24 hours after TBI induction. We presented analysis of both the absolute value and normalized values of brain stiffness, the latter documenting changes in brain-tissue stiffness relative to the average value of the entire brain at a given time point.

We note that tissue stiffness values inferred by ultrasound shear-wave elastography are sensitive to the tissue's net fluid content. For example, all else being equal more fluid as a percentage of tissue decreases the measured stiffness, while less fluid increases the measured stiffness [5]. One can appreciate this view by considering Derieppe et al. [10],

whose study of ischemia in kidney showed a decrease in SWE-derived stiffness, and Xu et al. [11], whose study of ischemia in mouse brain showed a decrease in stiffness ipsilateral to injury (a region of extensive edema) and an increase in stiffness contralateral to injury (a region of known reduced cerebral blood flow). Paraphrasing the literature analysis of Xu et al. [11], ischemic brain within a cranium doesn't sag while ischemic kidney within a belly does.

We start with our results for rats. The absolute value of Young's modulus increased through time in each of the ipsilateral and contralateral hemispheres compared to controls (Fig. 2). There exist many physiological processes that occur after TBI that can alter the fluid content of brain that may explain our observations, subject to direct testing. For example, our observed global increase in measured brain-tissue stiffness across hemispheres through time may have arisen due the combined effect of reduced peripheral blood pressure and increased in ICP, which can work together to reduce cerebral perfusion pressure (CPP) hence cerebral blood flow throughout the brain. This hypothesis is consistent with the observations of some researchers [19-20] though not all [21]. Also contributing to this net increase in brain-tissue stiffness may have been a reduction in cerebral spinal fluid (CSF) within the cranium [20]. We note that these hypotheses require that global peripheral (blood pressure) and intracranial (ICP; CPP; cerebral blood flow; CSF) processes more than compensate for the focal increase in fluid content within TBI brain ipsilateral to the injury caused by the observed edema and hemorrhage. That increase in focal fluid content may itself balance in part the focal ischemia observed by others after CCI [21]. Attention to the normalized data highlights these potentially competing, focal effects.

Specifically, we note that by 24 hours after TBI the normalized value of brain-tissue stiffness within the ipsilateral hemisphere reduced in magnitude relative to controls while its counterpart within the contralateral hemisphere increased in magnitude relative to controls (Fig. 3). Moreover, by 24 hours after TBI the ipsilateral value of normalized brain tissue stiffness was significantly reduced relative to the contralateral value. Because of our choice of normalization technique, these results document changes in brain-tissue stiffness that occur relative to the global rise in the absolute value of brain-tissue stiffness reported above.

With regard to the observed reduction in relative ipsilateral brain-tissue stiffness, we first note the presence and time course of edema and hemorrhage demonstrated by our histology (Fig. 1 E, F and Table 1) and consistent with other's observations[22-23]. In

addition to edema, others have documented ischemia measured using laser Doppler velocimetry and whole-brain autoradiography techniques. Specifically, Bryan et al. [21] observed immediate ipsilateral ischemia after severe CCI that lasted at least four hours after injury. We therefore hypothesize that the observed edema formation ipsilateral to injury by 24 hours lowered the normalized value of the measured intra-hemispheric average of brain elasticity compared to that of sham TBI in a manner that more than compensated for the likely effect of ischemia known to occur in at least severe CCI, but undocumented within our experiment, all riding on a wave of global reduction in blood flow due to elevated ICP. This complex hypothesis, besides requiring verification in future studies, is consistent with recent observations of reduced brain-tissue stiffness at the site of CCI in mice relative to the rest of the brain, based on images created with magnetic resonance elastography [24-25].

With regard to the observed increase in contralateral relative brain-tissue stiffness, our observations and those cited above show no edema formation contralateral to the injury while [19], for example, observed decreased cerebral perfusion pressure and reduced cortical perfusion contralateral to the injury, both consistent with our observations.

Our results for normalized values of brain-tissue stiffness observed for mice after TBI (Fig. 5) are consistent with what we observed for rats (Fig. 3). This suggests it possible that the same interplay of ipsilateral edema versus ischemia and global reduction in cerebral blood flow that can occur for rats may also have occurred for mice. Consistent with this idea, Lundblad et al. [26] observed after *severe* CCI significant edema in ipsilateral cortex, a reduction of cortical blood flow in ipsilateral cortex on time scales of hours to 24 hours and in contralateral cortex by 24 hours. Comparable studies are lacking for mild CCI and warrant future work.

Our measurement of the absolute value of intra-hemispheric brain-tissue stiffness of mouse brain differs significantly, however, from what we observed for rat brain. For example, ipsilateral to the injury site the absolute value of Young's modulus value decreased by 24 hours, rather than increased as for rats. Also, the absolute value of Young's modulus increased acutely contralateral to the injury as for rats, but returned to baseline values by 24 hours after TBI, unlike in rats, which continued to increase. This difference may have arisen due to the large discrepancy in areal extent between the ipsilateral craniectomy required for mice versus that for rats. Specifically, the craniectomy uncovered essentially the entire hemispheric cranial vault for mice while less than half of that vault for rats. Perhaps this relatively large craniectomy reduced the possibility of elevated ICP, hence

reduced CPP and cerebral blood flow in our mice. The mouse model may, therefore, only display the effects of intra-hemispheric dynamics (edema, local ischemia) and reduced global cerebral blood flow due to changes in systematic blood pressure rather than the additional effects of global intracranial dynamics (elevated ICP, hence a further decrease in CPP and therefore in cerebral blood flow).

Limitations

This study had several limitations due to its preliminary nature. First and foremost, we've generated a series of largely untested hypotheses regarding the possible impact on measured brain-tissue stiffness due to the relative weights of different fluid sources within brain tissue, motivated by our direct observations and the published literature. These hypotheses require direct testing. Also, out of necessity we performed a relatively large craniectomy to facilitate the CCI method for mice, which may have altered the effects of elevated ICP and reduced CPP known to occur in these animal models. Future studies should target use of larger animal models of TBI to mitigate this possible effect. In addition, we used SWE technology not optimized for rodent brain encased in a skull. The artifacts we observed associated with the skull produced elasticity values that are not consistent with other, published measurements of brain-tissue stiffness, forcing us to carefully select around these artifacts so that they did not confound our data.

Conclusion

We used ultrasound shear-wave elastography to measure absolute as well as normalized values of intra-hemispheric stiffness of rodent brain both acutely and at 24 hours after TBI via the controlled cortical impact (CCI) method. These observed changes in brain-tissue stiffness after TBI may reflect multiple physiological processes known to occur within brain after TBI caused by CCI. These processes include the initial formation of edema and hemorrhage known to develop ipsilateral to TBI and observed by us, as well as the known but un-assayed by us (a) formation of ischemia ipsilateral to TBI, (b) reduction in cerebral perfusion pressure and (c) blood flow observed both ipsilateral and contralateral to TBI. Ultrasound-based elastography may therefore offer a method to monitor subtle changes in brain after TBI.

Future work should target testing the links we have hypothesized between observed changes in brain-tissue stiffness and the underlying physiology of TBI. In addition,

366 future work should address currently identified problems in the translation of this
367 technology to human use, including delivery in a transcranial fashion of a shaped pulse of
368 ultrasound energy sufficient to generate usefully observable shear waves, and the known
369 large-scale anisotropy of human brain and its likely impact on the formulae used to
370 translate shear-wave propagation into estimates of brain-tissue stiffness.
371

372 **Acknowledgements**

373 We received support for this work from the Congressionally Directed Medical Research
374 Program (CDMRP), Award Number W81XWH-11-2-0109.
375
376
377
378

379 **Table 1**

Table 1: % extent of damage of TBI in histological analysis.				
Stain	Acute Mice	24 Hr Mice	Acute Rats	24 Hr Rats
H&E	8.02% +/- 2.2%	14.2% +/- 7.5%	4.62% +/- 2.7%	7.57% +/- 1.6%
CV	8.33% +/- 0.6%	11.2% +/- 2.7%	4.95% +/- 0.1%	6.98% +/- 2.1%

380

381

382

383

Figures

Fig. 1. Image Processing. (A) Aixplorer images in SWE mode (top) and B-mode (bottom) (B) The brain region was selected from the elastographic image (0-180 kPa) with reference to the B-mode image. (C) The SWE image of the brain was rescaled to 0-35 kPa to enhance the contrast. (D) Regions of Interest selected manually to avoid skull and artifacts (large values of Young's Modulus greater than that of brain). (E) Hematoxylin and Eosin and (F) Cresyl Violet staining of corresponding brain.

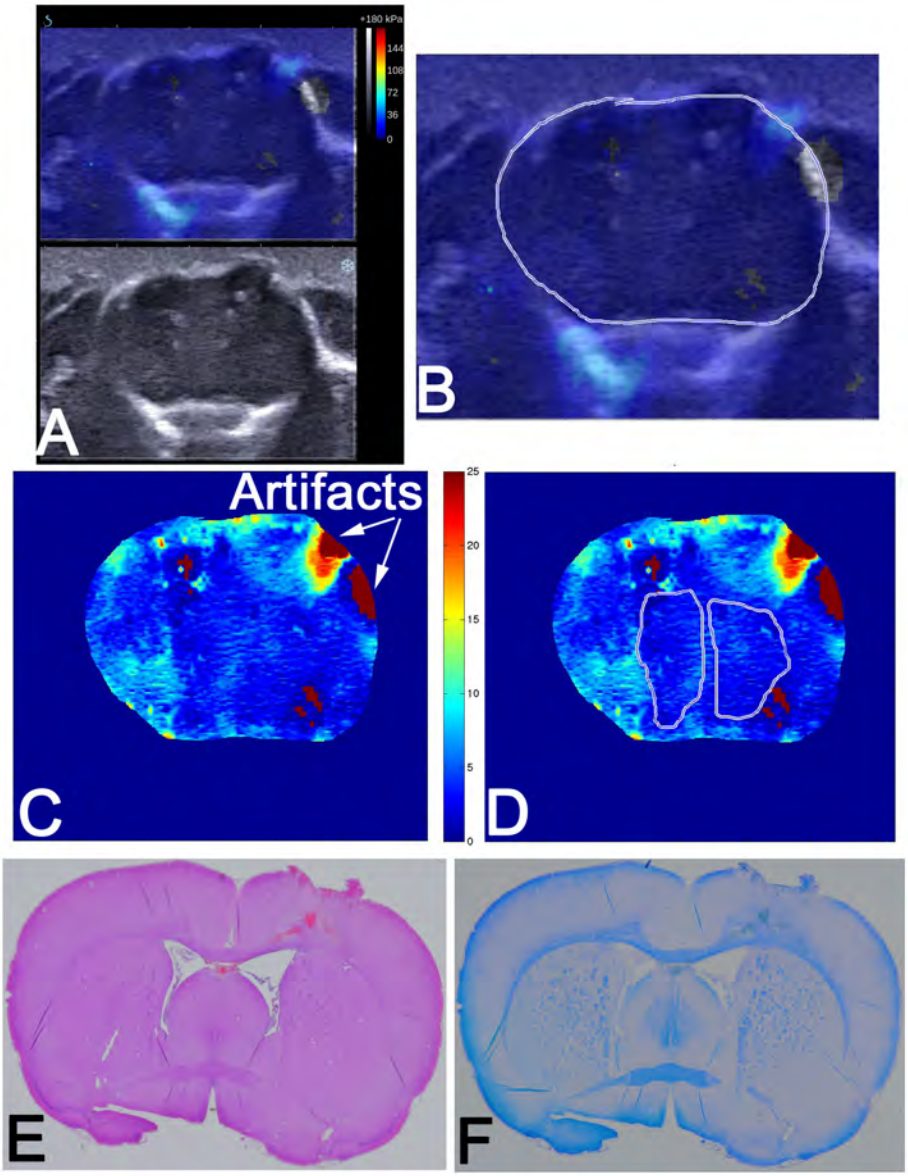

Fig. 2. Directly measured values of Young's Modulus for ipsilateral and contralateral hemispheres of the brains of rats for all test groups. * = $p < 0.05$ between the two indicated groups.

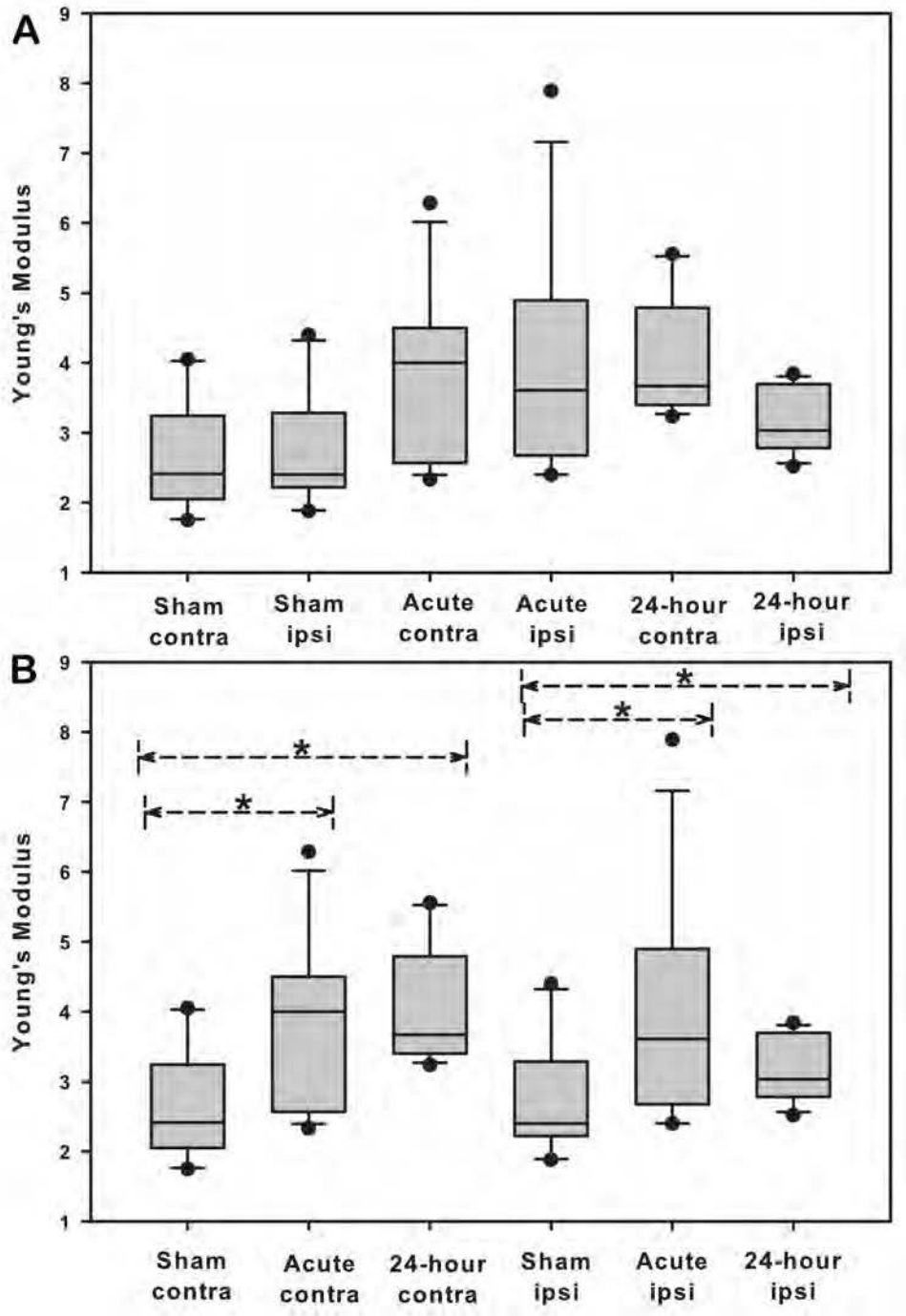

403 **Fig. 3**. Values of normalized Young's Modulus for ipsilateral and contralateral hemispheres
404 of the brains of rats for all test groups. * = $p < 0.05$ between the two indicated groups.

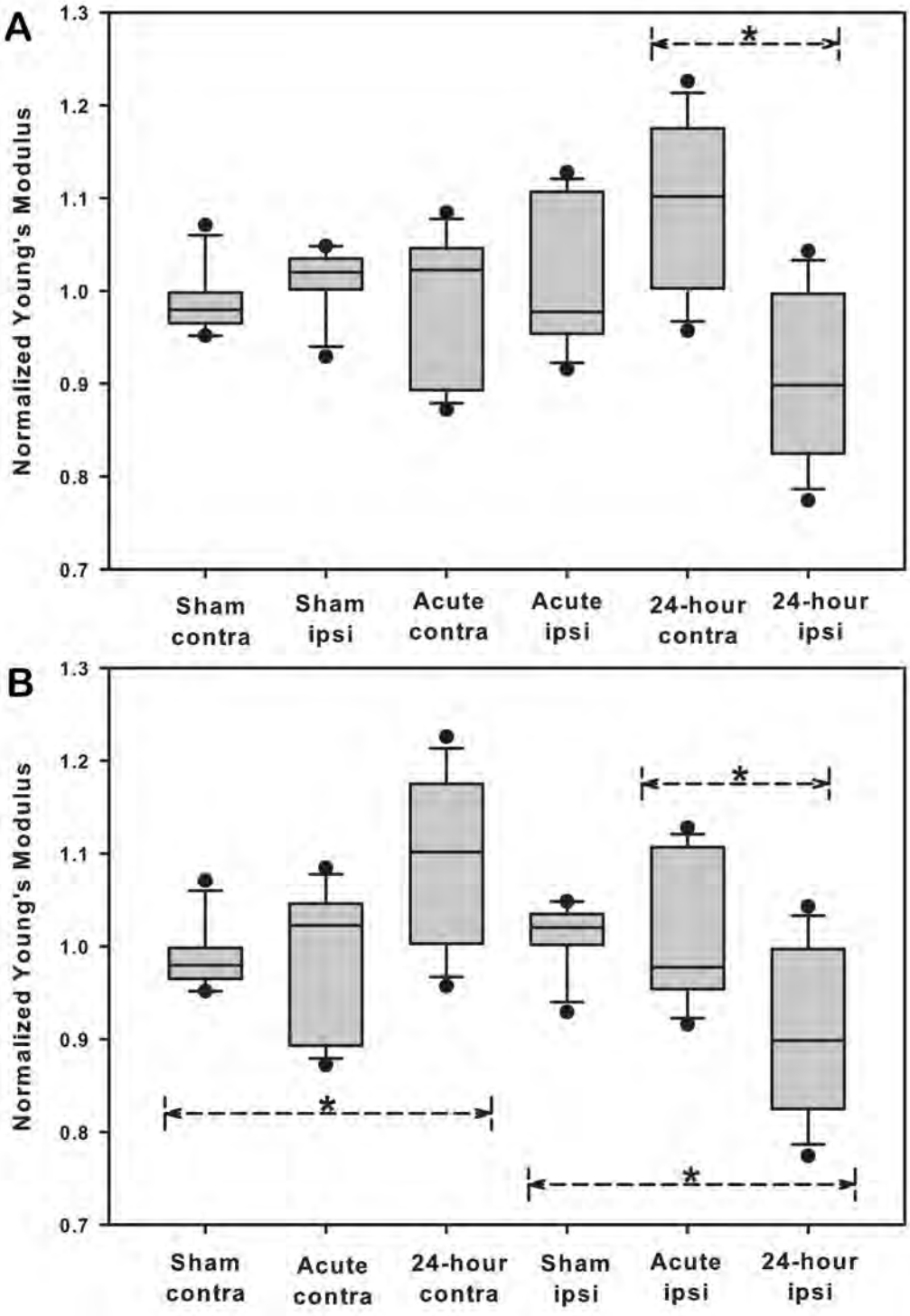

405
406

Fig. 4. Directly measured values of Young's Modulus for ipsilateral and contralateral hemispheres of the brains of mice for all test groups. * = $p < 0.05$ between the two indicated groups.

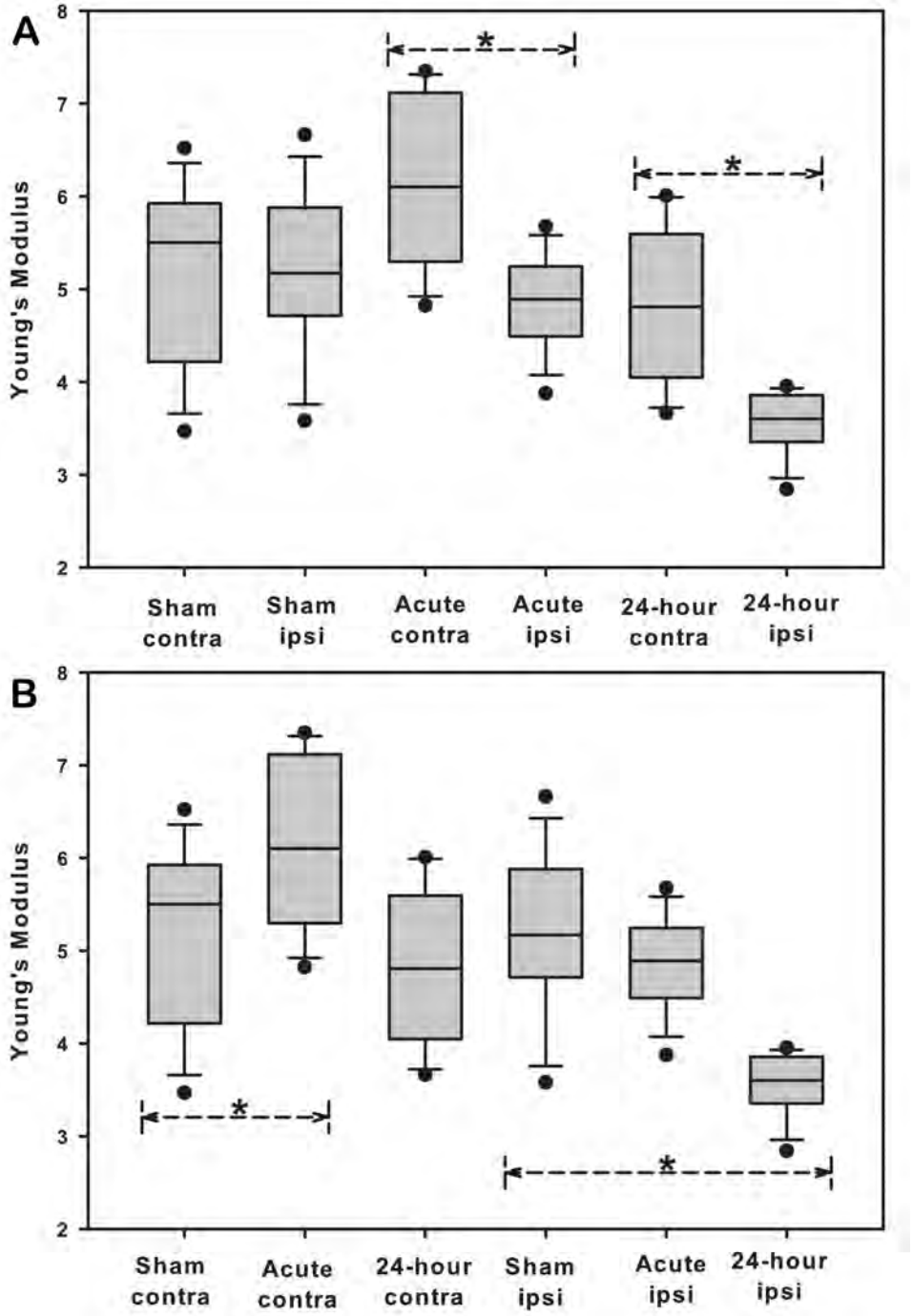

414 **Fig. 5**. Values of normalized Young's Modulus for ipsilateral and contralateral hemispheres
415 of the brains of mice for all test groups. * = $p < 0.05$ between the two indicated groups.
416

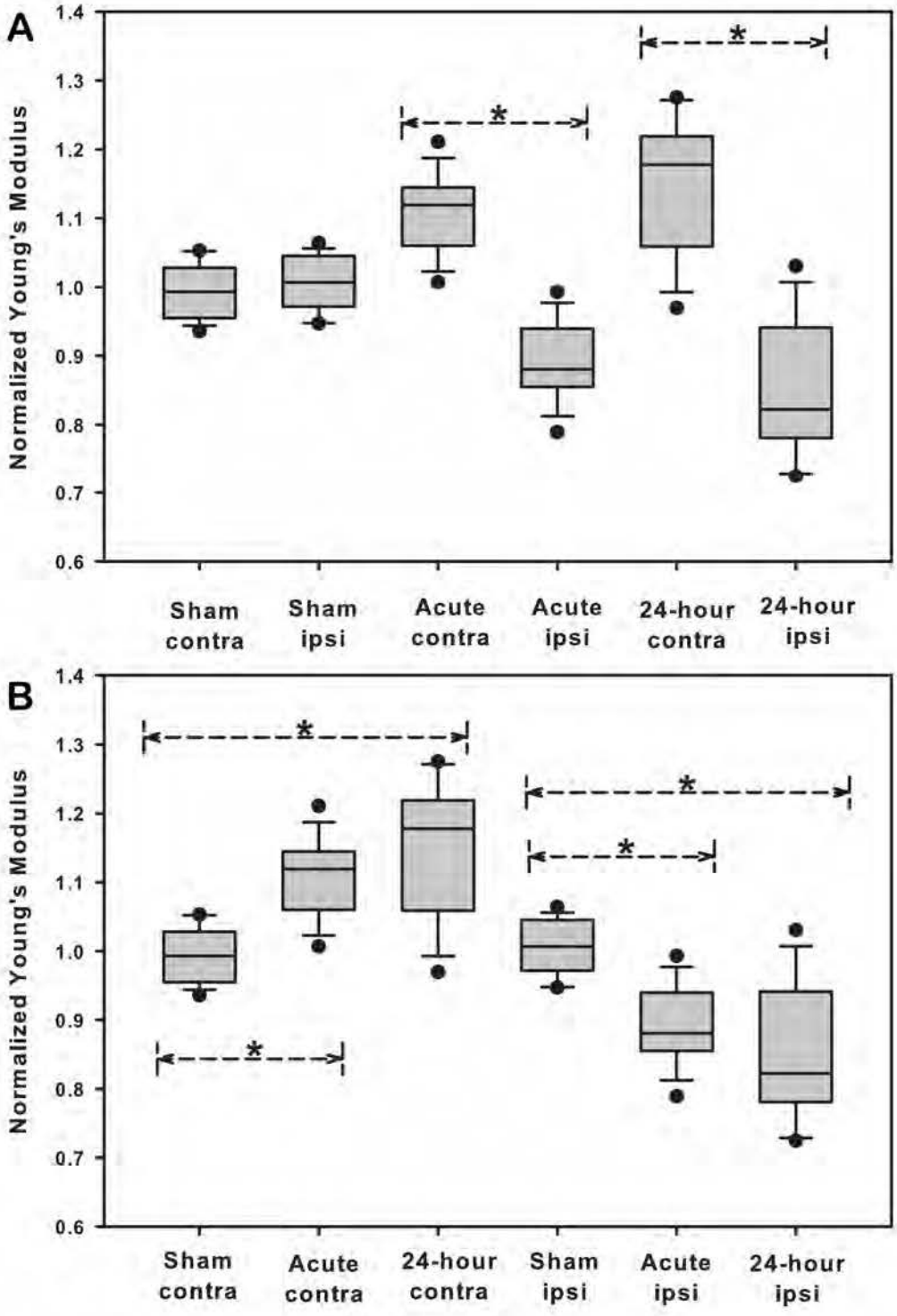

417

418 **References**

419

420 1. Meyer K, Helmick K, Doncevic S, and Park R. Severe and Penetrating Traumatic
421 Brain Injury in the Context of War. *J Trauma Nurs* 2008; 15:185-189.
422 2. Faul M, Xu L, Wald MM, Coronado VG. Traumatic brain injury in the United States:
423 emergency department visits, hospitalizations, and deaths. Atlanta (GA): Centers for
424 Disease Control and Prevention, National Center for Injury Prevention and Control;
425 2010.
426 3. Lee B and Newberg A. Neuroimaging in Traumatic Brain Imaging. *NeuroRx* 2005;
427 2:372-383.
428 4. Fryback DG, Thronbury JR. The Efficacy of Diagnoistic Imaging. *Med Decis Making*
429 1991; 2:88-94.
430 5. Tanter M, Bercoff J, Athanasiou A, Deffieux T, Gennisson JL, Montaldo G, Muller M,
431 Tardivon A, and Fink M. Quantitative assessment of breast lesion viscoelasticity:
432 initial clinical results using supersonic shear imaging. *Ultrasound Med Biol* 2008;
433 34:1373-86.
434 6. Deffieux T, Gennisson JL, Larrat B, Fink M, Tanter M. The variance of quantitative
435 estimates in shear wave imaging: theory and experiments. *IEEE Trans Ultrason*
436 *Ferroelectr Freq Control* 2012; 59(11):2390-410.
437 7. Gennisson JL, Deffieux T, Fink M, Tanter M. Ultrasound elastography: principles and
438 techniques. *Diagn Interv Imaging* 2013; 94(5):487-95.
439 8. Athanasiou A, Tardivon A, Tanter M, Sigal-Zafrani B, Bercoff J, Deffieux T, Gennisson
440 JL, Fink M, and Neuenschwander S. Breast lesions: quantitative elastography with
441 supersonic shear imaging--preliminary results. *Radiology* 2010; 256:297-303.
442 9. Garra BS. Elastography: current status, future prospects, and making it work for you.
443 *Ultrasound Q* 2011; 27:177-86.
444 10. Derieppe M, Delmas Y, Gennisson JL, Deminière C, Placier S, Tanter M, Combe C, and
445 Grenier N. Detection of intrarenal microstructural changes with supersonic shear
446 wave elastography in rats. *Eur Radiol* 2012; 22:243-50.
447 11. Xu ZS, Lee RJ, Chu SS, Yao A, Paun MK, Murphy SP, Mourad PD. Evidence of Changes
448 in Brain Tissue Stifness After Ischemic Stroke Derived From Ultrasound-Based
449 Elastography. *J Ultrasound Med* 2013; 32:485-494.
450 12. Macé E, Cohen I, Montaldo G, Miles R, Fink M, and Tanter M. In vivo mapping of brain
451 elasticity in small animals using shear wave imaging. *IEEE T Med Imaging* 2011;
452 30:550-8.
453 13. Misgeld T, Kerschensteiner M, Bareyre FM, Burgess RW, and Lichtman JW. Imaging
454 axonal transport of mitochondria *in vivo*. *Nat Methods* 2007; 4(7):559-561.
455 14. Lighthall JW. Controlled cortical impact: a new experimental brain injury model. *J*
456 *Neurotrauma* 1988; 5(1):1-15.
457 15. Dixon CE, Clifton GL, Lighthall JW, Yaghmai AA, Hayes RL. A controlled cortical
458 impact model of traumatic brain injury in the rat. *J Neurosci Meth* 1991; 39:253-262.
459 16. Green MA, Bilston LE, and Sinkus R. In vivo brain viscoelastic properties measured
460 by magnetic resonance elastography. *NMR Biomed* 2008; 21:755-64.
461 17. Kruse SA, Rose GH, Glaser KJ, Manduca A, Felmlee JP, Jack CR Jr., and Ehman RL.
462 Magnetic resonance elastography of the brain. *Neuroimage* 2008; 39:231-7.
463 18. McCracken PJ, Manduca A, Felmlee J, Ehman RL. Mechanical transient-based
464 magnetic resonance elastography. *Mag Reson Med* 2005; 53(3):628-39.

19. Cherian L, Robertson CS, Contant CF Jr., Bryan RM Jr. Lateral Cortical Impact Injury in Rats: Cerebrovascular Effects of Varying Depth of Cortical Deformation and Impact Velocity. *J Neurotrauma* 1994; 11(5):573-585.
20. Colgan NC, Cronin MM, Gobbo OL, O'Mara SM, O'Connor WT, Gilchrist MD. Quantiative MRI Analysis of Brain Volume Changes due to Controlled Cortical Impact. *J Neurotrauma* 2010; 27:1265-1274.
21. Bryan RM Jr., Cherian L, Robertson C. Regional Cerebral Blood Flow After Controlled Cortical Impact Injury in Rats. *Anesth Analg* 1995; 80:687-95.
22. Baskaya MK, Dogan A, Temiz C, and Dempsey RJ. Application of 2,3,5-triphenyltetrazolium chloride staining to evaluate injury volume after controlled cortical impact brain injury: role of brain edema in evolution of injury volume. *J Neurotrauma* 2000; 17:93-9.
23. Elliott MB, Jallo JJ, and Tuma RF. An investigation of cerebral edema and injury volume assessments for controlled cortical impact injury. *J Neurosci Meth* 2008; 168:320-4.
24. Boulet T, Kelso ML, Othamn SF. Microscopic magnetic resonance elastrography of traumatic brain injury model. *J Neurosci Meth* 2011; 201:296-306.
25. Boulet T, Kelso ML, Othman SF. Longterm *in vivo* imaging of viscoelastic properties of the mouse brain following controlled cortical impact. *J Neurotrauma* 2013; 30(17):1512-20.
26. Lundblad C, Grande PO, and Bentzer P. A mouse model for evaluation of capillary perfusion, microvascular permeability, cortical blood flow, and cortical edema in the traumatized brain. *J Neurotrauma* 2004; 21:741-53.

Ultrasonics xxx (2015) xxx–xxx

Contents lists available at ScienceDirect

Ultrasonics

journal homepage: www.elsevier.com/locate/ultras

Transcranial vibro-acoustography can detect traumatic brain injury, *in-vivo*: Preliminary studies

Martin W. Suarez [a,b], David D. Dever [a], Xiaohan Gu [a], P. Ray Illian [c], Abbi M. McClintic [b], Edin Mehic [a,b], Pierre D. Mourad [a,b,c,d,*]

[a] Department of Bioengineering, Univ. of WA, 1959 NE Pacific St., Box 356470, Seattle, WA 98195, United States
[b] Department of Neurological Surgery, Univ. of WA, 1959 NE Pacific St., Box 356470, Seattle, WA 98195, United States
[c] Applied Physics Laboratory, Univ. of WA, 1959 NE Pacific St., Box 356470, Seattle, WA 98195, United States
[d] Division of Engineering and Mathematics, Univ. of WA Bothell, 1959 NE Pacific St., Box 356470, Seattle, WA 98195, United States

ARTICLE INFO

Article history:
Received 17 October 2014
Received in revised form 21 April 2015
Accepted 25 April 2015
Available online xxxx

Keywords:
Traumatic brain injury
Vibro-acoustography
Acoustic emissions
Diagnostic focused ultrasound
Frequency compounding

ABSTRACT

Vibro-acoustography (VA) uses two or more beams of confocal ultrasound to generate local vibrations within their target tissue through induction of a time-dependent radiation force whose frequency equals that of the difference of the applied frequencies. While VA has proven effective for assaying the mechanical properties of clinically relevant tissue such as breast lesions and tissue calcifications, its application to brain remains unexplored. Here we investigate the ability of VA to detect acute and focal traumatic brain injury (TBI) *in-vivo* through the use of transcranially delivered high-frequency (2 MHz) diagnostic focused ultrasound to rat brain capable of generating measurable low-frequency (200–270 kHz) acoustic emissions from outside of the brain. We applied VA to acute sham-control and TBI model rats (sham $N = 6$; TBI $N = 6$) and observed that acoustic emissions, captured away from the site of TBI, had lower amplitudes for TBI as compared to sham-TBI animals. The sensitivity of VA to acute brain damage at frequencies currently transmittable across human skulls, as demonstrated in this preliminary study, supports the possibility that the VA methodology may one day serve as a technique for detecting TBI.

1. Introduction

Traumatic brain injury (TBI) represents a major problem for troops in modern combat zones. The military has reported 250,000 cases of TBI between 2002 and 2012 alone [1]. The actual number of TBI's may be even higher than reported; military field tests indicate that 40% of all TBI cases are missed due to high levels of diagnostic subjectivity and patient variability, including patient's reporting of their symptoms [2]. While standard clinical techniques for imaging TBI such as computer tomography (CT) and magnetic resonance imaging (MRI) can readily identify and quantify the presence, location and extent of a brain injury, the size of commercially available versions of devices thus far makes them largely inaccessible in the field. This results in a delay in quantification of the type and extent of TBI – epidural, subdural, versus intra-parenchymal bleeds; diffuse axonal injury, among others [3]. Delayed initial quantification of the brain injury leads, in turn, to a delay in triage decisions and implementation, resulting in a reduced likelihood for timely treatment and therefore a reduction in the quality of the clinical outcome for these patients [4]. As one example, surgical evacuation of epidural and subdural bleeds within hours of TBI immediately reduces the chance of exposure of brain to blood products while reducing intracranial pressure, hence brain herniation and associated ischemia, yielding significantly positive clinical outcomes. This is in contrast to the case of intra-parenchymal bleeds, where the initial exposure of blood products to brain tissue causes significant and irreversible brain-tissue damage that immediate evacuation of the hematoma does not alleviate [5]. Therefore development of portable systems for identifying the presence, type and severity of TBI in the field has the potential to significantly improve outcomes for injured soldiers and their civilian counterparts through support of early diagnosis and treatment decisions otherwise unavailable to the on-site medical practitioner without the information such systems can provide.

Given this clinical need, there exists active work supporting the creation of field-portable TBI imaging and/or detection devices, for example MRI for imaging and detection of structural changes in brain [6], electroencephalography or EEG for detection of altered

* Corresponding author at: Department of Neurological Surgery, University of Washington, Box 356470, Seattle WA 98195-6470, United States. Tel.: +1 206 543 3570, +1 206 543 9125 (office); fax: +1 206 543 6785.
E-mail address: pierre@apl.washington.edu (P.D. Mourad).

http://dx.doi.org/10.1016/j.ultras.2015.04.014
0041-624X/

brain function [7], and near-infrared spectroscopy (NIRS) for detection of altered brain structure [8].

The Infrascanner offers a particularly useful example of a field-deployable brain-injury detection device, here based on NIRS technology. The Infrascanner has the form factor of a hand-held device. It can detect asymmetries in relative cerebral oxygen saturation between four quadrants of the head in a manner capable of detecting the presence of supratentorial intracranial bleeds with volumes greater than 3.5 cubic centimeters. This system achieves approximately 90% sensitivity and specificity for these particular injuries, despite complications such as intrinsic variability in extra-cerebral tissues that TBI can exacerbate [9,10].

Here we seek to perform first studies that could lead to another type of hand-held, in-field TBI triage system, one based on a type of diagnostic ultrasound called vibro-acoustography (VA) that can directly interrogate brain tissue, likely without interference from intervening tissues when its focus is placed intracranially.

One may describe vibro-acoustography as an ultrasound-based means of generating focal vibrations within an object in order to characterize the structure and/or material properties of the object based on its acoustic response to the applied vibration. The ultrasound vibration generated within tissue arises due to a 'dynamic radiation force' intrinsic to appropriately designed ultrasound. Specifically, the dynamic radiation force is generated when two ultrasound beams of slightly different frequency (f_1 and f_2) intersect at a shared focal region within the tissue of interest. This force causes the tissue within the focus to oscillate at the difference frequency ($\Delta f = f_1 - f_2 \ll f_1, f_2$) of the two incident ultrasound beams. Vibrating tissue from within the ultrasound focus can generate detectable acoustic emissions. The amplitude of these emissions has been used to quantify the viscoelastic properties of various tissue types and objects [11,12].

While the focused nature of VA predisposes it to spot sampling, typical use of VA to date has been for imaging small areas, made possible by incrementally scanning across regions of interest [12–14]. VA imaging has been used to distinguish between normal and calcified femoral arteries *in-vivo* [13], to detect calcifications within the prostate [12], detect breast lesions in humans [14], image lesions in the liver [12], and track brachytherapy seeds used in the treatment of prostate cancer [12]. An advantage to Vibro-acoustic images is that they do not exhibit the speckle noise traditionally associated with B-mode images (although VA is not completely free of spatially variant artifacts).

Vibro-acoustography has not yet been applied to brain tissue. Brain trauma can alter the mechanical properties of the brain [15–17], leading us to hypothesize that the acoustic emissions from brain generated by VA would differ between damaged versus undamaged brain tissue. Here, we present preliminary data consistent with this hypothesis.

2. Materials and methods

2.1. Traumatic brain injury induction

All animal procedures were approved by the Institutional Animal Care and Use Committee (IACUC) of the University of Washington, Seattle, WA. Male Sprague Dawley® rats (Charles River, Wilmington, MA), weighing between 351 ± 80 g, were split into two experimental groups: a sham control group ($N = 6$) and an acute TBI group ($N = 6$). Selection of animal model and sample size were informed by our previous studies [18] where significant differences in brain tissue stiffness, as captured by ultrasound shear wave elastography, were identified between groups containing five animals. Additionally, these studies indicated that the relatively large size of the cranial window (needed for our TBI model, as described later) in mice, as compared to rats, may have altered the effects of elevated intracranial pressure (ICP) and cerebral perfusion pressure (CPP) following injury. Rats were selected as an animal model for this study in an effort to minimize the influence of the cranial window on ICP and CPP.

Animals were anesthetized throughout the study with Isoflurane gas through a facemask with spontaneous ventilation (5% for induction and 1.5–2% for maintenance, with a 100% oxygen flow rate of 1.5 L/min). Depth of anesthesia was monitored via toe pinches and tracking of blink reflex. The rats were then placed on a stereotactic surgical platform (Stoelting, Wood Dale, IL) with metal bars that were fixed within the rats' ears to stabilize their heads for surgery, injury induction, and ultrasound data collection. A heating pad was placed under the rat to maintain body temperature. The head was then shaved and the remaining hair removed with Nair® (Church & Dwight Co, INC., Princeton, NJ, USA). Following epilation, subcutaneous lidocaine (0.08 mL, 20 mg/mL) and bupivicaine (0.08 mL, 0.32 mg/mL) were administered and spread across the surgical site by manual palpation.

An incision along the sagittal plane was then made from behind the ears to between the eyes. Following this, an area of skull approximately 1 cm in width was fully exposed. A small bone drill was used to create a circular hole through the skull, at a location 3 mm anterior and 2 mm to the left of the lambda, without penetration of the dura. A rongeur was used to widen this cranial window radially to a diameter of approximately 3 mm, in order to accommodate the tip of a controlled cortical impact (CCI) device (AMS 201, AmScien Instruments, Richmond, VA, USA).

For each animal in the sham or acute TBI group the tip of the CCI device was positioned directly over the cranial window and lowered to the surface of the brain. At this point, sham animals were removed from the apparatus while remaining under anesthesia and prepared for ultrasonic imaging, described below. For TBI animals, the device was then fired to induce a 2 mm deep impact into the brain with a tip speed of 1.15 m/s, consistent with the protocol of Lighthall [19] as refined by Dixon et al. [20]. Within 10 min after TBI or completion of the sham surgery, ultrasound application to the brain was initiated.

2.2. Ultrasound system

A dual-element 2 MHz focused ultrasound transducer (Sonic Concepts, Model H-148, Woodinville, WA) was used to produce the dynamic radiation force needed to generate tissue vibrations (Fig. 1). This transducer has a radius of curvature of 63.2 mm, placing the center of the focus 51.74 mm from the exit plane. The inner element has an inner diameter of 22.6 mm and outer diameter of 48.29 mm. The outer element has an inner diameter of 49.05 mm and outer diameter of 64.0 mm. Linear simulations of both elements operating in unison (Fig. 2) predict a focus that measures 8 mm axially and 1 mm radially as measured at the pressure half-maximum value.

Each transducer element was driven independently by a function generator (33220A 20 MHz Function/Arbitrary Waveform Generator, Agilent, Santa Clara, CA) through independent amplifiers (Model A150 RF Power Amplifiers, E&I, Rochester, NY); a third gating function generator (of the same model) was used to control synchronous output of the transducer elements. The VA transducer was calibrated at the carrier frequencies (not the difference frequencies). The signals from each element, captured at the transducer's focus, were independently measured in degassed water with a needle hydrophone (HNR-100 S/N 1370, ONDA, Sunnyvale, CA), to ensure that both elements contributed equal pressure to the mutual focus for each of the difference frequencies considered: 200–270 kHz, inclusive, in steps of 10 kHz. The calibrated hydrophone used for configuration had a range of

Please cite this article in press as: M.W. Suarez et al., Transcranial vibro-acoustography can detect traumatic brain injury, *in-vivo*: Preliminary studies, Ultrasonics (2015), http://dx.doi.org/10.1016/j.ultras.2015.04.014

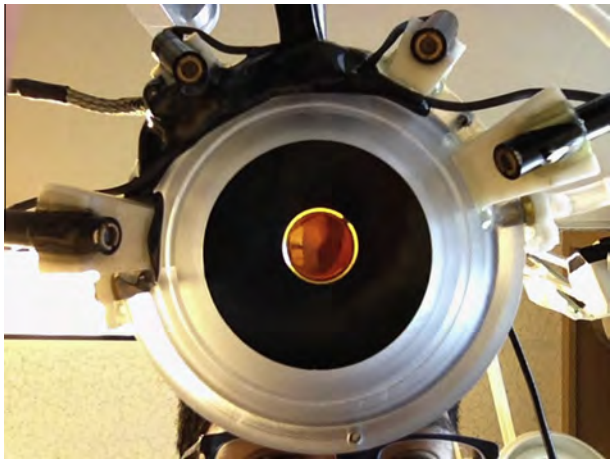

Fig. 1. H-148 HIFU transducer (black), confocal PVDF hydrophone (orange), and plastic coupling cone with aiming lasers. The lasers were affixed such that they intersected at the transducers focus and were used to position the ultrasound focus. To couple the transducer to the rat's skull, the cone is filled with degassed water and sealed with latex. The volume of water in the cone can be adjusted with a pair of syringes connected to the cone's sides (not seen here). (For interpretation of the references to color in this figure legend, the reader is referred to the web version of this article.)

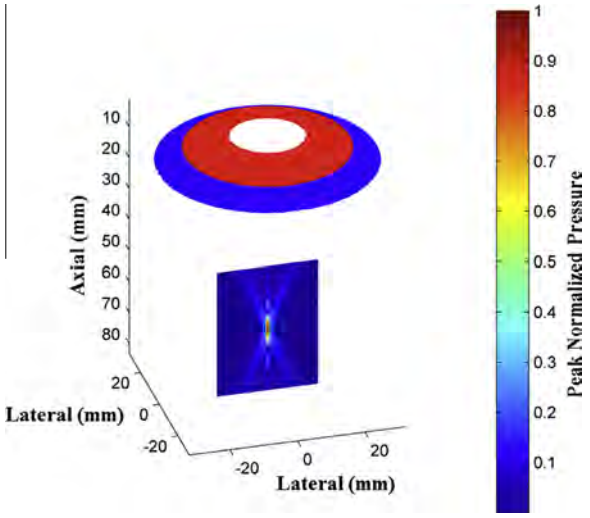

Fig. 2. Mathematical simulation of the maximum pressure field generated by the H-148 transducer. The transducer face is depicted on top. In the pressure field, red indicates high pressure and blue low pressure. (For interpretation of the references to color in this figure legend, the reader is referred to the web version of this article.)

0.25–20 MHz. The net pressure generated by both transducer elements at a given difference frequency was used to determine that the generated spatial-peak-temporal-average (SPTA) intensity (I_SPTA) was 0.27 W/cm^2 ± 0.04 W/cm^2. The above procedure for measuring I_SPTA was then repeated with the ultrasound transmitted through rat skull to determine the ultrasound intensity experienced by rat brain; this was measured to be 0.015 W/cm^2 ± 0.0062 W/cm^2. The ultrasound intensities measured through skull fall below the FDA prescribed limit for human cephalic imaging (0.094 W/cm^2 I_SPTA) [21]. Ultrasound was applied for 1000 μs and the acoustic emissions from the tissue were recorded for 1200 μs and sampled at 50 MHz.

2.3. Application of diagnostic focused ultrasound

Rats were maintained under Isoflurane anesthesia throughout Vibro studies. The face of the ultrasound transducer was covered with a plastic coupling cone filled with degassed water for optimal ultrasound transmission to the brain. The front of this coupling cone was sealed with a sheet of acoustically translucent latex, the rear was closed with a focused polyvinylidene fluoride (PVDF) hydrophone (Harisonic® Y-107-7, Olympus Corporation, Tokyo, Japan). The focus of the hydrophone was selected such that it remained confocal with the transducer. The entire research-grade VA device (transducer, coupling cone, and PVDF hydrophone together) has a diameter of 10 cm and a height of 8 cm and weighs 540 g. The hydrophone was then connected to an amplifier (Hydrophone Booster Amplifier, Precision Acoustics Ltd., Dorchester, Dorset, UK) and oscilloscope (LeCroy, Chestnut Ridge, NY, USA) to enhance the acoustic emissions from the brain. These acquired waveforms were then transmitted via GPIB connection to an analogue-to-digital converter (Alazar Technologies Inc., Pointe-Claire, QC Canada) for MATLAB-based data processing (MathWorks, Natick, MA, USA).

The transducer and hydrophone were mounted on a three-way micro-positioning system (Velmex, INC., East Bloomfield, NY, USA) to allow the ultrasound focus to be moved to any anatomical point of interest. A laser guidance system was implemented (Fig. 1) in order to identify the spatial location of the ultrasound focus during experiments. Specifically, these lasers were affixed to the coupling cone such that their intersection marked the center of the transducer's focus. The transducer's position was adjusted via the micro-positioner such that the center of the ultrasound focus projected 5 or 8 mm below the surface of the skull, as desired. The focus could then be moved to each of the two depths and two target locations, Front Left (FL5 or FL8) and Front Right (FR5 or FR8). The target locations were defined relative to the site of injury by their coronal position on the skull (Fig. 3). Target locations were chosen such that measurements were not taken from regions of the head where skull was removed. Acoustic emissions from the brain across the range of predetermined difference frequencies (200–270 kHz, in steps of 10 kHz) were collected twice for each difference frequency. Collected waveforms were exported to MATLAB® for analysis. Within MATLAB the two waveforms from

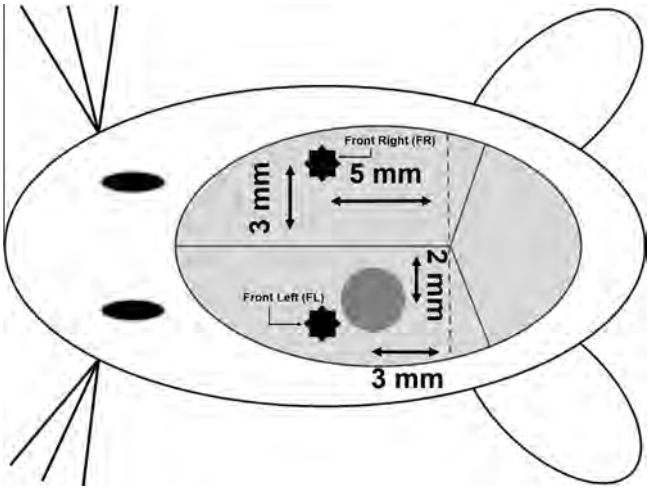

Fig. 3. Surgical procedure schematic. A hole was drilled in the skull 3 mm in diameter (gray circle), located 3 mm anterior and 2 mm to the left of the lambda, which is the visible rear suture joint on the surface of the skull. Focused ultrasound was applied at the locations denoted by the stars, which are both 5 mm anterior of the lambda and 3 mm left and right, respectively. The focus was aimed 5 and 8 mm deep at each location.

Please cite this article in press as: M.W. Suarez et al., Transcranial vibro-acoustography can detect traumatic brain injury, *in-vivo*: Preliminary studies, Ultrasonics (2015), http://dx.doi.org/10.1016/j.ultras.2015.04.014

each difference frequency were then averaged to produce a final, mean value of the amplitude for the acoustic emission. This mean value for the acoustic emission amplitude was collected three times for all difference frequencies and from each target location.

2.4. Histopathology

After completion of the ultrasound studies, rats were euthanized via pentobarbital (Schering-Plough Animal Health, Canada) overdose. The abdominal cavity was opened, the heart exposed, and a butterfly needle inserted into the left ventricle. Saline and then neutral buffered formalin were pumped through the animal to fix the tissue. The fixed brain was harvested and placed in formalin solution for at least 7 days. Fixed brains were sliced and stained by the University of Washington Histology and Imaging Core. Standard Hematoxylin & Eosin (H&E) stain was applied to the slides.

Completed slides were scanned and analyzed using Image J (NIH) to quantify the relative area of injured brain tissue compared to the whole brain.

2.5. Analysis of acoustic emission data

Through initial exploration we found that the spectral magnitude of the carrier frequencies varied daily, likely as a result of small fluctuations in amplifier gain and inter-rat differences such as skull thickness. To account for fluctuations that might influence our results we normalized acoustic emissions by the spectral magnitudes of their associated carrier frequencies, as captured by the PVDF hydrophone in our VA system. We developed the following equation to account for this effect:

$$N = \frac{A^2}{C_1^2 + C_2^2}$$

'A' is the maximum spectral magnitude from within the frequency bin of an acoustic emission generated by a given applied difference frequency. C_1 and C_2 are the spectral magnitudes of each of the backscattered carrier frequencies associated with this difference frequency. N compensates for fluctuations in the spectral amplitudes of the carrier frequencies described above. N yields non-dimensional measures of the Vibro-acoustic emission signal magnitude for a given frequency. We normalized the raw acoustic emissions data for all the analysis presented in this paper.

We analyzed the measured acoustic emissions from rat brain across a frequency range of 200 kHz–2.5 MHz to include signals from each of the carrier frequencies as well as from the difference frequency. Following acquisition, acoustic emissions were decomposed via Fast Fourier Transform (FFT) to examine their frequency components. Emissions were then gathered into frequency bins centered at each difference frequency with a width of 7 kHz. Once binned, we applied incoherent frequency compounding, following the mathematical technique described by others [22,23], to the acoustic emission data, by averaging across the acoustic emission magnitudes generated at each applied difference frequency.

2.6. Statistical analysis

The magnitudes of Vibro-acoustic emissions acquired from sham and TBI rats were not normally distributed, as a result a non-parametric test (Mann–Whitney Rank Sum Test; SigmaPlot, Systat Software Inc, San Jose, CA, USA) was used for statistical comparisons. Each animal contributed 24 data points for a total of 144 data points in each experimental group (sham or TBI) at each location. In all comparisons, the significance level was set at $p \leqslant 0.05$.

3. Results

3.1. Vibro-acoustic emissions

Vibro-acoustic emission data was successfully collected from a total of 12 rats: 6 sham and 6 TBI. The non-compounded acoustic emission amplitudes from sham rats at all positions and depths were generally higher than those for TBI rats across all applied difference frequencies. However, the only statistically significant difference arising from acoustic emissions at a single difference frequency was captured at the FL5 location with an applied difference frequency of 260 kHz ($p = 0.04$).

After frequency compounding, where acoustic emission signals at their respective locations were averaged across all difference frequencies, the amplitudes for sham rats at all positions and depths remained generally higher than those for TBI animals. Significant differences between sham and TBI brain in the compounded emission amplitudes were seen at the FL5 location ($p = 0.001$), the FL8 location ($p = 0.001$), and the FR5 location ($p = 0.015$) (Fig. 4).

3.2. Histopathology

Histopathological analysis showed that the controlled cortical impact device created a focal contusion injury at and around the site of impact. The injury occupied on average 10.96 ± 2.43% of the brain, covering approximately 3 mm × 4 mm. The outer edges of the histologically identifiable damage reached within 0.7 mm of the front-left Vibro application location and 3.9 mm from the front-right location.

4. Discussion

Here we present the first Vibro-acoustography (VA) study applied to brain. As this was a preliminary study we wanted optimal conditions for ultrasound application and acquisition to ensure we were obtaining the highest quality data possible. Animals were epilated prior to the application of ultrasound to ensure optimal coupling of the transducer with the animal's head. Animal fur is quite thick and has the potential to trap air bubbles which may act as scatterers/reflectors even when coupling gels are thoroughly applied. VA applied in humans would be done through acoustic

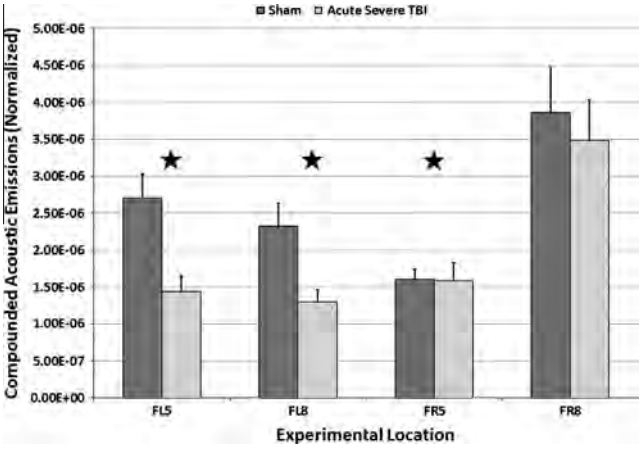

Fig. 4. Normalized and compounded Vibro-acoustic emissions from all experimental locations. Error bars represent standard error. Stars denote statistically significant differences ($P \leqslant 0.05$). Each experimental group (sham or TBI) had 144 data points at each location. At FL5 Mann–Whitney U Statistic = 7816; $P = 0.001$, at FL8 Mann–Whitney U Statistic = 7572; $P = 0.001$, at FR5 Mann–Whitney U Statistic = 8141; $P = 0.015$, at FR8 Mann–Whitney U Statistic = 8921 $P = 0.199$.

Please cite this article in press as: M.W. Suarez et al., Transcranial vibro-acoustography can detect traumatic brain injury, *in-vivo*: Preliminary studies, Ultrasonics (2015), http://dx.doi.org/10.1016/j.ultras.2015.04.014

windows such as the temporal, foramen magnum, transorbital, submandibular, etc. In this manner we estimate that ~80% of the brain can be accessed; as an example Kucewicz et al. [24] demonstrated that ultrasound applied through the right temporal window can capture skull on the left side of the head as well as structures 10 cm left or right of the axial direction. More brain can be made accessible to VA by steering the ultrasound focus (adjusting the angle at which the transducer makes contact with the acoustic windows). While the presence of hair over some of the acoustic windows remains a concern, standard practice for transcranial Doppler ultrasound in humans (as practiced by experienced sonographers) demonstrates that gel can be applied to the hair in these regions while minimizing air bubbles to allow routine collection of ultrasound data.

We delivered VA to brain tissue with and without an acute focal contusion injury, and were able to detect significant differences in the compounded acoustic emissions captured from these two groups. Specifically, following the TBI, we observed a measurable and statistically significant difference between ultrasound-induced, compounded acoustic emissions from sham TBI rat brain versus actual TBI rat brain. We detected these differences for tissue within four millimeters of damaged brain, at three of four anatomical sites.

We note that our compounded data analysis highlighted statistically significant changes in acoustic emissions from TBI brain versus sham TBI brain. However, when we analyzed acoustic emissions from the independent applied difference frequencies (used to construct compounded data), we rarely saw statistically significant effects. The efficacy of a compounded analysis of acoustic emissions relative to an analysis of emissions from individual difference-frequencies likely arises from the effect of reverberation on each analysis technique, as well as the strong frequency dependence of reverberation [22,23]. Reverberations are produced when acoustic emissions generated within the brain reflect from different locations and interact constructively or destructively within the cranium prior to their exit from the cranium and their recording by our PVDF hydrophone. The effect of reverberation on acoustic emissions used to create VA images manifests as spatial variability in the image. Additionally, the effect of reverberation on acoustic emissions varies significantly with the applied difference frequency. For our experiments, reverberation at a single difference frequency would alter the amplitude of acoustic emissions from brain alone as compared to acoustic emissions from a brain enclosed by skull. Significant modification of an acoustic emission due to reverberation could then result in the mischaracterization of the mechanical properties of an object. With regard to TBI this could entail identifying healthy tissue as damaged or vice versa. Thus by applying a range of difference frequencies to induce acoustic emissions from brain, then averaging the emissions across all applied frequencies, a process known as incoherent frequency compounding, we seek to average away the influence of reverberation on our acoustic emission data from the brain within the cranium, thereby highlighting the acoustic emissions from the brain itself [22].

5. Limitations

The spatial resolution of our current VA device is limited by the physical size of the emitted focus (8 mm axial length and 1 mm radial length). Our current work shows that VA can detect injury when applied to brain 1–5 mm away from the actual location of induced injury (2–3 mm in diameter). While this gives a first estimate as to the size of injury our device can detect, we note that our induced injuries lie within a relatively small brain where their presence may affect the global properties of the brain, such as intracranial pressure. Future work using larger animals will enable us to further characterize the size of detectable injuries.

There exist obvious differences between our rat TBI model and genuine human TBI that require further study before application of VA to humans. Most obviously, the size and structure of a rat head differs significantly from that of a human cranium. The small size of a rat brain relative to that of a human brain likely facilitates differences in the extent of reverberation in acoustic emissions, owing to the proximity of the ultrasound focus to the skull. The human skull, while much larger, also represents an additional challenge due to its thickness, which attenuates the ultrasound transmitted into the brain. Access to sufficient brain with VA could be addressed by applying ultrasound through a variety of acoustic windows (temporal, foramen magnum, transorbital, submandibular, etc.) where the skull is relatively thin. As an example Kucewicz et al. [24] demonstrate that ultrasound applied through the right temporal window can capture skull on the left side as well as structures 10 cm anterior or posterior of the probe position in the axial direction. Insonation through acoustic windows with a carrier frequency of 2 MHz is a common practice in standard transcranial Doppler (TCD) currently used in humans [25]. Enabling a user determined focal depth for VA, modifying ultrasound parameters, and determining an ideal range of difference frequencies would also help optimize VA for human use.

Our study demonstrates that an analysis of Vibro-acoustic emissions is sensitive to the presence of brain damage up to at least 4 mm away, the largest distance available to us in this animal model. If this result represents what we can achieve with TBI detection via Vibro-acoustography in humans, then an efficient search for damaged human brain would require a high density of VA focal volumes, a likely impractical requirement. Therefore, practical implementation of VA may require its pairing to a secondary TBI imaging modality, such as standard diagnostic ultrasound imaging or shear-wave elasticity imaging [18,26], one with less spatial resolution and reduced specificity but with a broader field of view. We realize that combining VA with another imaging modality (diagnostic ultrasound) does represent an additional engineering challenge relative to VA alone, however, devices combining diagnostic ultrasound imaging with separate ultrasound modalities involving acoustic radiation force do exist, and have been used on humans Harper et al. [27]. Work with these kinds of devices do show increased complexity related to device use but also indicate that the increased engineering complexity produces increased efficacy. In the case of pushing kidney stones Harper et al. they use diagnostic imaging to guide ultrasound-based pushing. In our case we can guide VA ultrasound to possible TBI sites and reduce the time of diagnosis and increase the sensitivity and specificity of the diagnosis.

6. Conclusion

We envision eventual implementation of VA from a portable ultrasound device such as that made by Mobisante, whose small form factor (a cell phone or tablet with an attached, hand-sized ultrasound scan head) gives it important advantages in emergency situations and for the military. Many current VA applications utilize 2D image generation, which involves lengthy raster scans and compiling emissions from many different locations. However, our approach seeks to use point measurements of VA-induced acoustic emissions to verify the presence of TBI rather than image TBI. Therefore, coupling VA with a separate ultrasound imaging modality with some sensitivity to TBI might increase the speed of use as well as the net sensitivity and specificity of TBI diagnosis, subject of future work. The equipment used in this experiment (transducer, function generators, power supplies, etc)

Please cite this article in press as: M.W. Suarez et al., Transcranial vibro-acoustography can detect traumatic brain injury, *in-vivo*: Preliminary studies, Ultrasonics (2015), http://dx.doi.org/10.1016/j.ultras.2015.04.014

can be miniaturized, making it highly portable. For example, there exist standard ultrasound imaging systems that are laptop size (e.g. SonoSite EDGE sytem ~$35,000) and tablet or cell phone size (e.g. the MobiSante MobiUS ~$7500 or Philips VISIQ systems ~$14,500). A miniaturized VA platform similar to the EDGE, MobiUS or VISIQ systems would enable users to collect point VA measurements and examine the mechanical nature of tissues in question. Translation of VA to one of these devices would require design and fabrication of a new transducer, one that contains the appropriate ultrasound elements and hydrophone.

Successful miniaturization would produce a small, portable VA system optimized for use by first responders, combat medics, and other medical personnel. Use of such a device has the potential to significantly alter medical outcomes after acute TBI by enabling physicians to identify the type and extent of brain injury in the acute stage thereby facilitating steps to minimize the long-term medical consequences of that injury. Future studies will assess the efficacy of VA for TBI detection in more realistic animal models and work toward miniaturization of the VA system.

Acknoweldgements

This work was funded by U.S. Army Medical Research and Materiel Command, Award # W81XWH-11-2-0109, titled "Toward Development of a Field-Deployable Imaging Device for TBI".

References

[1] Hannah Fischer, U.S. military casualty statistics: operation new dawn, operation iraqi freedom, and operation enduring freedom, www.fas.org. Federation of American Scientists, n.d. Web. 9 May 2013.
[2] T.C. Miller, D. Zwerdling, Military still failing to diagnose, treat brain injuries, National Public Radio, 8 June 2010. <http://www.npr.org/2010/06/08/127402993/military-still-failing-to-diagnose-treat-brain-injuries>.
[3] S.S. Armin, A.R. Colohan, J.H. Zhang, Traumatic subarachnoid hemorrhage: our current understanding and its evolution over the past half century, Neurol. Res. 28 (2006) 445–452.
[4] B. Lee, A. Newberg, Neuroimaging in traumatic brain imaging, NeuroRx 2 (2005) 372–383.
[5] J.M. Seelig, D.P. Becker, J.D. Miller, R.P. Greenberg, J.D. Ward, S.C. Choi, Traumatic acute subdural hematoma: major mortality reduction in comatose patients treated within four hours, New Engl. J. Med. 304 (1981) 1511–1518, http://dx.doi.org/10.1056/NEJM198106183042503.
[6] C.Z. Cooley, J.P. Stockmann, B.D. Armstrong, M. Sarracanie, M.H. Lev, M.S. Rosen, L.L. Wald, Two-dimensional imaging in a lightweight portable MRI scanner without gradient coils, Magn. Reson. Med. 73 (2) (2015) 872–883, http://dx.doi.org/10.1002/mrm.25147. Epub 2014 Mar 25.
[7] L.S. Prichep, S. Ghosh Dastidar, A. Jacquin, W. Koppes, J. Miller, T. Radman, B. O'Neil, R. Naunheim, J.S. Huff, Classification algorithms for the identification of structural injury in TBI using brain electrical activity, Comput. Biol. Med. 53 (2014) 125–133, http://dx.doi.org/10.1016/j.compbiomed.2014.07.011. October; Epub 2014 Aug 1, PMID: 25137412.
[8] C.S. Robertson, E.L. Zager, R.K. Narayan, N. Handly, A. Sharma, D.F. Hanley, H. Garza, E. Maloney-Wilensky, J.M. Plaum, C.H. Koenig, A. Johnson, T. Morgan, Clinical evaluation of a portable near-infrared device for detection of traumatic intracranial hematomas, J. Neurotrauma 27 (2010) 1597–1604.
[9] A.E.R. Young, T.J. Germon, N.J. Barnett, A.R. Manara, R.J. Nelson, Behaviour of near-infrared light in the adult human head: implications for clinical near-infrared spectroscopy, Br. J. Anaesth. 84 (1) (2000) 38–42.
[10] J.M. Murkin, M. Arango, Near-infrared spectroscopy as an index of brain and tissue oxygenation, Br. J. Anaesth. 103 (Suppl. I) (2009) i3–i13.
[11] M. Fatemi, J.F. Greenleaf, Vibro-acoustography: an imaging modality based on ultrasound-stimulated acoustic emission, Proc. Natl. Acad. Sci. USA. (1999).
[12] M.W. Urban, A. Alizad, W. Aquino, J.F. Greenleaf, M. Fatemi, A review of Vibro-acoustography and its applications in medicine, Curr. Med. Imag. Rev. (2011) (November 1).
[13] C. Pislaru, B. Kantor, R.R. Kinnick, J.L. Anderson, M.C. Aubry, M.W. Urban, M. Fatemi, J.F. Greenleaf, In vivo vibroacoustography of large peripheral arteries, Invest. Radiol. (2008).
[14] A. Alizad, D.H. Whaley, M.W. Urban, R.E. Carter, R.R. Kinnick, J.F. Greenleaf, M. Fatemi, Breast vibro-acoustography: initial results show promise, Breast Cancer Res.: BCR 14 (5) (2012) R128, http://dx.doi.org/10.1186/bcr3323.
[15] B.D. Greenwald, D.M. Burnett, M.A. Miller, Congenital and acquired brain injury. 1. Brain injury: epidemiology and pathophysiology, Arch. Phys. Med. Rehab. (2003).
[16] T. Boulet, M.L. Kelso, S.F. Othamn, Microscopic magnetic resonance elastrography of traumatic brain injury model, J. Neurosci. Meth. 201 (2011) 296–306.
[17] T. Boulet, M.L. Kelso, S.F. Othman, Longterm in vivo imaging of viscoelastic properties of the mouse brain following controlled cortical impact, J. Neurotrauma (2013), http://dx.doi.org/10.1089/neu.2012.2788.
[18] Z.S. Xu, A. Yao, S.S. Chu, M.K. Paun, A.M. McClintic, S.P. Murphy, P.D. Mourad, Detection of mild traumatic brain injury in rodent models using shear wave elastography: preliminary studies, J. Ultras. Med. 33 (10) (2014) 1763–1771.
[19] J.W. Lighthall, Controlled cortical impact: a new experimental brain injury model, J. Neurotrauma 5 (1) (1988) 1–15.
[20] C.E. Dixon, G.L. Clifton, J.W. Lighthall, A.A. Yaghmai, R.L. Hayes, A controlled cortical impact model of traumatic brain injury in the rat, J. Neurosci. Methods (1991).
[21] Guidance for Industry and FDA Staff – Information for Manufacturers Seeking Marketing Clearance of Diagnostic Ultrasound Systems and Transducers, US Food and Drug Administration. 9 Sept 2008. http://www.fda.gov/RegulatoryInformation/Guidances/ucm070856.htm.
[22] M. Urban, A. Alizad, M. Fatemi, Vibro-acoustography and multifrequency image compounding, Ultrasonics (2011) 689–696.
[23] M. Urban, G. Silva, M. Fatemi, J. Greenleaf, Multifrequency vibro-acoustography, IEEE Trans. Med. Imag. 25 (10) (2006) 1284–1295.
[24] J.C. Kucewicz, B. Dunmire, N.D. Giardino, D.F. Leotta, M. Paun, S.R. Dager, K.W. Beach, Tissue pulsatility imaging of cerebral vasoreactivity during hyperventilation, Ultrasound Med. Biol. 34 (8) (2008) 1200–1208.
[25] M. Kassab, A. Majid, M. Farooq, H. Azhary, L. Hershey, E. Bednarczyk, M. Johnson, Transcranial doppler: an introduction for primary care physicians, J. Am. Board Fam. Med. 20 (1) (2006) 65–71.
[26] Z.S. Xu, R.J. Lee, S.S. Chu, A. Yao, M.K. Paun, S.P. Murphy, P.D. Mourad, Evidence of changes in brain tissues stiffness after ischemic stroke derived from ultrasound-based elastography, J. Ultrasound Med. 32 (3) (2013) 485–494.
[27] J.D. Harper, B. Dunmire, Y. Wang, J.C. Simon, D. Liggit, M. Paun, B.W. Cunitz, F. Starr, M.R. Bailey, K.L. Penniston, F.C. Lee, R.S. Hsi, M.D. Sorensen, Preclinical safety and effectiveness studies of ultrasonic propulsion of kidney stones, Urology 84 (2014) 484–489.